Microfluidic Separation: Validation of Shear Driven Circular Liquid Chromatography

Zur Erlangung des akademischen Grades eines

Dr. rer. nat.

von der Fakultät Bio- und Chemieingenieurwesen

der Technischen Universität Dortmund

genehmigte Dissertation

vorgelegt von

M.Sci. Ying Cai

aus

Hubei, China

bearbeitet am

ISAS – Institute for Analytical Sciences

Tag der mündlichen Prüfung: 06.04.2009

1. Gutachter: Prof. Dr. A. Schmid
2. Gutachter: Prof. Dr. A. Manz

Dortmund 2009

Abstract

A novel channel-free microfluidic chromatography system with a rotating plate was developed and successfully used for the shear driven circulation and separation of analytes. The method “channel-free shear driven circular liquid chromatography” combines the benefits of both shear driven chromatography and the cyclical separation approach.

Two shear driven rotating microfluidic setups were designed and optimized to investigate the rotating microfluidic flow behavior. One setup was explored to validate shear driven circular liquid chromatography without the need for channels. This cyclical approach potentially offers an infinite path length and does not involve the complications of micro- or nanofabrication. Variable theoretical plate numbers can be achieved by merely changing the number of cycles in the separation process. To demonstrate the technique two model fluorescent analytes rhodamine B and fluorescein were separated, and during the separation process the theoretical plate number exceeded 1000. Fast Fourier transform was utilized to convert the periodic fluorescent signals into frequency information for individual analytes especially in rotating system. This system and methodology can be further optimized, with higher plate number separations readily anticipated.

Another setup was fabricated to integrate automated hydrodynamic injection system without channels by taking advantage of molecular diffusion equilibrium in a microfluidic flow.

The channel-free microfluidic cyclical separation system has clear superiority over current liquid chromatography techniques and has potential applications in high efficiency liquid chromatography for life science.

Zusammenfassung

Ein neuartiges mikrofluidisches kanalfreies Chromatographie-System mit einer rotierenden Platte wurde entwickelt und erfolgreich eingesetzt für die Scherkraft-getriebene Bewegung und Trennung von Analyten. Die Methode der kanalfreien und kreisförmigen Scherkraft-getriebene Flüssigkeits-Chromatographie verbindet die Vorteile der Shear-driven-Chromatographie und der zyklischen Trennung.

Zwei Scherkraft-getriebene rotierende mikrofluidische Plattformen wurden entwickelt. Dabei lag der Fokus auf der Optimierung des rotierenden mikrofluidischen Fließverhaltens. Ein entwickeltes Setup diente zur Analyse von der kreisförmigen Sherkraft-getriebene Flüssigkeits-Chromatographie, wobei auf die Notwendigkeit von Kanälen verzichtet wurde. Dieser zyklische Ansatz bietet das Potenzial unendliche Weglängen anzuwenden. Weitere Vorteile liegen in der günstigen Herstellung des Chips und dem Wegfall von Komplikationen bei der Mikro- oder Nanofabrikation. Veränderliche theoretische Trennstufenzahl können erreicht werden, indem die Anzahl der Zyklen während der Trennung erhöht wird. Zur Demonstration der Technik wurden zwei fluoreszierende Modellanalyten getrennt mit einer Trennstufenzahl größer 1000. FFT wurde verwendet, um die Informationen der regelmäßigen fluoreszierenden Signale des rotierenden Systems in Form von Frequenz für die einzelnen Analysen zu nutzen. Die Einfachheit des Systems und der Methode können weiter mit Verbesserung der Trennstufenzahl optimiert werden.

Ein weiteres Setup wurde hergestellt, um eine automatisierte hydrodynamische Injektionsmethode ohne Kanäle anzuwenden. Dies bringt die Vorteile des molekularen Diffusions-Gleichgewichts bei einer mikrofluidischen Strömung.

Das kanalfreie mikrofluidischen zyklische Trennsystem ist den derzeit Flüssigkeits-Chromatographie-Techniken klar überlegen. Die viel versprechende Anwendung hat einen hohen Wirkungsgrad und verbessert die Effizienz der Flüssigkeits-Chromatographie im Bereich der Life Science.

Declaration

I hereby declare that my thesis **Microfluidic Separation: Validation of Shear Driven Circular Liquid Chromatography** was written independently with no sources or aids other than those documented.

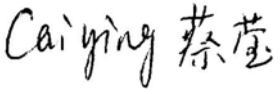

Dortmund, 19th September 2009

Copyright © September 2009 by Ying Cai

"The copyright of this thesis rests with the author. No quotations from it should be published without the author's prior written consent and information derived from it should be acknowledged".

Acknowledgement

Three years is a long time and also a short time. It is long, because I have made so many new friends and then saw them off during the past three years. But for scientific research, it is too short, as if I just start voyaging into the scientific ocean with my small sailing boat. Even though the journey is short, it is easier when you travel together. Eventually, I have the opportunity to express my gratitude for all the people who have accompanied me and supported me.

At first, I would like to give my greatest gratitude and respect to Prof. Dr. Andreas Manz and Prof. Dr. Andreas Schmid.

Prof. Dr. Andreas Manz gave me the chance to work in this institute. He affected me all the time with his passion and keen sensation on science. Every time when I felt so depressed like reaching a dead end, my talking with him would recharge me with full of energy. His way of encouraging his students was not only in research, but also in social life. That is why I respect him more than just a supervisor.

During my last few months with Prof. Dr. Andreas Schmid, I was deeply impressed by his precise and high-standard way of doing research. I respect him a lot for his providing only high quality work. He could not even realize how much I have learned from him.

Then, I want to give my sincere appreciation to Dr. Dirk Janasek, PD Dr. Joachim Franzke and Dr. Jonathan James West. Dr. Dirk Janasek helped me a lot with the designing and building the setup. His important comments help me a lot in staying at the right track. I thank PD Dr. Joachim Franzke for his valuable advices and tips. As a great group leader, he made me feel like working in a big family in the miniaturization group. I thank Dr. Jonathan James West for his fruitful discussions on broad topics concerning science.

The following appreciations I would like to give to the ISAS (Institute for

Analytical Sciences) workshop and material group. The workshop staff offered great effort when I built up the setup. I thank the material group people for helping me with measurements. White light interferometry was helped by Norman Ahlmann, IR by Dr. Heise and fluorescence spectroscopy by Ruediger Kuckuk. ISAS Berlin is greatly thanked for infrared ellipsometry measurement by Dr. Karsten Hinrichs.

Coming to our lab, I want to say thanks to Dr. Peter Jacob and Dr. Micheal Schilling for sharing the same lab. Discussing with them was a pleasure because they always had an objective point of view depending on their wide knowledge. I also thank Ann-Kathrin and Sasidhar for their kindly discussions and help. I thank Kaoru, Helke, and Cornelia to share the same office with me and made our office the source of happiness. Thank Elena, Marco, Sven, Jean-Philippe, Lindsey, Melissa, Katherine and Hendrik for their warm friendship. Thank you all!

I would like to give my special gratitude to Haixing for his nonstop and full-hearted moral support during my PhD work. He shared all of my happiness and sorrow for the past three years. His encouragements helped me overcome the difficulties in my life one after another.

At last, I would give my most thankfulness to my dear parents Lizhu Cai and Guiying Wu. Without their support, I can’t come to today. All my achievements also belong to them.

Ying Cai

Caiying 蔡莹

19.09.2008

TABLE OF CONTENTS

Chapter One: Introduction 1

Chapter Two: Micro Total Analysis Systems and Shear Driven Circular Chromatography 5

2.1 Micro Total Analysis Systems 5

2.1.1 Materials and Fabrication 8

2.1.2 Microfluidic Properties 9

2.2 Potential Driving Forces in Shear Driven Circular Chromatography 12

2.2.1 Centrifugal Force 13

2.2.2 Shear Force 15

2.3 Cyclic Liquid Chromatography 16

2.3.1 Miniaturized Liquid Chromatography 16

2.3.2 Cyclic Separation Method 19

2.4 Shear Driven Circular Chromatography 20

2.5 Summary 23

Chapter Three: a Shear Driven Rotating Microfluidic System 25

3.1 Establishment of Setups 25

3.1.1 Choice of Materials.....25

3.1.2 General Experimental Setup.....26

3.1.3 Liquid Film Thickness Measurement.....30

3.2 Applications of the Rotating Microfluidic System.....34

3.2.1 Fluorescent Particles.....34

3.2.2 Frequency Analysis.....37

3.2.3 Fluorophore Solution.....41

3.3 Summary.....42

Chapter Four: Channel-free Shear Driven Circular Liquid Chromatography.....45

4.1 A Channel-free System.....45

4.1.1 Introduction to Stationary Phase.....45

4.1.2 Coating Process.....46

4.1.3 Characterization of Glass Surface Properties.....50

4.1.4 Magnetic Powders.....54

4.2 Validation of Channel-free Shear Driven Circular Chromatography.....58

4.2.1 Separation of Rhodamine B and Fluorescein Mixture.....59

4.2.2 Resonance Energy Transfer.....67

4.2.3 Chromatographic Analysis.....71

4.2.4 Frequency Analysis.....74

4.2.5 Diffusion Coefficient.....80

4.2.6 Other Applications.....83

4.3 Summary 84

Chapter Five: Integration of an Automated Injection System with Separation Platform 87

5.1 Introduction of Injection with Micro-channel 87

5.1.1 Fabrication of Micro-channel 88

5.1.2 Injection Control 91

5.2 Channel-free Injection 96

5.3 Summary 100

Chapter Six: Summary and Outlook 103

6.1 Summary 103

6.2 Outlook 105

Appendix A: Additional Information on Micro-fluidic Rotating System 109

A.1 WLI Measurement 109

A.2 Structure Drawings of Two Designs 109

A.3 Oil-water System 112

Appendix B: Additional Information on Shear Driven Circular Liquid Chromatography 113

B.1 Contact Angle Measurements 113

B.2 Program in PICO 115

B.3 Chromatographic Performance 116

B.4 Program in MATLAB 117

B.5 Diffusion Coefficient 119

Appendix C: Additional Information on Injection Device 121

C.1 CCD Images of Injection and Rotation Process 121

Table of Abbreviations 123

Bibliography 125

CHAPTER ONE: INTRODUCTION

Analytical technique plays an important role in the development of science world. Given a cursory glance at the Nobel prizes in the last centuries, more than 50 topics are closely related to the analytical techniques, such as mass spectrometry, electron microscopy, chromatography, electrophoresis, nuclear magnetic resonance spectroscopy and so on.

Miniaturization is a technique to scale down the devices for user feasibility without losing the functionality. The applications of miniaturization can be traced back to decades ago, in electronics such as semiconductor devices and integrated circuit chips. The smaller mobile phones with more functions integrated and digital cameras with higher number of pixels are developed all owe to this technique. Besides daily life usage, miniaturized devices are also successfully used in molecular level analysis in life sciences and pharmacology. For example, DNA analysis using Polymerase Chain Reaction (PCR) chips are shown in figure 1.1 (A).

Nowadays, miniaturization is becoming a trend in analytical science. Thorough understanding of microfluidic fundamentals is developed and theories are established in order to build up application models directly or indirectly. And the intrinsic properties of fluid are utilized in miniaturization owe to these studies. As a landmark, the new concept Miniaturized Total Analysis Systems (μ-TAS) was introduced in 1990[1], and many applications are developed based on this concept. For example, the miniaturized Liquid Chromatography (LC) devices named “chip-based LC” and “bioanalyzers” developed by Agilent Technologies[1] are shown in figure 1.1 (B) and

[1] http://www.chem.agilent.com/scripts/PHome.asp

(D). Microfluidic chips with dynamic mixing and other functions shown in figure 1.1 (C) are developed by Micronit Microfluidic BV[2].

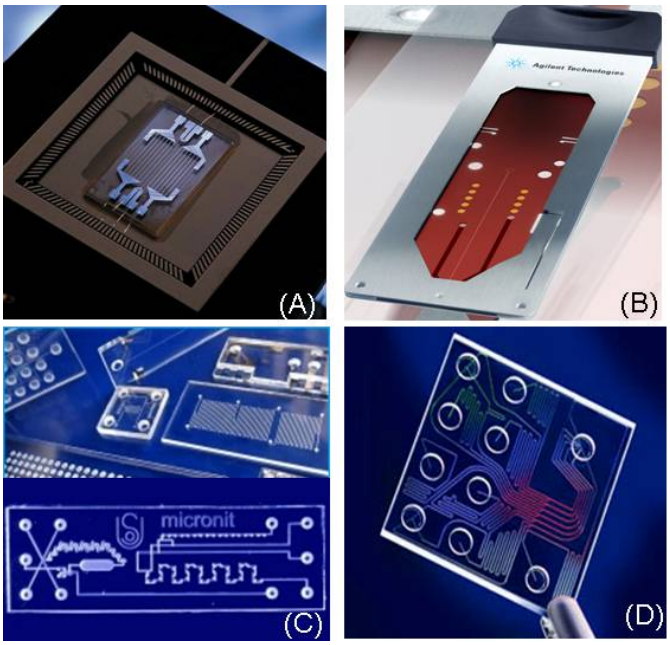

Figure 1.1: Miniaturized devices undertake various applications in analytical sciences, for example, (A) microfluidic PCR, (B) chip-based LC, (C) micromixer, and (D) bioanalyzers.

Separation method is predominant in analytical sciences. High Performance Liquid Chromatography (HPLC) and Capillary Electrophoresis (CE) are today's most widely used separation methods. In the commercial HPLC, the theoretical plate number is restricted to about 10^5 due to the critical pressure and the particle size. Those factors also determine the diffusional effects and heat transport in the packed column. Miniaturized open tubular liquid chromatography with proper detection methods can achieve higher theoretical plate numbers up to around $10^{6[2]}$. In electric driven systems such as capillary electrochromatography, the theoretical plate number is limited by the Joule heating effect and the electrophoretic mobility. These parameters are dependent on the electric voltage applied.

[2] http://www.micronit.com/en/home.php

In order to overcome pressure limitation in liquid chromatography and voltage limitation in electrochromatography, two possibilities are considered. One method is based on shear driven flow by taking advantage of the intrinsic fluid viscosity. In a channel with the same width, the mean velocity of the mobile phase is higher in a shear driven flow in comparison with a pressure driven flow. While the pressure driven flow profile is parabolic, and the shear driven flow is linear. The shear driven linear chromatography has been studied since 1999[3]. The other proposed method is the cyclic analytical method, which was firstly supposed by Martin in 1957[4] for Gas Chromatography (GC). In his description, two short columns were connected one after another to form a cyclic column instead of using one single long column. Later on, an improved method with no discontinuity along the column increased the separation efficiency by recycling the analytes coming out of a separation column. This method was reported with the name circular chromatography[5]. With this method, high theoretical plate numbers can be achieved and the analysis time is supposed to be reduced.

Shear Driven Circular Chromatography (SDCC) is a combination of both shear driven chromatography and circular chromatography. It is introduced to the microfluidic field as a method to realize liquid chromatography in a circular approach. The ultimate purpose is to integrate SDCC as a separation platform into μ-TAS and eventually increase the overall separation efficiency. SDCC is aimed at overcoming the limitation of separation column length in traditional analysis conceptions and is expected to achieve higher theoretical plate numbers.

The validation of SDCC was accomplished in this study. A new rotating microfluidic system was built up and the analytes were successfully separated. Instead of using a silica gel packed column or a fabricated micro-channel, the separation procedure was realized with a novel channel-free system based on flat glass plates.

Thesis Outline

This thesis is divided into four chapters according to their contents.

Chapter two briefly introduces the theoretical background of SDCC. This chapter is comprised of basic concepts and current development of μ-TAS, SDCC fluid dynamics, and the heuristic process of miniaturized chromatography techniques.

Chapter three describes the setups of a shear driven rotating microfluidic platform, which can be used for chromatographic applications; and the optimization of the microfluidic platforms is also discussed.

Chapter four focuses on the chromatographic experiments and data analysis based on the system built up in chapter three. The validation of channel-free SDCC is accomplished and two fluorescent components are successfully separated.

Chapter five gives a brief introduction of the automated injection methods which can be integrated with the rotating microfluidic platform to quantify the chromatographic methods described in chapter four.

CHAPTER TWO: MICRO TOTAL ANALYSIS SYSTEMS AND SHEAR DRIVEN CIRCULAR CHROMATOGRAPHY

2.1 Micro Total Analysis Systems

Since the last decades, a new concept which was concerned with the miniaturization of chemical or biological analysis systems has emerged in the analytical science. This concept is also known as μ-TAS or lab on a chip which is based on the Micro-Electro-Mechanical System (MEMS).

μ-TAS is used to describe the miniaturized analytical processes, which integrate different analytical units including sample injection, separation module and detector parts. For some miniaturized biochemical usages or drug discoveries, the system consists of even more individual steps such as sampling, sample pre-concentration, filtering, mixing, isolation and analysis. All these steps can be realized in a microfluidic chip or in a biochip, which is a platform for non-fluidic arrays.

Figure 2.1 shows how the macroscopic reaction system can be sorted and transferred into smaller units. This is the precondition for the following processes such as serial processing and analysis. After miniaturized, the reaction space and sample quantities can be greatly reduced.

μ-TAS has many advantages compared with macroscopic analysis systems

owing to the scaling down of size. Such advantages include:

- sizes of the analysis devices are reduced and less space is needed,
- the analysis devices are more integrated and easier to handle,
- the consumption of samples and reagents are reduced, and
- the analytical efficiency is increased.

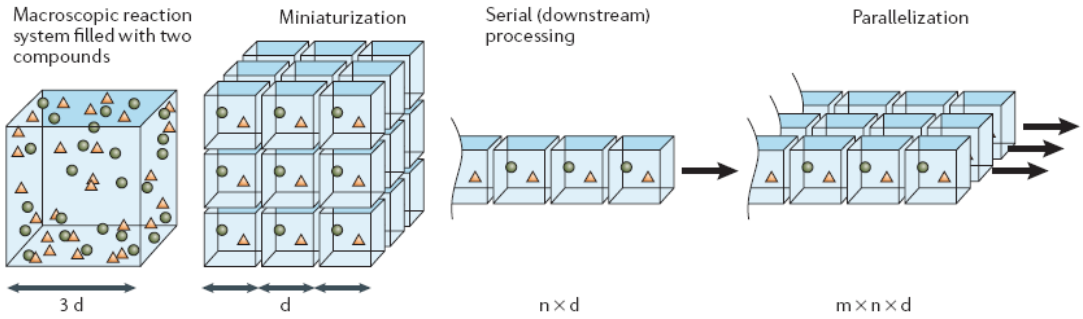

Figure 2.1: Illustration of scaling laws showing the size of both macroscopic and miniaturized reaction systems, the serial processing and analysis can be realized after miniaturization in μ-TAS[6].

In the 1990's, μ-TAS has been firstly applied in separation techniques such as miniaturized liquid chromatography and capillary electrophoresis[7] to increase their separation efficiency. The efficiency increases for LC is because that the miniaturized chromatography columns have minimized the heat and mass transfer in the macroscopic analysis system. The miniaturized CE with micro-channels has better resolution with extremely short channel length and relatively low voltage. These two well developed separation techniques have opened up the application markets according to the specialties of μ-TAS. Some examples of the applications are shown in figure 2.2. For example, in the clinical diagnostic analysis, a temperature-controllable electrophoresis chip was developed to separate lactate dehydrogenised isoform[8]; in the protein analysis, seven fluorescent marked

proteins were successfully separated in 2.5 s in a free-flow isoelectric focusing microfluidic device, which produced a linear pH gradient from pH 2.5 to pH 11.5 (figure 2.2 (A)). Some combined separation methods are much more efficient than single-function methods. For example, a technique named gradient elution moving boundary electrophoresis combined the electrophoretic immigration of the chemical components with the hydrodynamic bulk counter flow of the solution in the micro-channels (figure 2.2 (B)). Temperature gradient focusing was integrated with field amplified continuous injection to achieve an enrichment more than 1000 fold for the analyte separations[9].

μ-TAS touched on a large variety of applications in chemical and biological industry as well. The commercial HPLC-Chip was developed by Agilent Labs[10] from the prototype shown in figure 2.2 (C). It has a nano-electrospray interface connected to a mass spectrometer and an analytical LC column with the appropriate column length according to the flow rate of the nano-electrospray.

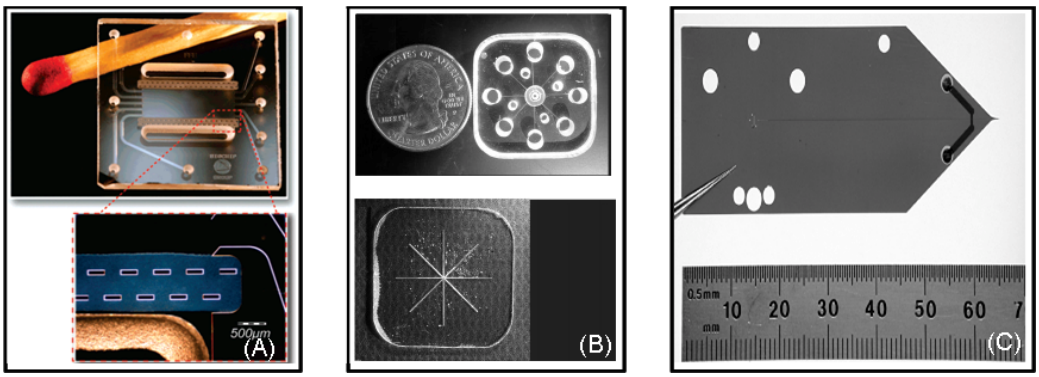

Figure 2.2: Recently developed applications of miniaturized separation systems, (A) a fabricated micro free-flow isoelectric focusing chip[11], (B) a micro gradient elution moving boundary electrophoresis chip[12], and (C) The early HPLC-Chip prototype developed at Agilent Labs[13].

The detection system is also an important part due to the low concentration and small output amount in μ-TAS. So the pre-concentration step was sometimes added before the detection step to enhance the sensitivity of the detection. Different kinds of detection methods such as optical, electrochemical or mass spectrometry systems based on the properties of the analytes are applied. Some new methods such as plasma detectors based on electrochemical technique and ion traps used in mass spectrometry[14] were discussed to optimize the detection systems.

All these microchips are fabricated on special substrates according to their functions.

2.1.1 Materials and Fabrication

Historically, silicon was commonly used as the substrate material to fabricate microfluidic systems[15]. Then quartz, glass and polymers took over[16] due to their insulating electrical properties and better fabrication feasibility. Now some materials such as Polymethylmethacrylate (PMMA) and Polydimethylsiloxane (PDMS) became popular in the investigation of single-using microchips because of their high chemical stability, good optical transparency, and various fabrication advantages. PDMS has compatibility with many organic solutions[17]-[19], hence the disadvantage of PDMS lies in taking the risk of being dissolved by some strong organic solvents such as chloroform. The solvent molecules can penetrate into PDMS substrate and lead to unknown leakage of analytes and solvents.

The choice of materials depends on the experiment requirements. Normally the following aspects are considered with experiences.

- the economical factors such as low-cost in a pure form,
- physical properties such as hardness and optical transparency,
- surface properties for chip bonding to other substrate,

- thermal and electrical properties,
- stability to chemical and biological reagents, and
- mechanical feasibility and applicability

Fabrication techniques are chosen according to substrate materials. Some well developed fabrication techniques, such as Lithographie Galvanoformung Abformung (LIGA), electro discharge machining, surface silicon micromachining, bulk silicon micromachining and self-assembly for submicron-size objects have been applied to chip fabrication. For PDMS substrate, templates based on daily life available materials[20] were modified and embedded in the chip fabrication. These methods can make the micro-devices considerably inexpensive. Recently, paper-based microfluidic chip was fabricated to cut the price into 3 cents per chip[21].

In the fabricated microchips, liquid flows obey the microfluid dynamics because of their small spaces. The microfluidic properties of fluid theoretically explain the flow behaviors in the microchips, and provide theoretical support for potential applications.

2.1.2 Microfluidic Properties

The concept microfluidics refers to any kind of theoretical and experimental study for liquid streams generated in micro-sized spaces. The typical dimension for μ-TAS devices is in the micrometer range. This small size has greatly increased the ratio of surface area to volume of the fluid, and induced special phenomena related to the surface characteristics[22]. Such phenomena include surface tension effects, capillary effects, diffusion effects, fast heating conduction effects and laminar flow effects. These characteristics can be explained by the microfluid dynamics.

According to the microfluid dynamics, the macro state variables (e.g., density

and temperature) do not change obviously over the length and time scales, when compared with the micro state variables such as molecular free path and molecular relaxation time. In microfluidic flows, the boundary condition controls the entire flow field and the flow profile is determined by the boundary condition. This simplifies the bulk fluid characteristics analysis such as temperature and concentration into only boundary condition analysis.

Microfluidic systems are often multi-physical systems governed by different forces. For example, pressure difference was used to drive liquid to flow through a channel; and at the same time, electric field was introduced to separate particles suspended in the liquid. The relevant physical properties change with the length scale L (m) of the microfluidic system. Table 2.1 shows the scaling relationship of some physical properties with the length scale L, when the velocity is a constant in all the cases[23]. Compared with pressure driven flows and gravity driven flows, shear driven flow has the simplest scaling dependence with L, which is in linear correlation. This property can be utilized to drive microfluidic flow more effectively, which is discussed in section 2.2.2.

Table 2.1: Dependence of physical properties with the length scale L in microfluidic systems, shear driven flow has the simplest scaling dependence with L.

Physical properties	**Relevance**	**Scaling dependence**	**Comment**
Viscosity	Flow with shear forces	L	For low Reynolds numbers
Pressure	Pressure driven flow	L^2	
Gravity	Dense flow or fluid mixtures with significant differences in density	L^3	
Surface tension	Flow of immiscible fluids	L	
Electrostatic force	Electrostatic single phase fluid flows	L^2	
Magnetostatic force	Magnetostatic single phase fluid usually with Lorentz forces in electric current flow	L^3	Fixed current density

Surface tension is the predominant force in multiphase microfluidic flows. Compared with electrostatic force and magnetostatic force in single phase fluids listed in table 2.1, surface tension has more effective driving influence on microfluidic flows.

The Reynolds number *Re* is always used to describe the flow condition of the fluid. Microfluidic systems have Reynolds numbers smaller than 1000 according to equation 2.1[24], where ρ (kg/m^3) is the fluid density, u (m/s) is the mean flow velocity and $\mu\left(\frac{kg}{m \cdot s}\right)$ is the dynamic viscosity of the fluid. The characteristic length scale l (m), which is often in the order of 100 μm, can also be the diameter of micro-channel if the channel is in round shape.

$$\mathrm{Re} = \frac{ul\rho}{\mu} \qquad (2.1)$$

Laminar flow occurs when *Re* < 2000, so the microfluidic flow is normally regarded as laminar flow due to the small *Re*. The laminar characteristic of microfluidic flow has a big impact on designing and manufacturing the microfluidic systems.

Compared with the convection flow occurs in pipes, fluids flowing in micro-channels only have the free diffusion effects due to the concentration gradient. Thus the diffusion coefficient D (m^2/s) is an important parameter in microfluid dynamics.

The simplified model for diffusion in microfluidic flow is the steady-state diffusion, where the time is so short that the concentration within the diffusion volume does not change with respect to time. D is defined by the velocity of diffusing particles, which depends on temperature, viscosity of the fluid and the particles size. In aqueous solutions, the diffusion coefficients of ions are in the range of $0.6 \sim 2 \times 10^{-9}$ m^2/s and the value of biological molecules normally range in

$10^{-11}\sim10^{-10}$ m^2/s. Taking the one-dimension steady-state diffusion as an example, the diffusion coefficient D can be defined by Fick's first law[25] (equation 2.2). J $\left(\frac{mol}{m^2 \cdot s}\right)$ is the diffusion flux in the diffusing volume, and C (mol/m^3) is the concentration in the position x (m).

$$J = -D\frac{\partial C}{\partial x} \qquad (2.2)$$

The microfluid dynamics in different microfluidic systems have different properties besides the common characteristics discussed above. Taking rotating microfluidic system as an example, the driving forces applied and the applications are especially discussed in the next section because of their importance in the research.

2.2 Potential Driving Forces in Shear Driven Circular Chromatography

Table 2.2 compares four important driving forces in microfluidic system. Hydrodynamic methods such as pressure driven, surface tension driven, shear force driven and centrifugal force driven were used for chromatography separations. Electrokinetically driven flows such as electroosmotic flow, electrocapillary flow, and electrohydrodynamic flow were all based on electric field.

In rotating microfluidic systems, centrifugal force and shear force are the two most important driving forces in the fluid dynamics.

Table 2.2: Comparison of microfluidic driving forces[26]

Comparison	Valve	Influenced by	Power source	Materials	Flow rate
Centrifuge	Only for liquids	Density and viscosity	Rotary motor	Plastics	From < 1 $nL \cdot s^{-1}$ to > 100 $\mu\ l \cdot s^{-1}$
Pressure	For both liquids and vapor	Generic	Pump, mechanical roller	Plastics	Very wide range (from < $nL \cdot s^{-1}$ to $L \cdot s^{-1}$)
Acoustic	None	Generic	Electric field (5-40 V)	Piezo-electrics	20 $\mu l \cdot s^{-1}$
Electrokinetic	Only for liquids	pH, ionic strength	Electric field (10 kV)	Glass, plastics	0.001-1 $\mu L \cdot s^{-1}$

2.2.1 Centrifugal Force

The commonly mentioned rotating microfluidic system is centrifugal force driven microfluidic system. This kind of rotating system requires no internal driving parts. The fluid propulsion from in to out is achieved solely by rotation of the disc.

Applying centrifugal force in μ-TAS has brought in a new technique named lab-on-a-CD (compact disk)[27]. To control the flow from spreading over the whole fluidic platform, channels and reservoirs were modified in a CD-like plastic substrate to complete centrifugation. The flow profile in centrifuge channels was laminar flow defined by small Reynolds numbers (< 100) and the mixing was carried out by pure molecular diffusion.

The recently reported applications based on lab-on-a-CD have accomplished more complicated functional tasks. For example, hydrophobic valves for discrete sample volumes controlling in nL range[28], capillary valves aligned sequentially to detect ions optically as shown in figure 2.3 (A); packed chromatographic

column for separating proteins (Quick Spin™ protein desalting column by Roche Diagnostics Corp, Indianapolis, IN)[1], and platform integrated for various biological functions such as cultivation and gene expression studies are shown in figure 2.3 (B). Nowadays, bio-CD used in the life sciences are reported as a new application field[29].

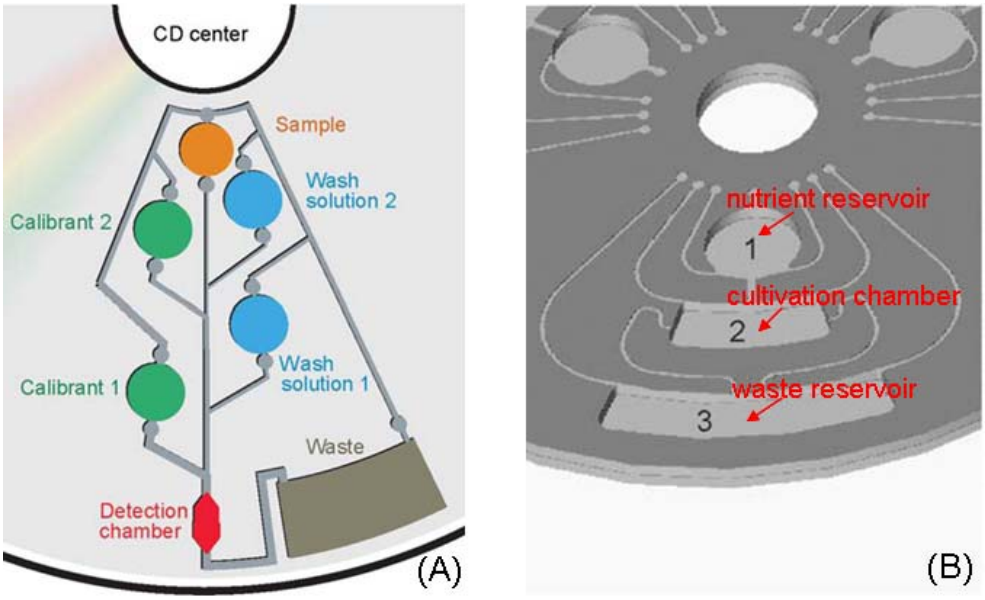

Figure 2.3: Schematic illustrations of the micro-structures for lab on a CD technique, which is based on the centrifugal force. (A) Capillary valves for the ion selective optode[30], which can be opened when rotation starts, and (B) cultivation system fabricated in two layers[31].

Besides lab-on-a-CD, micro centrifugal chamber fabricated for size exclusion purpose based on dynamic momentum change in microfluidic channels was reported recently[32].

In the shear driven circular chromatography experiment, the centrifugal force should be diminished. Because the centrifugal force will drive the sample out of the circular track, hence the sample is out of the detection region. Another force

[1] https://www.roche-applied-science.com

which is demanded in the experiment is the shear force.

2.2.2 Shear Force

Shear driven flows usually take place in micro-motors, comb mechanisms, and micro-bearings. For example, the flow between the stationary and mobile arms of a comb-drive mechanism is typical shear driven micro flow[33]. The simplest form is linear Couette flow (figure 2.4 (B)), which can be used as a prototype flow to represent fluid flows driven by a moving plate. The boundary condition at solid-liquid interfaces in micro-channels is taken as non-slip condition, which means that the velocity extrapolates to be zero in a certain distance behind the solid-liquid interface. The higher the driving rate is; the longer the non-slip distance will be. And the boundary slip length is longer on hydrophobic surfaces because the repulsion force between the liquid and the solid surface is stronger than that on hydrophilic surfaces.

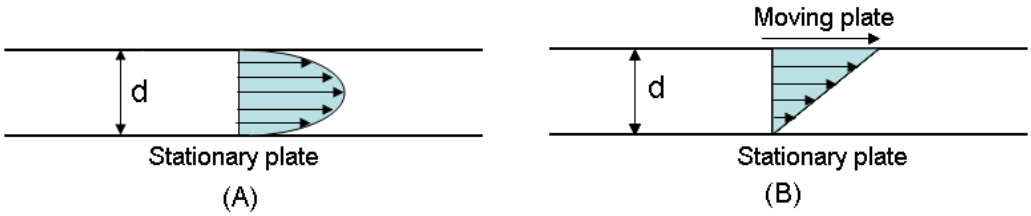

Figure 2.4: Flow profiles represent the fluid dynamics of (A) pressure driven flow, and (B) shear driven flow. The shear driven flow is simplified in to linear Couette flow with linear velocity profile.

Compared with pressure driven flow in the channel with the width of d in y dimension, shear driven flow has a longer mean radial distance where the sample species travel through. This is due to the bigger mean velocity of the fluid. In pressure driven flow, the velocity gradient is represented in figure 2.4 (A) and the flow profile is parabolic while shear driven flow has a linear flow profile (figure 2.4 (B)). Another difference between the two flows is the capacity of achievable

theoretical plate numbers in the chromatographic aspect. Due to the fact that the driving force for the open-tubular pressure driven flow is the pressure difference between both ends of the liquid stream, the channel length and the channel width are restricted by the Poiseuille's law[3]. But in shear driven liquid chromatography, the channel length and width have more freedom to achieve higher theoretical plate numbers.

Shear force was introduced into microfluidic devices by Luo et al to study droplets dispersion behaviors in two phase flow[34][35]. Shear force was also applied as a pumping force in the open or closed micro- and nano-fluidic systems to drive immiscible fluid layers to flow. Dietrich et al used oil covering water-filled micro-channels to simulate and prove the shear driven pump[36]. Other applications of shear force were reported to assist quantitative analysis of cell adhesion[37] and intracellular loading of cells with molecules[38] in microfluidic devices in life sciences.

Besides the dynamic properties brought by rotating shear force, in the shear driven circular liquid chromatography experiment, another important chromatographic property comes from the cyclic liquid chromatography method, which combines the benefits of miniaturized liquid chromatography and cyclic separation methods.

2.3 Cyclic Liquid Chromatography

2.3.1 Miniaturized Liquid Chromatography

The International Union of Pure and Applied Chemistry (IUPAC) [39] stated that "Chromatography is a physical method of separation in which the components to be separated are distributed between two phases, one of which is

stationary phase while the other moves in a definite direction".

In chromatography, the simplified separation behavior for two components is recorded in figure 2.5, and the separation ability of a stationary phase is defined by selectivity α (a.k.a separation factor). The selectivity α should be more than 1 if separation occurs efficiently. In the separation system for two components, this factor α is calculated by equation 2.3.

$$\alpha = \frac{t_{RB} - t_0}{t_{RA} - t_0} \qquad (2.3)$$

The dead time t_0 (s) is the time needed for a non-retention compound to be eluted from injection point to detection point. The dead time t_0 depends heavily on the stationary phase geometry and the mobile phase velocity. t_{RA}, t_{RB} (s) are the retention times for the two components are eluted out.

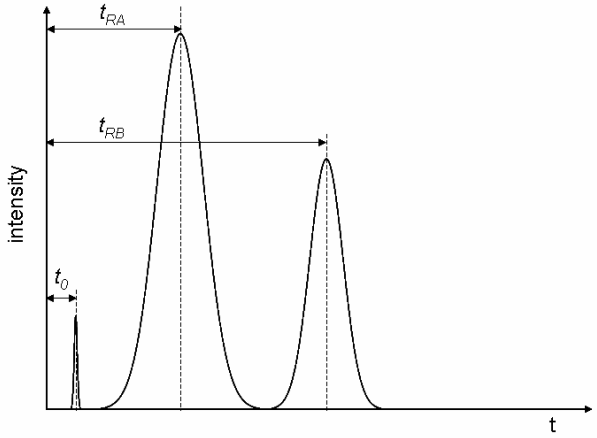

Figure 2.5: Chromatogram of two components. t_0 is dead time, t_{RA} and t_{RB} are retention time of the two components.

In liquid chromatography, the separation always takes place in a column. The separation efficiency of the column is defined by the theoretical plate number N (equation 2.4), which represents the succession of equilibrium steps. More steps in the column indicates the bigger separation efficiency with smaller band

broadening. In equation 2.4, t_R and w_b (s) are the retention time and the base width of the peak. If there are N equilibrium steps in a column of length L (cm), then the Height Equivalent to a Theoretical Plate (HETP) H (cm) is defined by: $H = L / N$, which is also used to describe the separation efficiency. N can also be represented with the peak height of a Gaussian peak and the width as a function of standard deviation δ (figure 2.6).

$$N = 16\left(\frac{t_R}{w_b}\right)^2 \qquad (2.4)$$

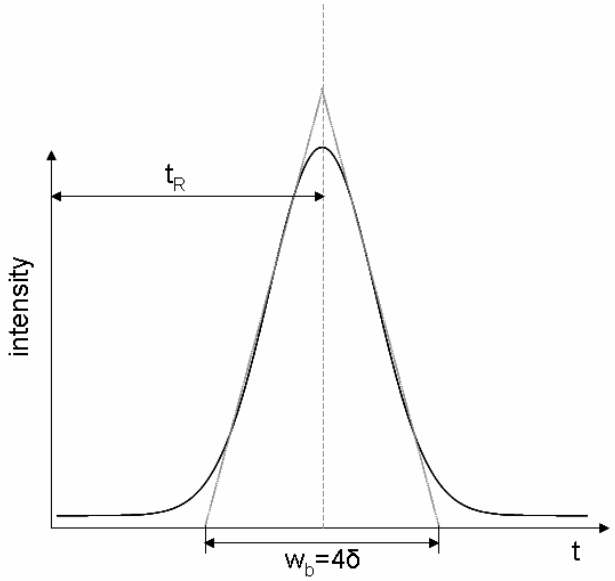

Figure 2.6: Representation of theoretical plate number N in chromatography. N is defined by the retention time t_R and the standard deviation δ.

Small non-porous particles ($\Phi \sim 1$ μm) were packed into the separation column (i.d. 5-10 μm)[40] in the prototype of miniaturized LC. The mechanical sealing problems occurred due to high pressure and the retention factors depended on the pressure change. Furthermore, the diffusion of component molecules and the mobile phase flow pathways in the stationary phase were affected by the flow velocity and column length, which were both determined by pressure. Hence, the theoretical plate numbers were restricted to be around 10^6[41].

The further developed method such as chip-based LC[42] was based on the standard particle-packing material and high pressure nano-pump. This technique integrated the pre-concentration column, separation column, capillary connector and electrospray emitter. The chip-based LC has been successfully applied to separate complex peptides mixtures, biomarkers, nucleolar proteomes and oligosaccharide samples[43]-[45]. Same as traditional LC, the theoretical plate numbers are restricted by the critical pressure and the particle size because the diffusion effect and heat transport are highly pressure dependent.

2.3.2 Cyclic Separation Method

Cyclic separation method is ideal to achieve potentially infinite separation length in chromatography. This approach can also be used to isolate certain components and carry out continuous detection. The cyclic method was firstly introduced in GC[4] as circular chromatography and has been used in CE for decades[46],[47]. From the electrophoretron[48] (figure 2.7 (A)) to the Synchronized Cyclic Capillary Electrophoresis (SCCE) as shown in figure 2.7 (B) and (C), the arranged capillaries increased from two to a number of polygon sides connected to form a closed loop.

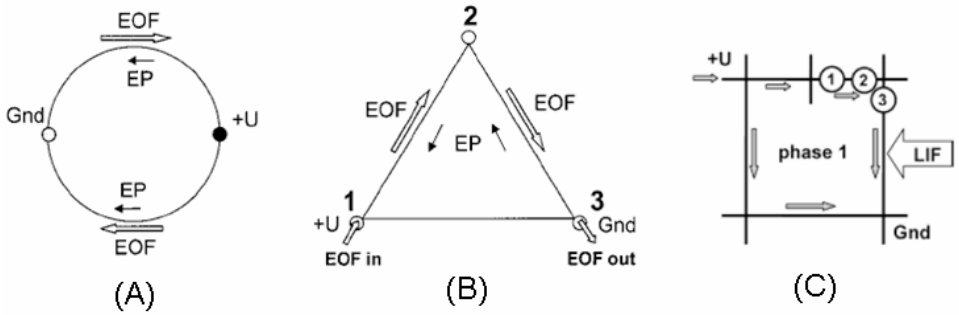

Figure 2.7: Schematic representation of (A) electrophoretron realized by two capillary channels with opposite surface charge, (B) SCCE with three capillaries to form a triangle to generate circular electric field, and (C) SCCE comprises a square geometry with easy voltage switching.

In SCCE, three or four capillaries were connected to form a triangle or square shape in a circular way (figure 2.7 (B) and (C)). With switchable voltage application, the analytes traveled with increasing number of cycles to achieve the same effects as that with high voltage, while the relatively low voltage applied accumulated with the cycles.

However, the side effects occurred with the polygon sides. They had enormous influence on the peak capacity and theoretical plate numbers because of the dispersion of the analytes in the corners[49],[50]. The theoretical plate numbers were limited to 10,000 per cycle due to decreased peak capacity, the Joule heating effect and the electroosmotic mobility. They were all dependent on the electric field applied.

With a combination of cyclic liquid chromatography and shear driven flow, shear driven circular chromatography is theoretically strong supported. The motivation and precursory research are introduced in the following section.

2.4 Shear Driven Circular Chromatography

In order to overcome pressure limitations in LC and voltage limitations in electrochromatography, shear force driven flow was developed by taking advantage of the intrinsic fluid viscosity. The shear driven flow was supposed to generate the moving mobile phase between two flat plates. Desmet group has developed a linear method since 1999 as shown in figure 2.8 and this system was compared with HPLC both theoretically[3] and experimentally.

The shear driven chromatography (SDC) was carried out in linear microfluidic channel which was about 300 nm deep. The stationary phase was reverse phase material such as alkanesilanes. The material was coated on the silica wafer or glass and the mobile phase was methanol and water mixtures.

With this method, fluorescein isothiocyanate-labeled angiotensins[52] were successfully separated. The detection limit was greatly enhanced[53] when the separation of four different coumarin dyes was reported one year later. The theoretical plate number was 2000–7000.

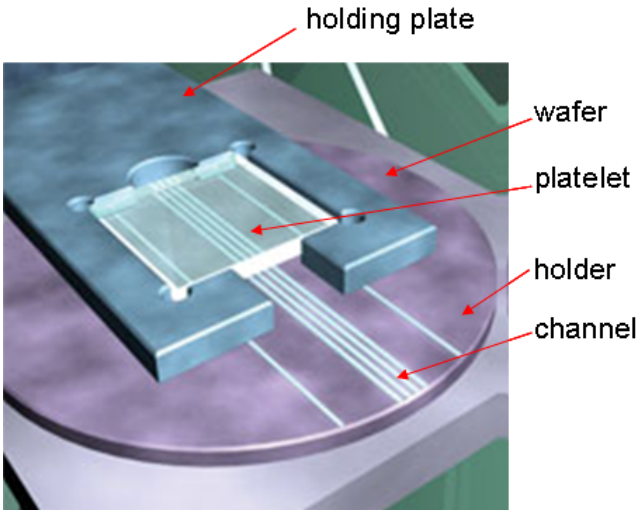

Figure 2.8: Assembled SDC device with silicon wafer on top and the metal holder beneath, where the SDC channel with an array of separated parallel channels were fabricated[51].

In order to obtain higher separation efficiency, shear driven circular chromatography (SDCC) was developed on the basis of shear driven linear chromatography. In SDCC, the linear channel was replaced by a circular channel, which has no input and output ends on both sides. SDCC proposes a way to achieve variable theoretical plate numbers, even to an infinite value, only by changing the number of cycles in the separation procedure (figure 2.9).

Previous SDCC setup[54] as shown in figure 2.10 demonstrates a prototype of SDCC with micro-channels.

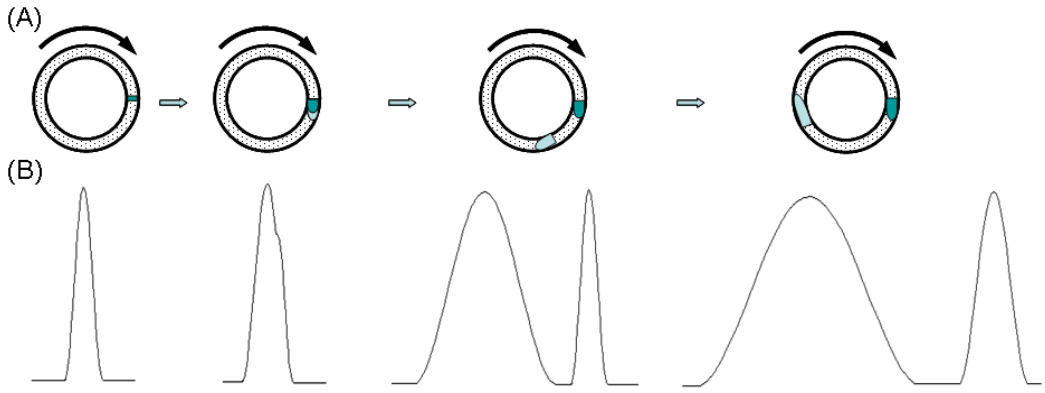

Figure 2.9: Schematic diagram of shear driven circular chromatography, (A) separation procedures of two components, and (B) signals according to the rotation steps.

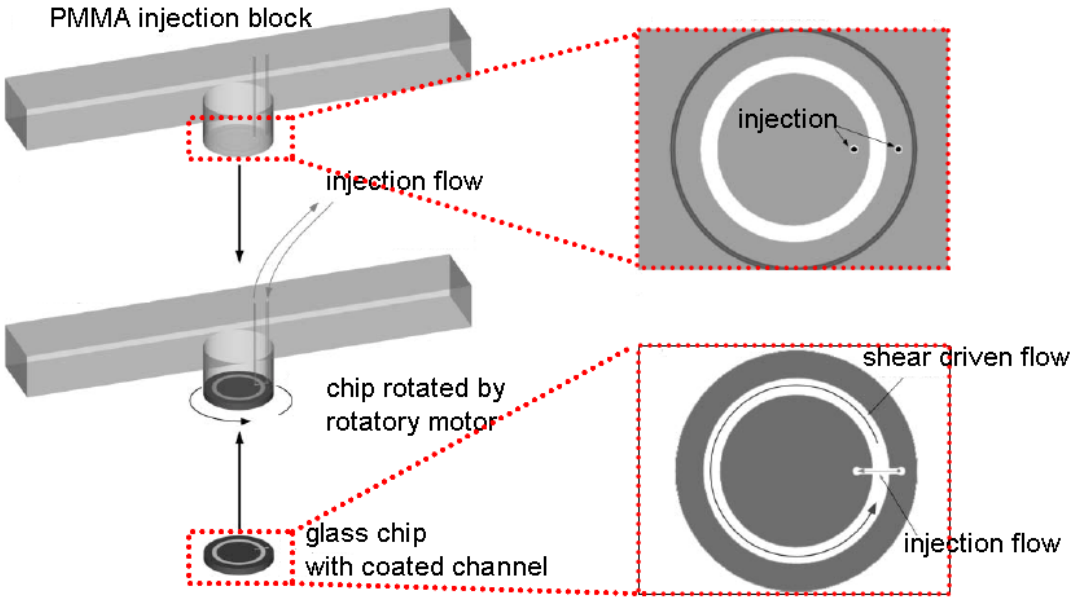

Figure 2.10: Schematic representation of device assembly and injection system[54]. The bottom glass plate contains a 15 μm deep channel etched on glass with an injection channel across. The top PMMA stationary bar remains fixed during the rotation of the bottom plate. The PMMA block also has a circular channel to hold the shear driven flow if the bottom channel is coated with too much stationary phase and even gets blocked.

In this system, the experiment was carried out in a 2 mm wide, 15 μm deep, donut-shaped channel fabricated on glass substrate. The mobile phase flowed with the speed of 1.423 $mm \cdot s^{-1}$. The reverse stationary phase C18 was polymerized and coated in the channel. This work proved that the shear driven fluid had exactly half the velocity of the moving plate, when the channel width was much greater than the channel depth.

However, there were many problems accompanying with this system. The existence of micro-channel added obstacle in stationary phase coating. It was very difficult to coat C18 in the channel precisely while still maintaining the homogeneity. Since the channel depth (15 μm) was much larger than that of the linear chips fabricated by Desmet's group, and the shear driven force was too weak to drive the sample to move in the channel. When the channel depth was comparable shallow, the freely rotating plate and the channel formed a half-open system. The unknown leakage out of the channel due to diffusion and centrifugal force was difficult to control. The channel wall couldn't avoid the sample leakage out of the channel, because there were gaps between the fixed glass plate and the rotating one. The thickness of the gap changed with the pressure added on top of the PMMA stationary bar.

We supposed that these problems can be reduced by carrying out experiment with two flat planar glass surfaces without any channel.

2.5 Summary

This chapter gives an overview of the theoretical basis and development of the SDCC method. The aim of μ-TAS is to serve analytical sciences in demanding fields, such as medical and clinical diagnosis[55] and single cell analysis[56]. However, as the fundamental prototype of microfluidic chips, further development

is necessary for the ultimate purpose to realize portable analytical instruments for daily use such as diagnosis whenever and wherever they are needed. As a novel miniaturized separation method, SDCC is conceived to realize controllable theoretical plate numbers and improve the separation efficiency.

CHAPTER THREE: A SHEAR DRIVEN ROTATING MICROFLUIDIC SYSTEM

3.1 Establishment of Setups

3.1.1 Choice of Materials

The choice of materials concerns many aspects including their physical and chemical properties that have been discussed in section 2.1.1. Here, table 3.1 summarizes the advantages and disadvantages related to our research. Since the rotating movement of the shear driven microfluidic platform is produced by a mechanical rotating motor, the mechanical hardness and stability should be considered in choosing material. Soda lime glass is chosen because it is the cheapest material with enough mechanical hardness to be fabricated among all the available materials, and it can best fulfill the experiment requirements.

Table 3.1: Comparison of possible materials in our experiment, glass was chosen because of its feasibility and physical properties.

Materials	Fabrication Technique	Advantages	Disadvantages
Silicon	Standard photolithography and wet-echting	High mechanical stability	Optically non-transparent, expensive
Glass	Standard photolithography and wet-echting	High mechanical stability, optically transparent,	Time-consuming fabrication and surface coating, expensive
PDMS	In-situ reaction molding[57]	Optically transparent, cheap, easy fabrication	Flexible, inefficient surface coating
PMMA	Injection molding[58] or LIGA	Optically transparent, cheap	Time-consuming fabrication, impossible surface coating

Two different geometrical types of soda lime glass plates are used in this experiment. One is glass plate in square shape with the size of 76 mm × 76 mm (Nanofilm, Westlake Village, CA, USA), and the other one is in round shape with the diameter of 50 mm (Edmund Industrial Optics, Barrington, USA).

3.1.2 General Experimental Setup

Two different mechanical setups were designed to build up rotating models for the shear driven microfluidic system. Both setups consist of stationary stage, rotatory stepping motor and microscope system (figure 3.1). The rotating momentum, which drove the microfluid flow in a circular way solely by shear force, was brought by the rotatory motor. The structure drafts of both designs are shown in section A.2.

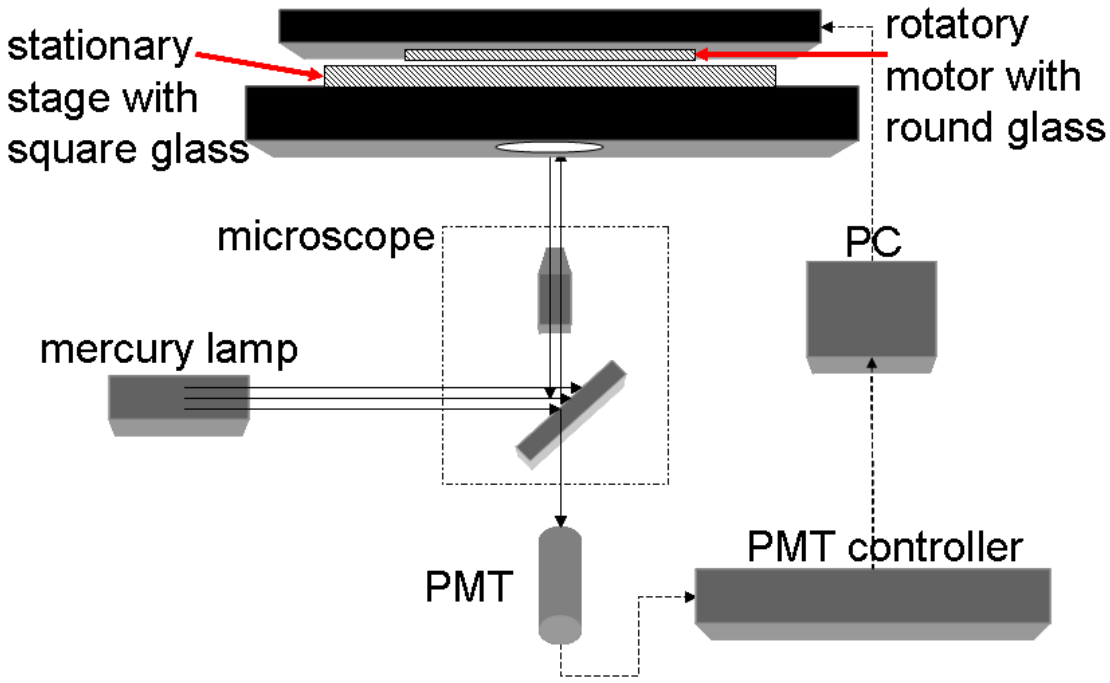

Figure 3.1: Schematic presentation of the experimental setup to represent shear driven rotating microfluidic environment.

In both designs, the microscope and detection system are the same; only the rotatory motors are different. The microscope system is composed of a Nikon ECLIPSE TE 300/200 Inverted Microscope with the TE-FM Epi-Fluorescence attachment (Nikon Corporation, Tokyo, Japan), a blue excitation filter block B-2A (Nikon Corporation, Tokyo, Japan) with the excitation filter at 450-490 nm, and a C-SHG1 super high pressure mercury lamp power supply with HBO 103 W/2 Mercury Short-Arc Lamp (Osram GmbH, Germany). The detection system has two detectors, one is CAIRN integrating photomultiplier controller with a Photomultiplier Tube (PMT) (Cairn. Research Ltd., Faversham, UK), and the other one is SONY XC-999P Charge Coupled Device (CCD) color video camera module (Sony Corporation, Japan). The rotatory motor for design A is a homemade motor and for design B is a stepping motor named PI M-062.PD Rotation Stage including power supply[1] (Physik Instrumente (PI) GmbH & Co. KG, Karlsruhe, Germany).

In both cases a liquid film was sandwiched between two flat glass plates. The square glass plate was laid beneath the round glass wafer, which was rotated by the rotatory motor.

Design A (figure 3.2) differs with design B (figure 3.4) in their rotating microfluidic conditions. For design A, the upper glass plate was fixed to the glass holder of the homemade rotatory motor by a vacuum pump. Both glass plates were fixed. Hence, the cover glass was relatively rigid to the plate underneath; and can't tune its position according to the bottom glass plate. When the surface of the glass holder was not precisely parallel to the stationary stage, the upper glass plate was correspondingly not strictly parallel to the bottom glass plate. The scratches on the bottom glass plate appeared after several rotation cycles (figure 3.3 (A)). More details are described in section A.1. The bottom glass plate was mechanically polished and the thickness of the liquid film in between changed with time during the rotation process. This unstable rotation condition led to unknown turbulence in microfluidic system.

[1] www.pi.ws

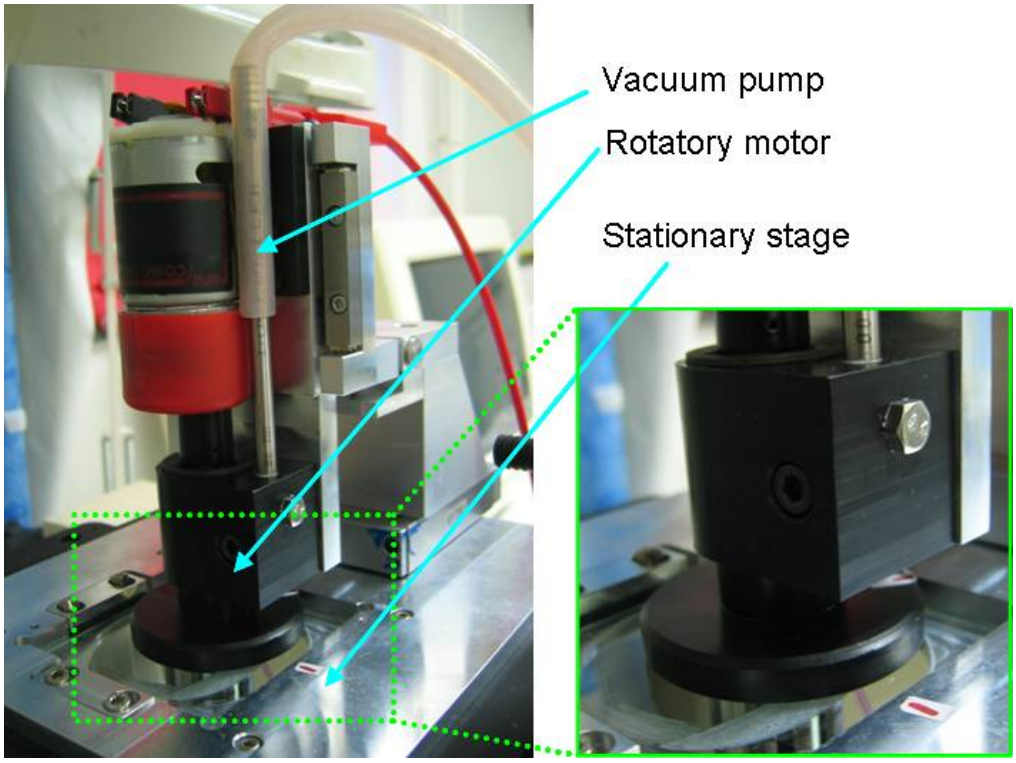

Figure 3.2: Experimental arrangement A with a homemade rotatory motor; and the round glass plate is fixed through vacuum pump with the motor. The rotatory motor has 1-dimension linear freedom of motion.

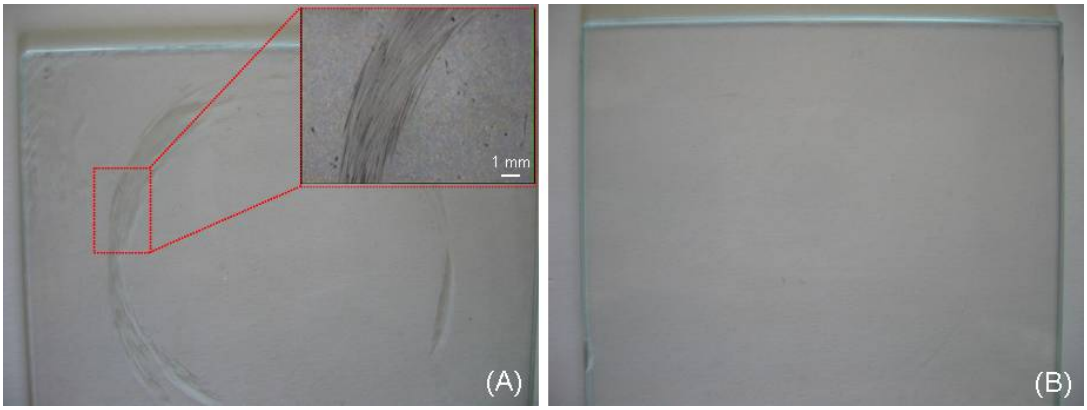

Figure 3.3: Quality of glass plate surface after rotating for 5 minutes (A) with design A and (B) design B. Pictures are taken by CCD camera. With design B, the scratches on the glass plate is avoided.

These problems can be solved by design B (figure 3.4) assembled with a PI stepping motor. The parallelity of the two glass plates was controlled by the weight of the stepping motor, which was measured to be 2.76 kg (equal to 27.05 N). Because the upper glass plate was fixed according to the position of the bottom one, this design provided much more stable rotating environment than that with design A. The stability is reflected by the surface property of the bottom glass after rotation as shown in figure 3.3 (B). The surface stayed clear and still smooth after rotation, without any scratches.

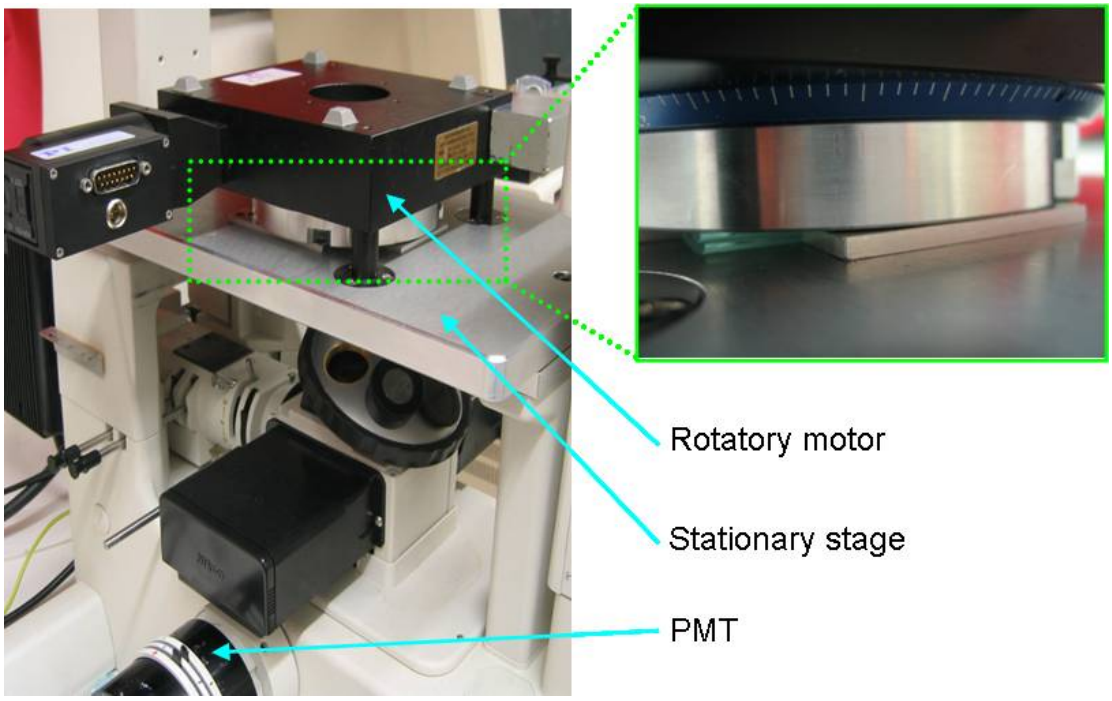

Figure 3.4: Experimental arrangement B with a PI stepping motor assembled with a glass holder made of metal. The glass plates are pressed together with relative parallel surfaces by the motor weight.

Another difference between the two designs lies in the mechanical movement of the rotatory motor. The homemade motor in design A has the freedom of motion in X-axis but the PI stepping motor in design B is fixed firmly with the stationary stage

to keep the parallelity. This movement freedom in design A makes the injection integration possible.

The design A is used to investigate particle motions under rotation in section 3.2.1 and is applied to integrate injection methods in chapter five. The design B is used in liquid film thickness measurement in section 3.1.3, to check fluorophore solutions rotating performance in section 3.2.3, and in SDCC experiment in chapter four.

3.1.3 Liquid Film Thickness Measurement

The estimation of scale is crucial in determining whether a system is a microfluidic system. The so-called “micro flow and nano flow” have the scale down to μm and nm as discussed in chapter two.

The thickness of liquid film can be determined by measuring electrical resistance or refractive index. The electrical resistance is proportional to the thickness of the liquid film and the light path length has the same property. In this experiment, Infrared Ellipsometry (IE) and volume-to-area methods were applied to identify the water film thickness between two glass plates.

Infrared Ellipsometry

IE measures the change of polarization property based on reflection or transmission of the material (figure 3.5 (A)). The polarization changes with the material's physical properties such as thickness, complex refractive index and dielectric tensor. Ellipsometry can achieve Ångstrom resolution when exploits phase information and the polarization of light.

IE method is assumed to measure the thickness of ultra-thin films within μm or nm scale. It was used to characterize the organic film-on-substrate samples[59] and the influences of inhomogeneities on thick film[60]. The sample must compose discrete, well-defined layers that are optically homogeneous and isotropical**.**

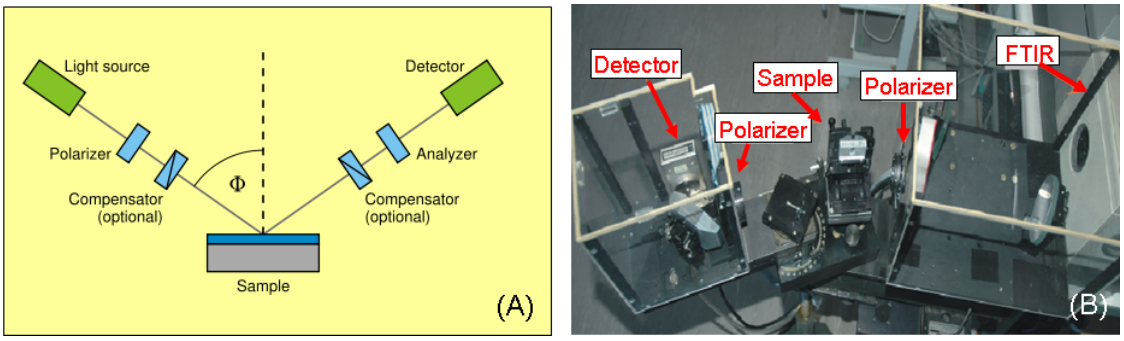

Figure 3.5: Illustration of (A) ellipsometry principle and (B) IE experimental setup. IE is used to measure the thickness of the mobile phase film in between two glass plates.

For example, the refractive index of air is 1 and silica is 3.42, hence, the property of materials in different layers such as silica-air-silica can be measured by refractive index changes.

In this study, IE measurements were carried out with the homemade IE setup designed by Institute for Analytical Sciences (ISAS) in Berlin shown in figure 3.5 (B). The samples were laid standing according to the instrument instead of lying in the traditional IE measurements. The spectral range of the stretching vibrations of the water reveals that detection of a water film down to 1 nm should be possible with this IE instrument.

Since the water film was sandwiched between two glass plates, the refractive index changed on glass-water-glass surfaces twice and the thickness of water film could be thus calculated. However, the refractive indices are similar for glass and water, which makes the thickness of water film difficult to be determined. Then the silicon-water-glass sample was used to replace the glass-water-glass sample. The surface roughness of the silicon wafer should be the same as the substituted glass plate; otherwise the thickness of the water film would be different.

Figure 3.6 illustrates the experimental outcomes. Figure 3.6 (A) is the graph for silicon-air-glass sample as a reference measurement for calibration. Figure 3.6 (B) shows the thickness of water film, which is sandwiched between silicon wafer and glass plate. The spectra of 30 nm and 300 nm water films were measured as

references to determine the spectrum of water film with unknown thickness. A thickness range instead of precise value was obtained. The water film was determined to be thicker than 300 nm, which was beyond the detection limit of the available IE instrument. Since the IE method was not able to measure the thickness of water film, another method by measuring the volume and area of the water film was employed.

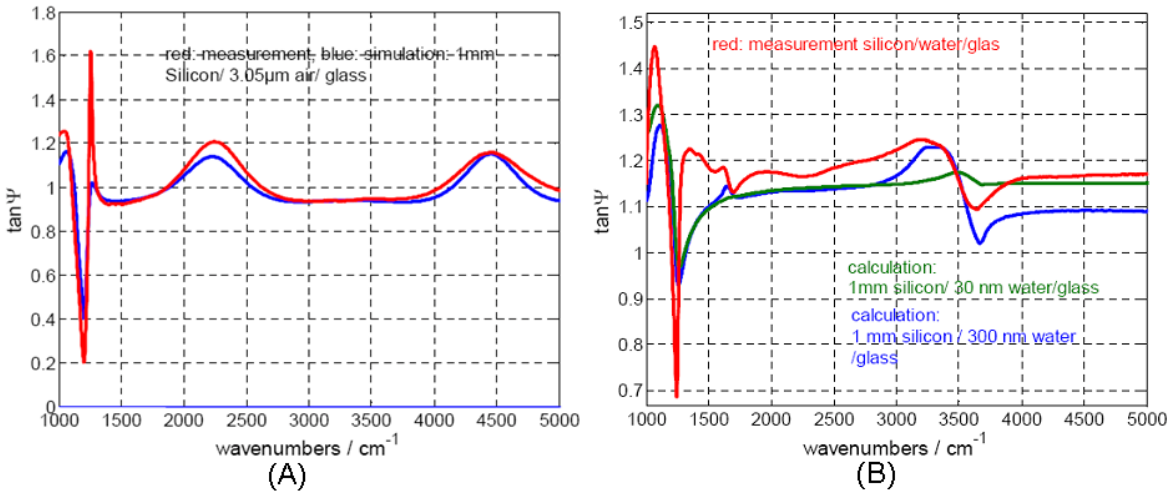

Figure 3.6: Measured and calculated tan Ψ spectrum of (A) silicon-air-glass sample for instrument calibration, and (B) silicon-water-glass sample. The thickness of water film is between 30 nm and 300 nm, but the precise value can not be decided by IE.

Volume-to-area

When the volume V (µL) and area A (mm^2) of a portion liquid are known, the thickness d (µm) can be derived by $d = V / A$. In this experiment, the d of water film between two glass plates was determined by measuring the area of the water droplet with defined volume. In order to eliminate capillary force on the hydrophilic surfaces, the glass plates were silanized to be hydrophobic. The silanization process was the same as described in section 4.1.2 for the SDCC experiments.

1 µL of dye in water solution was perfused by syringe onto the silanized glass plate and the other glass plate was laid immediately on top. The area of the dye

droplet was recorded by CCD camera and then obtained by CorelDRAW 12. Three samples are listed in table 3.2 and the average thickness of water film is calculated to be around 26.7 μm.

Table 3.2: Parameters in volume-to-area experiments, images are taken by CCD camera with bars, areas are acquired with CorelDRAW 12, and the thicknesses are derived by $d = V / A$. The average thickness of the mobile phase film is about 25 μm.

Images taken by CCD	Volume (μL)	Area (mm^2)	Film thickness (μm)
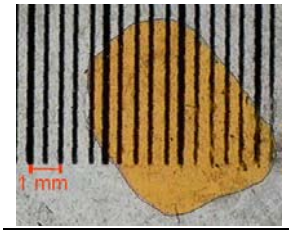	1.0	31	32.3
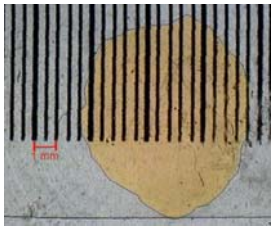	1.1	47	23.4
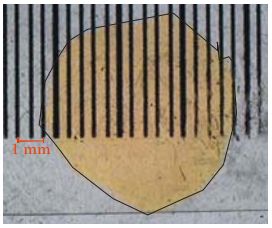	1.0	41	24.4

After the establishment and characterization of the microfluidic system, each setup was given different task according to its characteristics. In order to study the feasibility of validate shear driven circular liquid chromatography and integrability of injection system with these setups, specific experiments were designed and the further characteristics of these setups were checked.

3.2 Applications of the Rotating Microfluidic System

In earlier rotating microfluidic systems, microvalves, microchannels and other integrated internal parts were arranged in a certain sequence to achieve various aims[61] solely by centrifugal force. For example, the microvalves on the rotating platform were used to control the fluid flow, while the opening of the microvalves depended on the rotation frequency of the rotating platform, the channel dimensions, and the physical properties of the microfluidics.

In our rotating microfluidic system, the centrifugal force was not required and the centrifugal effect should be eliminated. So the rotation frequency was kept low. The fluorescent particles were studied to understand the influence of the centrifugal force.

As supplementary information, the rotation effect of immiscible liquid layers is discussed in section A.3 for potential applications of this system. While droplets of one fluid in another immiscible fluid flow in micro-fluidic system are used widely in food chemistry and pharmacy fields. The special distribution and dispersion properties provide big potentials for emulsion study[35].

3.2.1 Fluorescent Particles

The sample solution was prepared with 2 mM FluoSpheres® carboxylate-modified microspheres in water. This solution has yellow-green fluorescence (505/515) with 2% solids. Two different sizes of particles were prepared: Φ 0.1 μm and Φ 2 μm (Invitrogen, USA).

Experiment:

A small aliquot of water solution with fluorescent particles was injected by syringe onto the silanized glass surface followed by perfusing water droplets all around the glass plate. Another glass plate was laid on top carefully to drive out air

bubbles. Then the stepping motor was fixed and started to rotate. The images in time sequences were recorded by CCD camera and the fluorescent intensities of 2 μm particles are shown in figure 3.7.

The bright parts in figure 3.7 are fluorescent particles. They appear with specified time interval determined by the rotation frequency. As shown in the image sequences, the bright areas show up during every cycle at almost the same position on the glass. The time interval between each cycle is about 3 s. This phenomenon indicates that the centrifugal force has very little influence on this microfluidic system, because the propulsion effect induced by centrifugal force is very limited. The particles are driven mainly by shear force occurs in the circular track other than being driven out to the edge.

In the experiment, the intensity changed irregularly because there were some fluorescent particle residues sticking on the rotating glass plate, and the amount was changing during rotation. This uneven distribution of the fluorescent particles on the rotating plate could be improved by diluting the solution, but led to too low intensity to be detected.

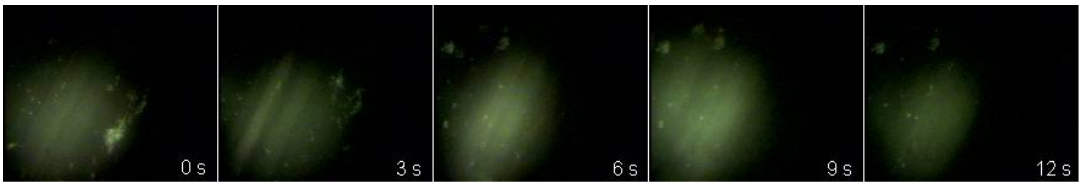

Figure 3.7: Distribution changes of fluorescent particles with time recorded by CCD camera. The rotation frequency is 1.37 Hz and the particle size is 2 μm in diameter. The centrifugal force is proved to have no influence while the fluorescent particles stay in the same track every cycle.

The centrifugal force *F (N)* can be calculated by equation 3.1, where *r* is 9 mm and *f* is 1.37 Hz. The centrifugal acceleration *a* is 0.666 m/s^2, which is much smaller than the gravity acceleration *g* (9.8 m/s^2). Therefore the centrifugal force can be

omitted with the particles when the frequency is as small as 1.37 Hz. This result explains the experimental results shown in figure 3.7 from the mathematic aspect.

$$F = m \cdot a = m \cdot (2\pi f)^2 \cdot r \quad (3.1)$$

Another experiment was designed with the same rotation frequency but the size of particles was changed. The fluorescent intensities taken by PMT are shown in figure 3.8 as a comparison of rotation behavior for different particle sizes within the same time period (~ 40 s). The regular peaks appear almost every 0.8 s are assumed to be due to the particle residues or diffractions on the rotating glass plate. This graph shows that there are more periodic peaks with 0.1 μm particles (figure 3.8 (A)) than with 2 μm particles (figure 3.8 (B)).

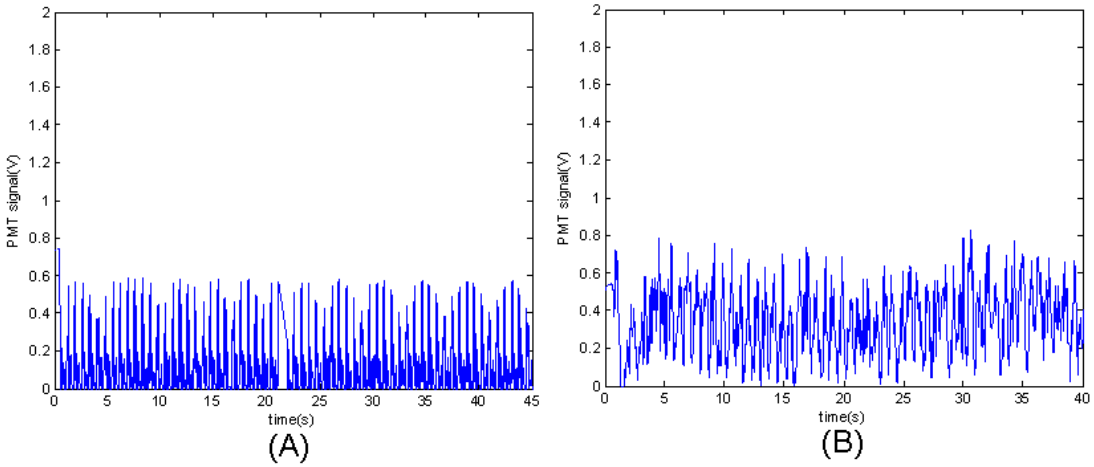

Figure 3.8: Fluorescent intensities of fluorescent particles with diameters of (A) 0.1 μm and (B) 2 μm rotating at 1.37 Hz. More periodic peaks appear with 0.1μm particles. The regular peaks appear every 0.8 s are the residues or diffractions on the rotating glass plate.

But from the graphs, it is difficult to get more information other than fluorescent intensities for the individual or collective behaviors of the fluorescent particles. Hence, Fast Fourier transform is used to get more time information for our rotating platform.

3.2.2 Frequency Analysis

Fast Fourier transform (FFT) is an efficient algorithm to compute the discrete Fourier transforms (DFT) and the inverse[1]. FFT is of great importance to analyze periodic signals for signal processing in the finite field. The cyclic filter banks were built up to simulate analysis in many applications such as image subband coding[62]. In this experiment, the cyclic signals showed up were assumed to be analyzed by FFT to increase the S/N ratio. The frequency information was extracted from the time information, and each group of regular periodic peaks should have a single peak in the frequency graph.

FFT Functions:

If a given signal $x(t) = x(t+T)$ is periodic with the time period T (s), its spectrum is discrete with frequency interval $f = 1/T$. FFT can be derived with equation 3.2 from a series of periodic signals in an infinite time period.

$$X(f) = \int_{-\infty}^{\infty} x(t) e^{-j2\pi ft} \cdot dt \qquad (3.2)$$

Many simulation functions are developed to filter out undesired frequency peaks. Different FFT functions are chosen for different analyzing purposes. One of the functions commonly used is named wavelets function. It is explained by equation 3.3 where *a* and *b* are undefined parameters. This function is not to replace the Fourier transform but merely as a de-noising step to increase the S/N ratio:

$$F(x) = \int_{-\infty}^{\infty} e^{-\frac{x^2}{a}} \cdot \cos(bx) \cdot dx \qquad (3.3)$$

Another function called Shah Convolution Fourier transform (SCOFT)[63], which has been recently applied to CE microchip analysis[64], multiple-sample injection technique[65], and particle flowing velocity measurement[66]. SCOFT is unique in

[1] http://en.wikipedia.org/wiki/Fast_Fourier_transform

analyzing linear signals in a separated multiple detection. The continuous linear signals can be detected in a sequence of discrete signals with defined time intervals as shown in figure 3.9. The time intervals are controlled by a homemade device with slots aligned in certain distances. This device is used to cut the continuous signal into discrete and periodic ones. So the continuous time domain signals are successfully transferred into frequency domain signals.

SCOFT can be used in this experiment for linear separation analyzing, if the rotating microfluidic platform is further miniaturized in the future that the whole platform can be observed under the microscope. But now only a small part of the platform was able to be seen by the microscope at one time, so the continuous fluorescent signals were detected every cycle when they reached the detection window. The periodic signals were transferred by plain FFT to investigate the rotation condition.

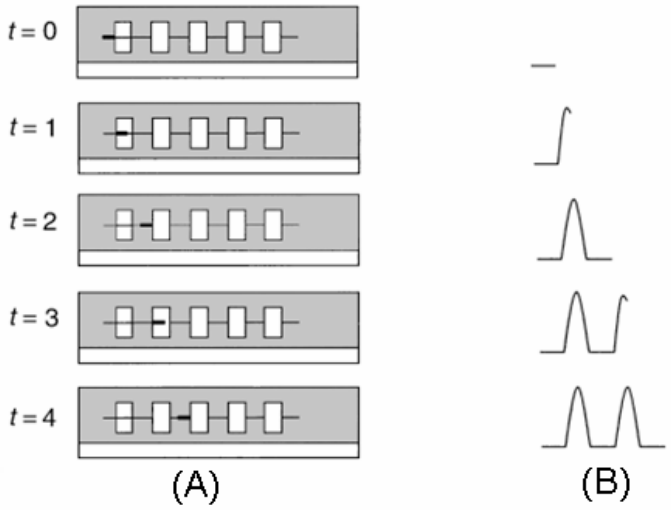

Figure 3.9: Illustration of SCOFT function in transferring (A) linear continuous signals with a homemade device into (B) discrete periodic signals. The time interval is defined by the distance between two detection slots of the device, and the flow rate of the sample.

In order to obtain better resolution with FFT, the practical way is to collect data for a longer time period.

Data Collection Time

FFT signals are discrete with frequency spacing between continuous data points in the frequency domain graphs. This is defined by $\delta_{(s)} = S_{scan} - rate/n$, where $\delta_{(s)}$ is the frequency spacing and n is the total number of input points[67]. The simulated peak can reach closely to its true height and shape by changing S_{scan} and n. If n increases but S_{scan} stays constant, the $\delta_{(s)}$ will decease. This means if the narrower peak width is needed, more data points should be collected to define the peak. This can be achieved by collecting the raw data for a longer time period. Meanwhile, longer time period of data collection contributes to better resolution in FFT analysis because of more time information. The function: $y = \sin x$ is taken as an example, the resolution of y is better with narrower peak width at 0.16 Hz for a longer time period (figure 3.10 (B)) compared with that of a shorter time period (figure 3.10 (A)). For x from 1 to 50000 in figure 3.10 (B), n is bigger and thus $\delta_{(s)}$ is smaller than that for x from 1 to 500 in figure 3.10 (A), and more data are collected to form the peak.

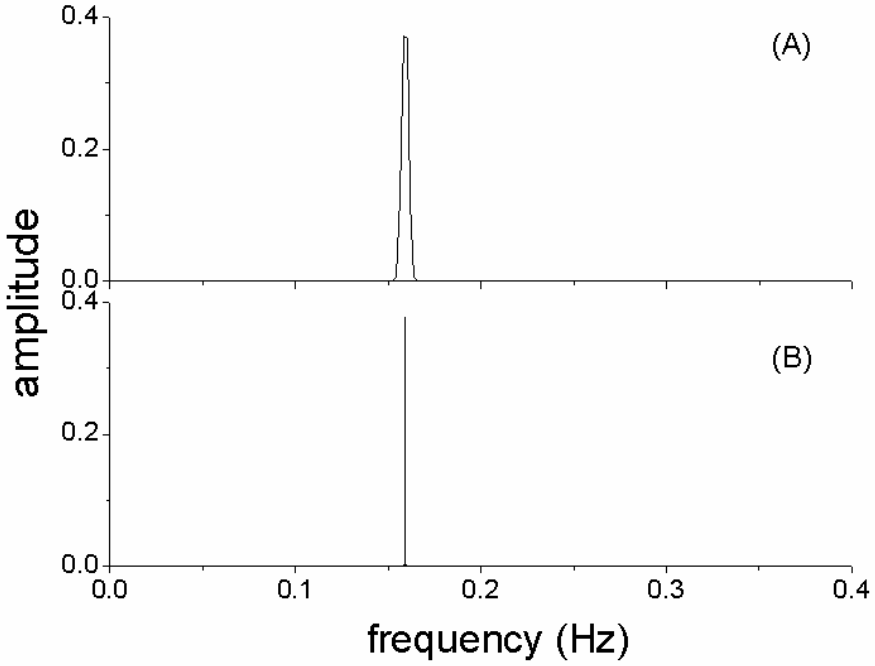

Figure 3.10: Theoretical illustration of FFT analysis for different time durations. (B) longer time period for more data collection has superior peak resolution than (A) shorter time period.

This theory can be used to increase the resolution of FFT peaks in the SDCC experiments described in section 4.2.4. However, the study of the rotating performance of fluorescent particles is only to check the influence of centrifugal force. Hence only plain FFT function is capable.

Results:

In our rotating microfluidic system, the rotation frequency of 1.37 Hz was chosen to analyze the movement of fluorescent particles under rotation (figure 3.8). The frequency information of the particles with the size of 0.1 μm and 2 μm in diameters were compared in figure 3.11.

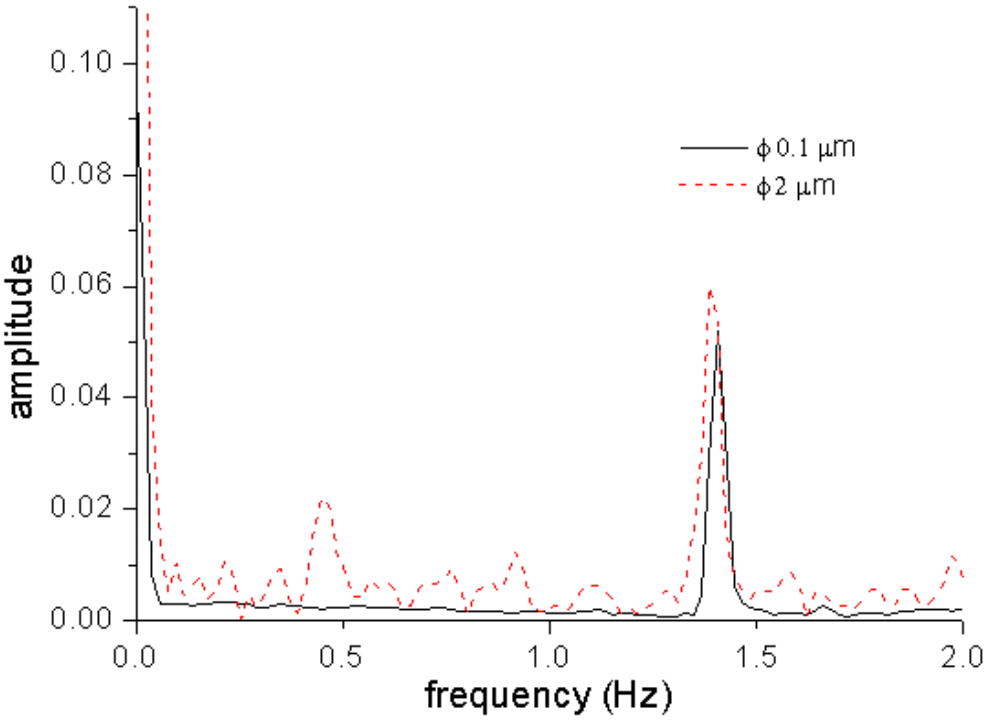

Figure 3.11: Frequency information of 0.1 μm and 2 μm particles rotating at the frequency of 1.37 Hz. The FFT is done by Origin 7.0. Peak at 1.37 Hz is the periodic signal of residue or light diffraction and reflection with the rotations.

The comparison of the frequency information shows that the particles with bigger size have more motion freedom compared with smaller ones, since bigger particles show more peaks on the frequency graph. For the particles with both sizes, the signal at 1.37 Hz, which equals to the rotation frequency, comes from diffraction or fluorescent residues on the rotating glass. However, 2 μm particles have many small peaks between 0 and 1.37 Hz. These peaks attribute to free diffusion and random movements of the big particles or their aggregations under the shear force, albeit the particles diameter (Φ 2 μm) are relatively small to the microfluidic film thickness (20 μm). There is no clear peak at about 0.7 Hz, which is half of the rotation frequency. This phenomenon indicates that most of the particles do not move at the same speed with the mobile fluid. With the 2 μm particles, a distinct peak at about 0.5 Hz is observed. This peak indicates that a great amount of particles move 0.2 Hz slower than the mobile fluid.

For the 0.1 μm fluorescent particles, no obvious peaks show up in the graph. Therefore the detection limit has to be enhanced in order to study particle movement. Some new methods concerning the light source, special NA filters, and pre-treatment of the samples were reviewed[68] towards high-resolution and high-sensitivity fluorescent devices integrate with lab-on-chip devices.

Since fluorescent particles are investigated to get the conclusion that centrifugal force has little influence when the rotation frequency is not higher than 1.37 Hz in our rotating microfluidic system, and FFT analysis is proved to be an effective way to analyze periodic signals. Based on these results, preliminary experiment is designed to check the feasibility of design B for chromatography applications.

3.2.3 Fluorophore Solution

A small aliquot of fluorescein solution was rotated in water environment for 30 s with design B. On the images taken by CCD camera (figure 3.12), a circular track is formed other than an area.

This observation indicates that the boundary is successfully established in our system, and design B is capable in carrying out microfluidic separation experiment. If the separation can be completed in such a short time, the separation efficiency will be high.

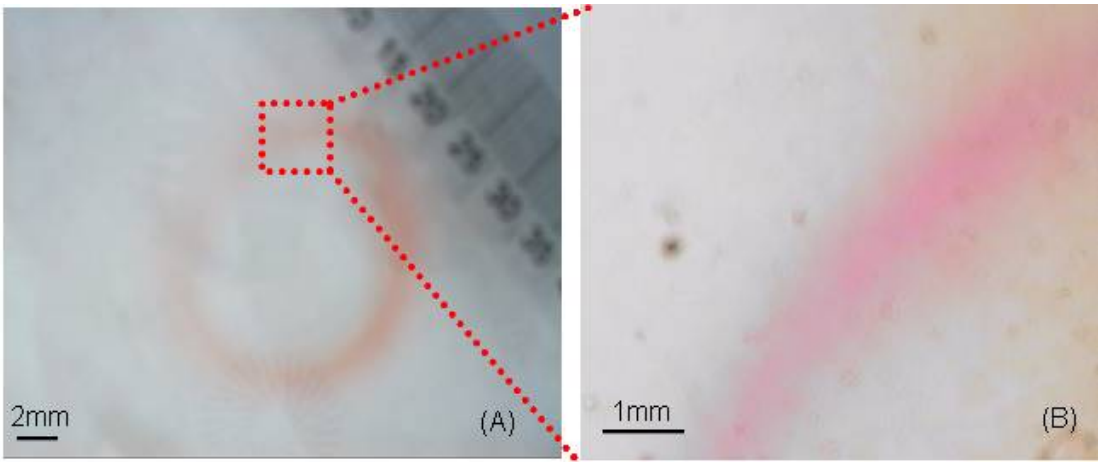

Figure 3.12: Images of (A) flow track overview and (B) amplified part for fluorescein after rotating for 30 s with 2 Hz. Due to the diffusive balance in microfluidic system, the average width of the track is about 0.5 mm.

3.3 Summary

In this chapter, a system was successfully built up to produce rotating momentum to drive the microfluid flow in a circular way. Two setups were designed with different rotatory motors. Their benefits, drawbacks and potentials are summarized in table 3.3.

Table 3.3: Comparison of two setups designed in our work, design A is suitable for integrating future injection process and design B is proper for circular shear driven chromatography experiments.

Setup	Advantages	Disadvantages	Applications
A	Motor has X-axis motion freedom, rotation frequency range: 0.5-50 Hz[1]	Rigid in Z-axis, induces turbulence and scratches on glass plates, rotation frequency is unstable	Potential to integrate injection process
B	Stepping motor has flexibility in Z-axis, two glass plates can be tuned to be parallel, rotation frequency is stable	Fixed in X- and Y-axis, rotation frequency range: $\leq$ 2 Hz	Validate circular chromatographic method

[1] The rotation frequencies are recorded by stroboscope.

Using the fluorescence intensity to detect the movement of freely diffusing fluorescent particles was reported to be a sensitive method to investigate the tracking and controlling of small particles[69]. Here, the frequency information contained in the periodic discrete fluorescent signals was extracted out by FFT. Besides free diffusion, the movement of particles is also influenced by the shear force.

Various applications of microfluidic flows in micro-channel or nano-channels were reviewed[70], and the fundamental prospect for lab-on-chip devices is based on multiphase flow. In this experiment, the wall of micro-channel was defined by hydrodynamic stability of shear driven flow instead of the solid channel walls. The diffusion equilibrium in a short time period made the temporary establishment of multilayer boundaries possible. The boundary formed restricted the dispersion and exchange flows between multiphases. The concentration gradient of microfluidic layers was also able to be restricted [71].

CHAPTER FOUR: CHANNEL-FREE SHEAR DRIVEN CIRCULAR LIQUID CHROMATOGRAPHY

4.1 A Channel-free System

Fluid flows in micro-channels can be controlled by the combination of channel geometry and surface modification to vary the boundary effects[72]. Two layers of microfluidic flows have been introduced to accomplish chromatographic separation with high speed[73] in a single channel. Another kind of micro-channels has been built with the porous material in microfluidic methodologies[74]. This model produced more than 5000 micro-channels in the networks of the porous packed media. In the centrifugal rotating microfluidic system, the micro-channels always display three-dimensional micro-structures, which offer the spaces for the centrifugal force to create an artificial gravity and continuously drive the microfluidic flow in the radial direction[75]. In a summary, the traditional concept of "channel" in the microfluidic system is always relevant to the spaces formed between two solid side walls.

In this experiment, a novel channel-free method was developed. No solid channel wall exists; instead, two flat glass plates are where the chromatography takes place. The stationary phase was then coated directly on the glass surface.

4.1.1 Introduction to Stationary Phase

In reverse phase liquid chromatography (RPLC), the stationary phase is non-polar and the mobile phase is polar. The stationary phase is hydrophobic in physical property, and it must be stable against the dissolution caused by the solvent in mobile phase, and must be chemically inert to both the mobile phase and the analytes. The

stationary phase also has to be stable to the shear force induced by the flow. Most commonly used stationary phase is octadecylsilane (ODS), which is bonded to a silanol function group with a chemical bonding named siloxane linkage[76]. The reaction process is shown in figure 4.1.

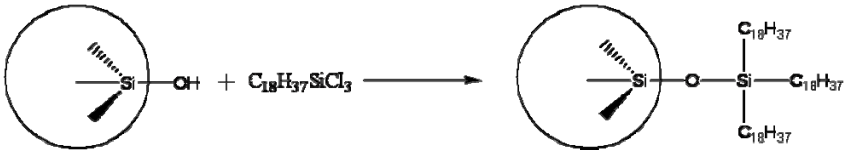

Figure 4.1: Reaction of silanol function group with tri-functional ODS. With this reaction, the stationary phase of C18 is coated on the glass plate for the following chromatography experiments.

The selectivity of stationary phase varies with the length of alkane chain and the coating property. ODS is chosen because of its good separation ability for many components. The silanol function group located on the fully hydrated surface has the steric restriction to react fully with silane solution. Different types of silanol groups on the glass surface exhibit different reactivity to silanes.

The soda lime glass used in this experiment has the chemical composition of $12.3Na_2O \cdot 5.5MgO \cdot 8.9CaO \cdot 1.1Al_2O_3 \cdot 72.2SiO_2$[77], which means the chemical structures on the surface is inhomogeneous. The inhomogeneity provides various reaction sites on the glass surface. Porous silicon[78] and monolithic silica column[79] have been investigated to substitute the silicon substrates used in shear driven linear chromatography. In this experiment, ODS was directly coated on the whole flat soda lime glass surface in order to overcome channel restrictions.

4.1.2 Coating Process

Reverse phase coating process consisted of two steps: pretreatment and silanization. In both steps, several methods were compared and the best approach was chosen. In the pretreatment step, the glass plate was firstly washed with deionized water and ethanol, and pretreated in different ways. In the silanization step, pretreated

glass plates were silanized with the 30% (v/v) n-octadecyltrichlorosilane ($C_{18}H_{37}SiCl_3$, 90%, cont. 10% branched isomers, Sigma Aldrich Chemie GmbH, Germany) in toluene (Merck, Germany) solution with different methods. The silanized glass plate was rinsed with toluene and dried at room temperature with nitrogen. At last, the prepared glass plates with C18 coating were heated in the oven at 70 ^{o}C overnight to firm the bonding.

Pretreatments

The basic function of pretreatment is to clean the soda lime glass surface, and remove the handicaps and contaminants. Furthermore, it can also activate the silanol function groups. In our experiment, O_2 plasma, piranha solution (3:1 (v/v) concentrated sulfuric acid to 30% hydrogen peroxide solution) and 2% (v/v) HF solution were tested. Homemade O_2 plasma cleaner (figure 4.2) can oxidize the glass surface so that more silanol function groups are added.

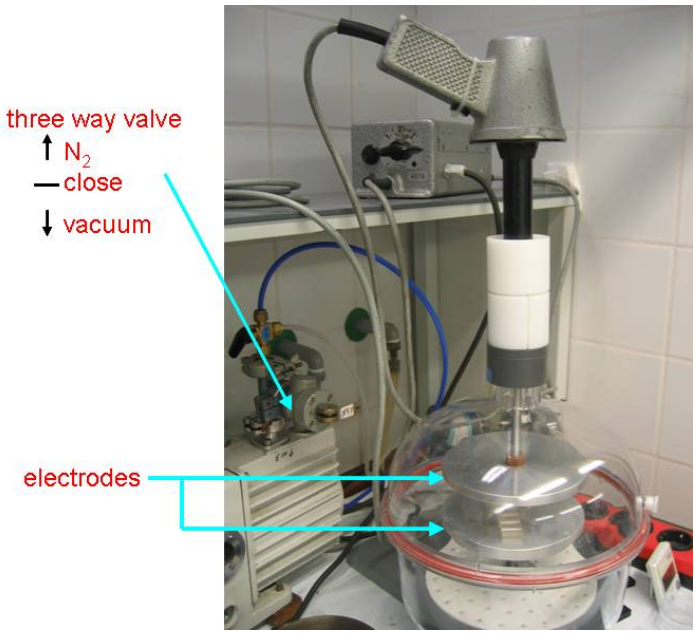

Figure 4.2: Photo of homemade O_2 plasma cleaner used for pretreatment. Glass surface needs 1 minute plasma treatment to clean and activate the surface.

Piranha solution enables stronger oxidation and hydrolysis to provide more silanol function groups. Both pretreatments do not change the surface topography, but pretreatment with HF solution roughens the glass surface to increase the silanization sites.

All these pretreatments keep the surface hydrophilic and do not change any chemical properties. After pretreatment, spin coating, vapor deposition and immersion methods were introduced for silanization. The glass surface has to be freshly prepared and immediately silanized.

Spin Coating

The spin coating process was programmed to rotate at 8.3 Hz for 5 s and afterwards at 24.9 Hz for 15 s. A drop of C18 solution with the volume of 1 mL was dropped by a syringe in the centre of the glass plate, and the rotation started. After the rotation, the glass plate was heated on hotplate at 110 ^{o}C for 1 min.

The surface properties of glass plate after spin coating are recorded by microscope (figure 4.3).

The inhomogeneity coming from spin coating is mainly because that the glass surface is hydrophilic but the C18 solution is hydrophobic. The compatibility of glass surface and C18 solution is low, so the C18 drop splits into small droplets and accumulate as small spots on the surface other than spread evenly as a film. The droplets in the center (~ 0.5 mm in diameter) are bigger than these at the border (~ 0.1 mm in diameter) due to weaker centrifugal force in the central part. After the toluene was removed, solid accumulations other than a solid layer were left on the glass surface. When the volume of C18 increased to 2 mL, the distribution of C18 droplets on the glass surface did not improve.

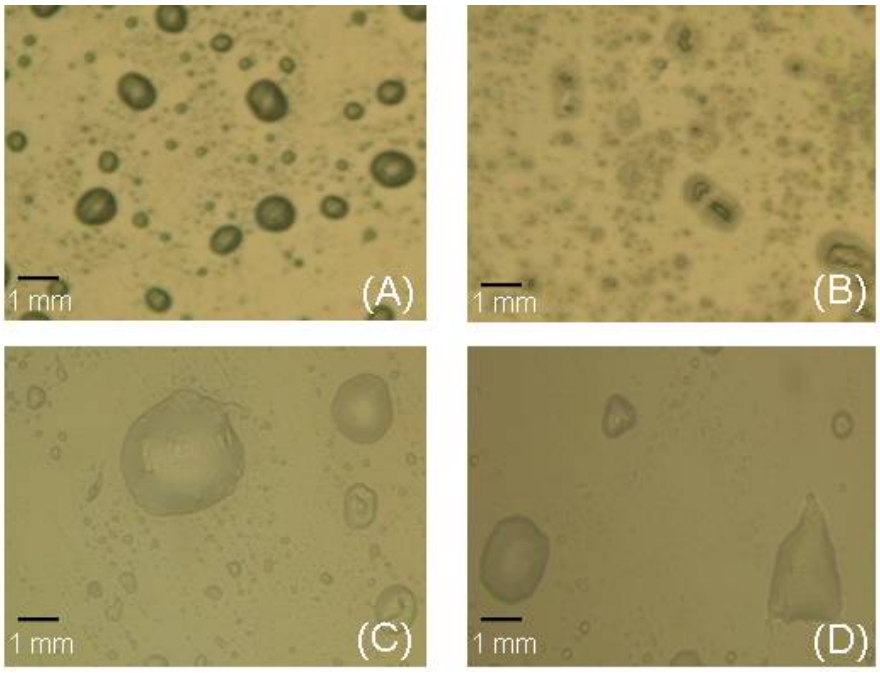

Figure 4.3: Photos of glass surface after the spin coating process with 1 mL C18 solution. (A) The central part and (B) the border part of the glass surface have dark "islands" due to the accumulation of C18 droplets. After heated up to remove the toluene solvent, (C) the solid parts on the surface still exist. If (D) more C18 up to 2 mL is added, the inhomogeneity does not improve.

Vapor Deposition

To overcome the accumulation of C18 droplets that occurred in the spin coating process, vapor deposition method was introduced to generate dense and homogeneous C18 vapor instead of droplets. The vapor sprayed at the same time on the whole pretreated glass surface. C18 solution was kept in a small chamber together with target glass plate during the deposition process. Since C18 has long chain length and high boiling point, they were heated up to 60^{o} C for 30 min.

After the vapor deposition, no accumulation was seen on the glass surface. The surface properties are checked in section 4.1.3.

Immersion

In parallel, immersion method was introduced to solve the inhomogeneous "island" problem. The pretreated glass plate was submersed into C18 solution and kept at 30^{o} C for at least 24 hours, then rinsed with toluene and distilled water. The surface properties are also checked in section 4.1.3.

4.1.3 Characterization of Glass Surface Properties

Some of the basic properties of a stationary phase are the stability against dissolving in the mobile phase and a certain surface homogeneity. Hence, contact angle measurements and white light interferometry (WLI) were chosen to characterize these surface properties.

Contact Angle Measurement

Contact angle reflects whether the surface property is hydrophobic or hydrophilic. In our measurement, static tangent method was used to acquire the contact angles.

To check the stability of stationary phase against the mobile phase, C18 coated glass plates were submersed in mobile phase solution for 24 h. Then the contact angles were measured and compared with the contact angles on fresh-made glass surface. The details are illustrated in section B1.

From the comparison of contact angle changes summarized in figure 4.4, the immersion method is superior. The glass surface freshly silanized with C18 has a mean contact angle of 113°, and the angle is reduced only from 116° to 110° after immersion in mobile phase, indicating its coating stability against the mobile phase. However, with the vapor deposition method, the contact angle decreases tremendously from 100° to 55°, which indicates that only temporary physical attachment of C18 instead of chemical bonding is formed in the vapor deposition process.

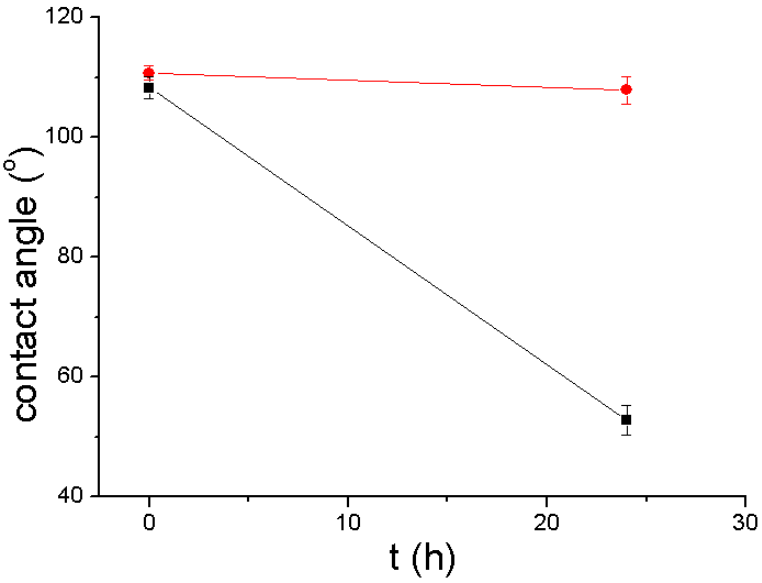

Figure 4.4: Contact angle changes versus time. (■) vapor deposition method shows inferior performance with poor stability and (●) immersion method has better stability when the glass plate is immersed in the mobile phase for 24h.

White Light Interferometry

WLI measurements were accomplished by the equipment ZYGO New View 5000 System (ZYGO Corporation, USA)[1]. To obtain precise height measurements with large steps or rough surfaces, a method called vertical scanning or coherence probe interferometer was used. Equipped with a white light source, this method employed the coherence peak sensing approach.

All 2D and 3D images shown in figure 4.5 and figure 4.6 illustrate the topographic maps of the test glass surfaces with the coherence intensity images. The colors represent heights. The black parts in these images represent the area with unknown optical property. The unknown property may be due to either too low or too high topography. Another possible reason is that these parts are covered with the material, which has too much absorption of the white light and too low reflection to give any height information in WLI measurements.

[1] http://zygo.com/

In figure 4.5, the surface roughness with immersion and vapor deposition methods are compared. Immersion method gives better homogeneity and thicker C18 coating. The average roughness (X_{RMS}) of the C18 layer coated on glass surface is about 300 nm with the immersion method and about 30 nm with the vapor deposition method.

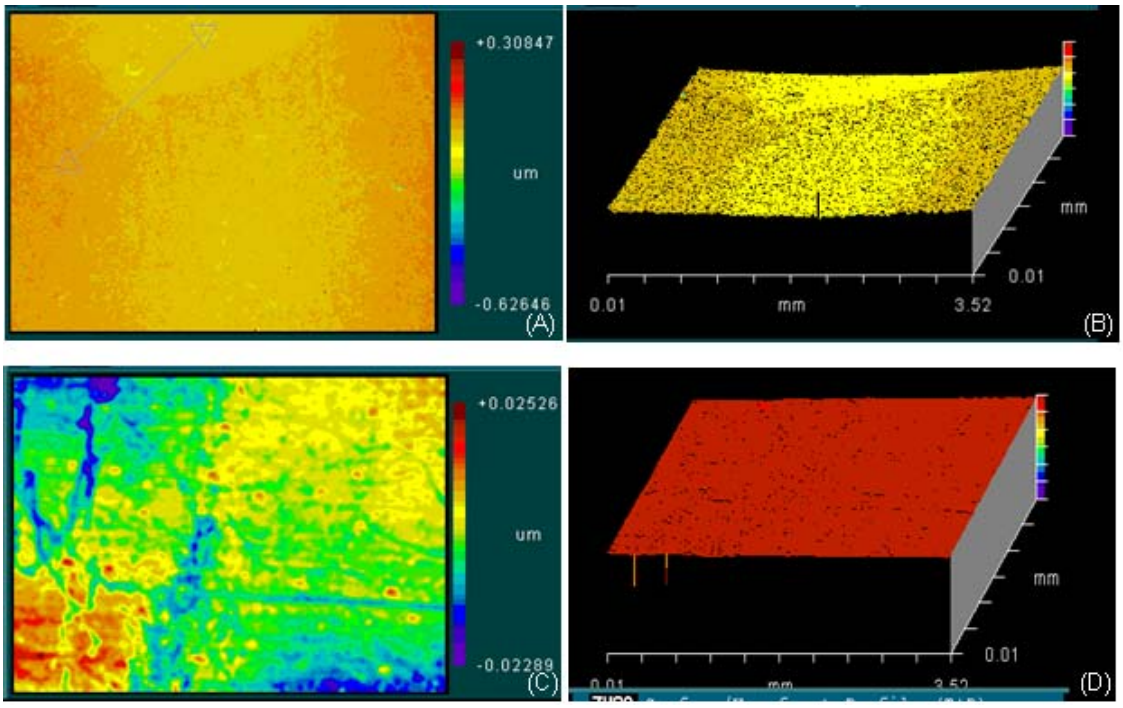

Figure 4.5: Surface topographic images of C18 coated glass surfaces with height information measured by WLI. (A) and (B) are surfaces treated with immersion method; (C) and (D) are treated with vapor deposition method. Measured area is 0.01 mm × 0.01 mm. The immersion method has better homogeneity and thicker C18 coating.

In parallel, different pretreatment methods are compared in figure 4.6 with the same silanization method (immersion). To carry out thickness measurement, half of the glass surface was wrapped by a plastic stripe immediately after pretreatment. After silanization with immersion method, the plastic stripe was taken off and the cross section over coated and uncoated surface was measured by WLI. Through analyzing the depth of the cross section from the images in figure 4.6, plasma cleaner

gives the weakest coating process with an average thickness of 500 nm. The piranha solution is a stronger oxidant with a thicker C18 layer of about 900 nm. HF solution is corrosive to glass, so that the C18 layers are the thickest, which have an average thickness of 1200 nm with the roughness of 500 nm.

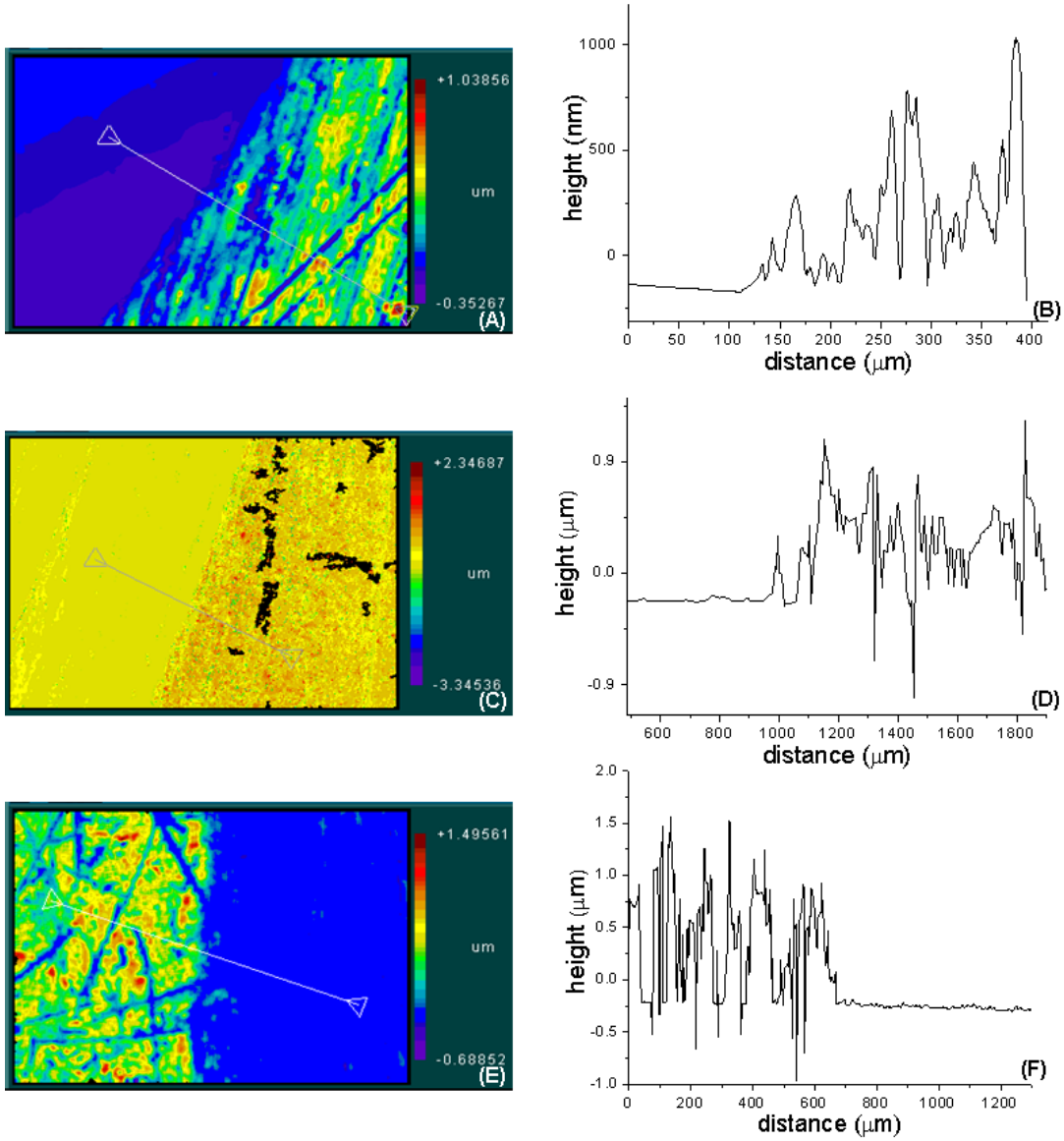

Figure 4.6: Topographic maps and the height profiles of the test glass surfaces. The height profiles calculated in (B), (D), and (F) are done by Origin 7.0 according to the topographic maps on the left side. The glass surfaces pretreated with (A) plasma cleaner, (C) piranha solution, and (E) 2% HF solution are compared. HF pretreatment has thicker C18 coating and better roughness.

The different thickness of C18 layers with different pretreatment methods is due to the different roughness on the uncoated glass plates. Hence the uncoated glass surface properties are checked by WLI (figure 4.7). Over the same distance of 100 μm, the HF solution pretreatment offers the roughest surface (about 60 nm) and plasma cleaner pretreatment gives smoothest surface (about 30 nm). The roughened surfaces provided more silanization sites and therefore the coated layers had better roughness.

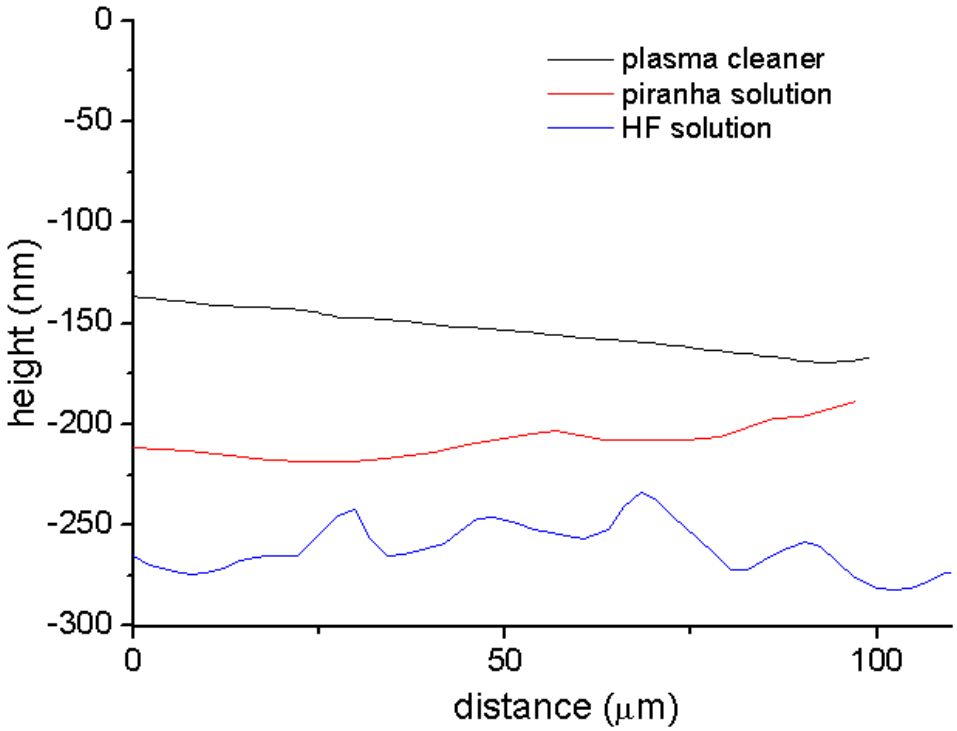

Figure 4.7: Height profiles of the bare glass surfaces pretreated by plasma cleaner, piranha solution, and HF solution. The glass surface pretreated with HF has roughest surface profile, which provides more active sites for silanization step.

Meanwhile, other method for stationary phase coating was tried as well.

4.1.4 Magnetic Powders

One way to improve the coating of stationary phase is using the magnetic nano-powders as the holding media for C18 layer. The magnetic nano-powders are easy to

handle because of their fluidic property and stable surface coating. The fluidic property makes them easy to be shaped by a magnet with various requirements.

Coating Process:

The coating process for magnetic powders is the same as for ferrofluids[80]. 0.5 g magnetic particles (Iron oxide nanopowder, < 50 nm, Sigma-Aldrich Chemie GmbH, Germany) were dissolved in methanol and dispersed in C18 toluene solution, and stirred for 12 h at 30 ºC. Then the particles were rinsed by toluene and dried with nitrogen. The coating property was checked with infrared spectrometry (IR).

The IR experiment was done by PERKIN ELMER System 2000 IR spectrometry with Nd YAG Laser. The scanning wave numbers were from 4000 cm^{-1} to 500 cm^{-1}. Sample powders were mixed with KBr and pressed with a homemade mechanical pump into a tablet for IR measurement.

The IR spectra are shown in figure 4.8. The effective chemical bond is Fe-O-Si bond. From the comparison before (figure 4.8 (A)) and after (figure 4.8 (B)) the coating process, water components in magnetic powders stay the same with the constant absorbance intensity at about 3500 cm^{-1}. The peak at about 1200 cm^{-1} increases after the coating process due to the formation of Si-O bonds. Before the coating process, the spectrum at about 1200 cm^{-1} comes from the minor C-O bonds contained in the air (CO_2), which have a peak at the same position with Si-O bonds. The new peaks in figure 4.8 (B) between 2850 cm^{-1} and 3000 cm^{-1} represent that Fe-O-Si bond was formed during the coating process. IR spectra identified the successful bonding of C18 stationary phase and the magnetic powders.

After the stationary phase was coated on the magnetic powders, rotation movement was applied to check the location property of the new stationary media.

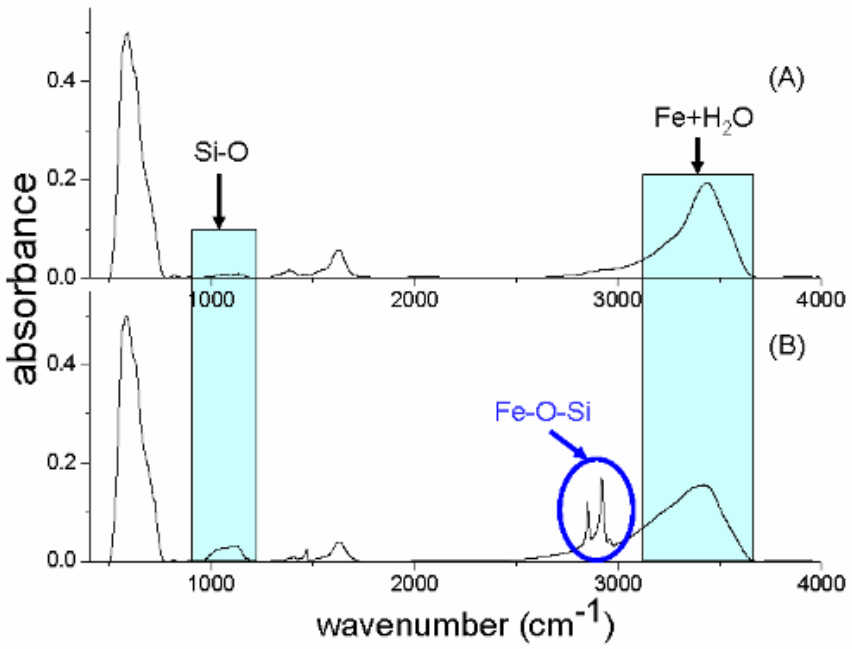

Figure 4.8: IR spectra of magnetic powders (A) before and (B) after coated with C18. The absorbance peaks between 2850 cm^{-1} and 3000 cm^{-1} represent the formed Fe-O bonds.

Experiments and Characterization:

In order to check the location stability of the magnetic powders in the rotation procedure, the experiment design is illustrated in figure 4.9 to observe the behaviors of the magnetic powders.

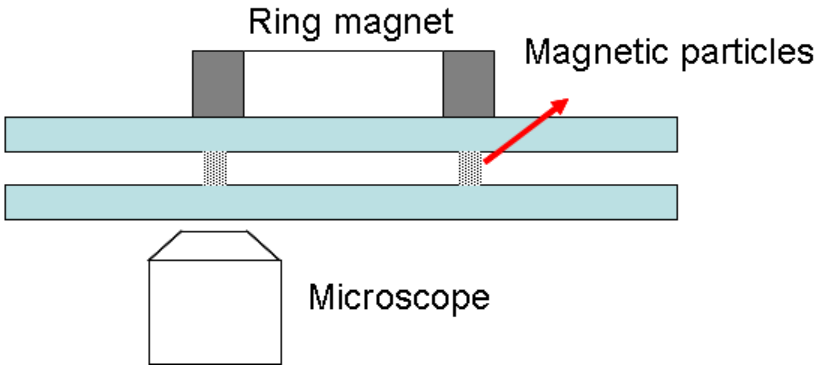

Figure 4.9: Illustration of the rotation experiment when C18 is coated on the magnetic powders.

Before rotation, the particles were sprayed with the pipette evenly in a round area as shown in figure 4.10 (A), according to the size of the ring permanent magnet (N 38, OD 40 × ID 36 × 7 mm, Nickel, ChenYang Technologies GmbH & Co. KG). The ring magnet was laid on top of the rotation glass plate. The mobile phase was perfused around the circle. The final track was determined by the ring magnet during rotation experiment because of the flowing freedom of the magnetic powders.

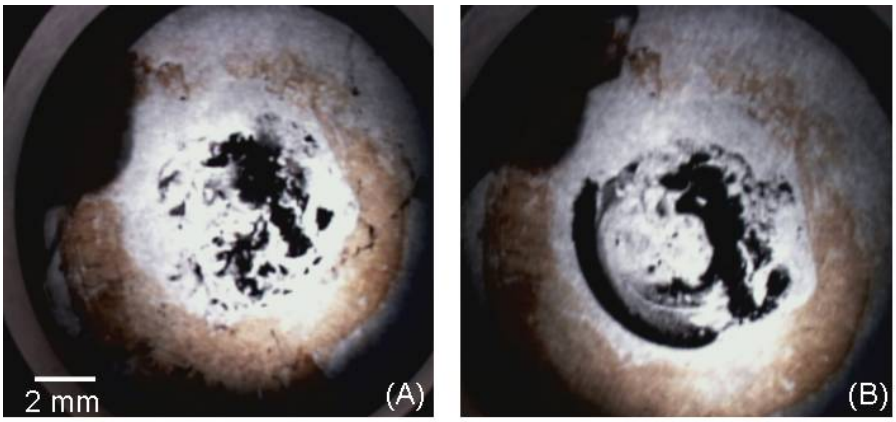

Figure 4.10: Magnetic powder (A) before and (B) after rotation experiment. The circular track is formed by the ring magnet. The uneven distribution of magnetic powders indicates that the magnetic power is weakened by the thickness of the glass plate and is not suitable for SDCC.

Since the strength of magnetic field produced by the magnet decreases with the inverse third or fifth power of distance[1], the thickness of glass plate (~ 1 mm) weakens the magnetic power enormously. Another factor affecting the strength of magnetic field is the aggregation of fine powders. The magnetic powders accumulated during rotation to form "islands" on the glass plate. This made the magnetic powder much weaker on the top of the "islands" than the bottom. Therefore, the magnetic field was uneven through the circular track, and the magnetic powders were located unevenly as shown in figure 4.10 (B). When the thickness of the

[1] http://en.wikipedia.org/wiki/Magnetic_moment

powders was bigger than that of the liquid film, the rotation was hindered. This would lead to the turbulence in mobile phase.

After the investigations on different stationary phase coating methods, pretreatment with HF solution and silanized with immersion method afterwards was chosen for the following SDCC experiments.

4.2 Validation of Channel-free Shear Driven Circular Chromatography

Today's dominant separation methods such as HPLC and CE are both limited by resistive behaviors discussed in section 2.3. For example, the fast pressure driven flows in small columns with long paths are districted by Poiseuille's law of extreme and impractical pressure limitation; on the other hand, band broadening attributed to the temperature change through the column is also dependent on the flow velocity[81]. Then shear driven chromatography was developed to overcome these limitations with the help of liquid viscosity in micro-channels. When SDC is to be realized, the channel-free system has more potential compared with micro-channels in separation efficiency enhancement. Nanostructure fabrication on stationary phase with monolithic silica layer has the same function with "channel-free" method. Recently, the nanostructure fabrication was reported to give faster separations, better resolution and lower limits of detection[82] in LC. The nanostructure has the dimension in the range of 10 μm.

The channel-free separation method is inspired by thin layer chromatography (TLC) and ultrathin layer chromatography (UTLC) systems which have only flat stationary phase layer instead of channels. In order to validate SDCC, the experimental arrangement B described in figure 3.4 in section 3.1.2 was chosen to investigate circular liquid chromatography in the following experiments.

4.2.1 Separation of Rhodamine B and Fluorescein Mixture

The experimental operation is illustrated in figure 4.11. No micro-channel is fabricated and only shear force is applied.

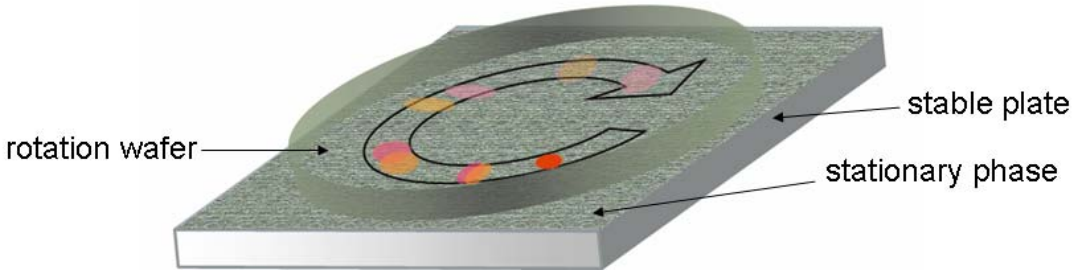

Figure 4.11: Illustration of the channel-free SDCC process. Analytes are sandwiched between the cover glass plate (rotated by the rotor) and bottom glass plate (coated with C18). The analytes are separated in a circular track with the cycles.

The analytes chosen in our experiment were rhodamine B with the excitation wavelength (Ex) at 530 nm and emission wavelength (Em) at 566 nm (Merck, Germany), and fluorescein sodium salt with Ex at 490 nm and Em at 520 nm (Merck, Germany). The molecular structures are shown in figure 4.12. Their fluorescent wavelengths fit the filter range of our microscope and their polarities are much different.

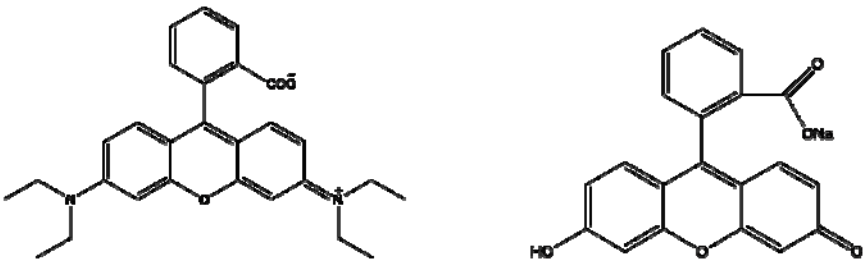

Figure 4.12: Molecular structure of rhodamine B and fluorescein sodium salt.

The sample was prepared with 5 mM rhodamine B and 5 mM fluorescein mixtures in methanol (Merck, Germany) solution.

Experiment:

A small aliquot of the sample solution was injected manually onto the C18 coated glass plate laid beneath. Then the mobile phase was perfused around the sample droplet on the bottom glass plate and covered with the uncoated glass plate, taking care to avoid the formation of air pockets. The rotation motor was laid immediately on top to fix the upper glass plate with a homemade metal frame. This step was carried out as fast as possible with practice to eliminate the analytes diffusion into the mobile phase before rotation. When the rotation started, the fluorescence intensities were collected by PMT or CCD camera.

For preliminary investigation, rhodamine B and fluorescein were tried on TLC plates to check the retention factor and separation capability. With HPTLC plates silica gel 60 F254 plates, which were precoated for nano-TLC (Merck, Darmstadt, Germany), rhodamine B and fluorescein were successfully separated as shown in figure 4.13. According to the chosen stationary phase, mobile phase with low reactivity and high retention factor was chosen. In our experiment, the mobile phase was 30% (v/v) water in methanol (Merck, Germany) solution.

The separation occurred in the radius direction rather than in the fluid flow direction. This phenomenon indicated that the flow of the fluorescent dyes was dominated by primary diffusion effects in the silica gel layer.

The separation took place only in the direction of mobile phase diffusion within the porous micro-structures of the stationary phase, but not in the direction of rotation. The porous silica gel layer with the pore size of about 60 Å[1] has hampered the diffusion of samples from silica gel to mobile phase. The main part of the samples was trapped in the pores and flowed from pore to pore with the diffusion of the

[1] http://www.voigtglobal.com/EM_Merck_TLC_Plates.htm

mobile phase. Shear driven flow had minor effects on the separation process. Hence, the commercial silica gel plate was not suitable to carry out SDCC because of its surface properties.

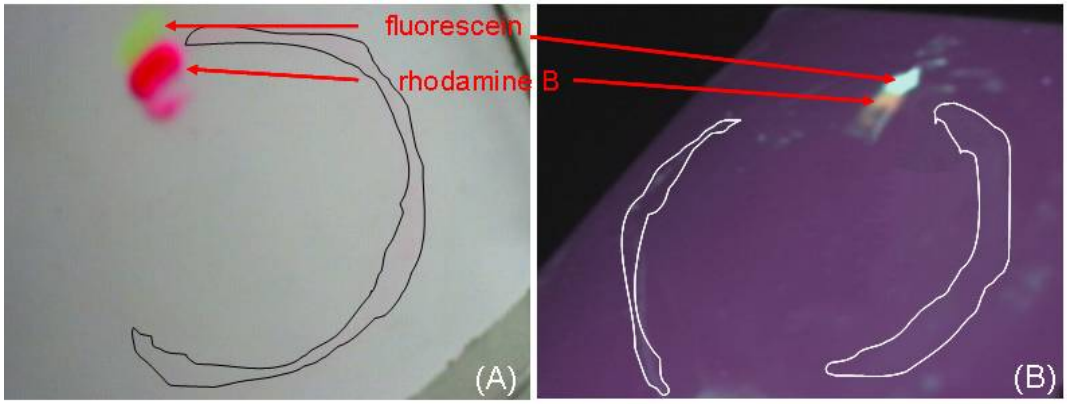

Figure 4.13: Rhodamine B and fluorescein separated by TLC silica gel plates with 70:30 (v/v) methanol in 1-octanol solution. Fluorescein has lower polarity and flows faster than rhodamine B. The two fluorophores separate in the diffusion direction other than shear flow direction. The flow trajectory of the dyes has been outlined.

Mobile Phases

30% (v/v) water in methanol solution was used as mobile phase because of its superior performance in TLC compared with other combinations as shown in figure 4.14. 1-octanol, ethyl acetate and n-hexane solvent are all from Sigma Aldrich Chemie GmbH, Germany. The retention factors R_f defined by equation 4.1 are described in table 4.1. Bigger R_f reflects better separation performance. In equation 4.1, $S_{compound}$ *(cm)* and $S_{solvent}$ *(cm)* are the distances travelled by the compound and solvent front.

$$R_f = \frac{S_{compound}}{S_{solvent}} \quad (4.1)$$

The mobile phase 15:35:50 water, methanol and ethyl acetate (row D in table 4.1) is not chosen even though it shows better separation performance than 30:70 water

and methanol solution (row A intable 4.1). This is because fluorescein flows as far as mobile phase, and the retention factor is 1. The stationary phase has no influence on the analytes. In the chromatogram, the signal peaks of mobile phase and fluorescein will overlap, and the peak shape of fluorescein is too poor to calculate theoretical plate numbers and the other chromatographic parameters.

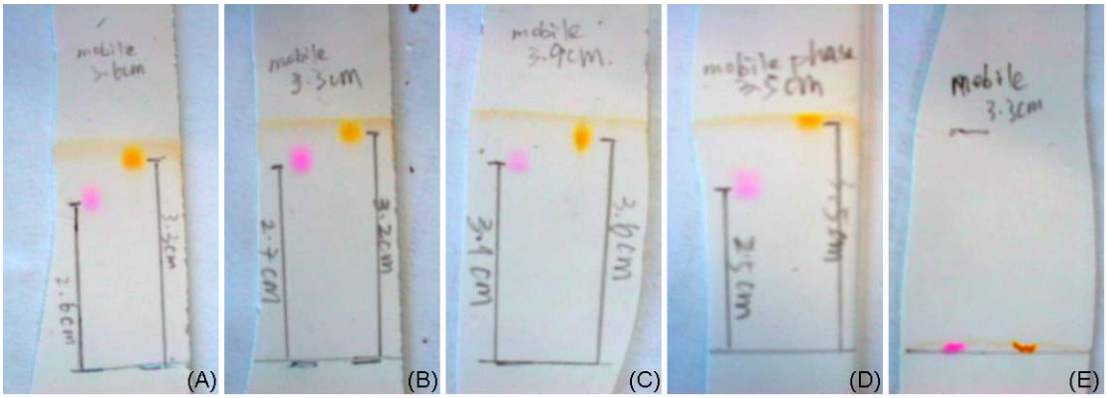

Figure 4.14: TLC performance with different mobile phases. (A) 30:70 (v/v) water and methanol, (B) 25:65:10 (v/v/v) water, methanol and octanol, (C) 15:85 water and methanol, (D) 15:35:50 water, methanol and ethyl acetate, and (E) 15:35:50 water, methanol and n-hexane are used. The analyte is 5 mM rhodamine B and 5 mM fluorescein mixture in methanol.

Table 4.1: Retention factors R_f in TLC for different mobile phases. Mixture A is used in the following experiment because of its resonable retention factor R_f for fluorescein and better retention factor difference of the two fluorophores.

mobile phases	$S_{compound}$ for rhodamine B (cm)	$S_{compound}$ for fluorescein (cm)	$S_{solvent}$ (cm)	R_f for rhodamine B	R_f for fluorescein	R_f difference
A	2.6	3.3	3.6	0.72	0.92	0.2
B	2.7	3.2	3.3	0.84	0.97	0.13
C	3.1	3.6	3.9	0.79	0.92	0.13
D	2.5	3.5	3.5	0.71	1	0.29
E	0	0	3.3	/	/	/

A: 30:70 (v/v) water and methanol,
B: 25:65:10 (v/v/v) water, methanol and octanol,
C: 15:85 water and methanol,
D: 15:35:50 water, methanol and ethyl acetate,
E: 15:35:50 water, methanol and n-hexane

SDCC

In SDCC experiment, the glass plates were prepared by HF pretreatment and immersion silanization as discussed in section 4.1.2, and 30% (v/v) water in methanol solution was used as mobile phase. Because the stationary phase had a thickness of about 1200 nm and the roughness was about 500 nm, compared with mobile phase film with the thickness of 20 μm thick, the fluorescent dyes were mainly carried by mobile phase and the signals were recorded by PMT whilst the motor rotating.

The temperature stays steady because SDCC is an open system. Other parameters such as mobile phase flow velocity and sample concentration affect the separation performance of the SDCC system. In order to optimize separation, all the variables have to be calibrated.

Velocity of moving wall u_{wall} *(m/s)* was controlled by the rotation frequency, which was defined as $u_{wall} = 2\pi rf$. In our experiment, r was a constant (9 mm) because of the fixed bottom stationary stage with a fixed microscope objective pinhole. The sample was injected according to the objective position, which is 9 mm away from the center. The linear velocity profile of shear driven flow produced a mean mobile phase velocity, which is half of the moving wall velocity ($\bar{u} = u_{wall}/2$), which was proved in previous work[50].

For setup B, the rotation frequency of step motor was controlled by a self-developed PICO program written and explained in section B.2.

Frequency f was then a controllable and key factor in SDCC. Two extreme cases are shown in figure 4.15, either with too low (0.045 Hz) frequency or with too high (0.45 Hz) frequency. With the low frequency (figure 4.15 (A)) the sample already dispersed into the surrounding mobile phase, and the signals went extinct before the separation occurred. Because our system was channel-free and the samples were restricted in a circular track temporarily only depending on the short-term diffusion balance between sample and mobile phase. After the short balance, the samples dispersed and the concentration decreased. The shear force also reinforced the dispersion effect and speeded up the attenuation. On the other hand, if the frequency f

was too high (figure 4.15 (B)), the sample was carried mainly in mobile phase and had not enough time to fully exchange with stationary phase. The exchange was limited, and the function of stationary phase was weakened. Thus the separation efficiency was low. It was proven that equilibrium was impossible to establish with too high frequency. This led to a circular track full of fluorescent dyes, which was indicated in PMT record as poor resolution peaks or even no peaks but plateau. Even if the separation occurred, the frontier portion would travel too fast and meet the tail portion to remix again. In figure 4.15 (B), the peaks appeared in good shape for the first several cycles but became broadened with time and changed into a plateau at last. Hence, it was impossible to detect the separation with either too low or too high rotation frequency.

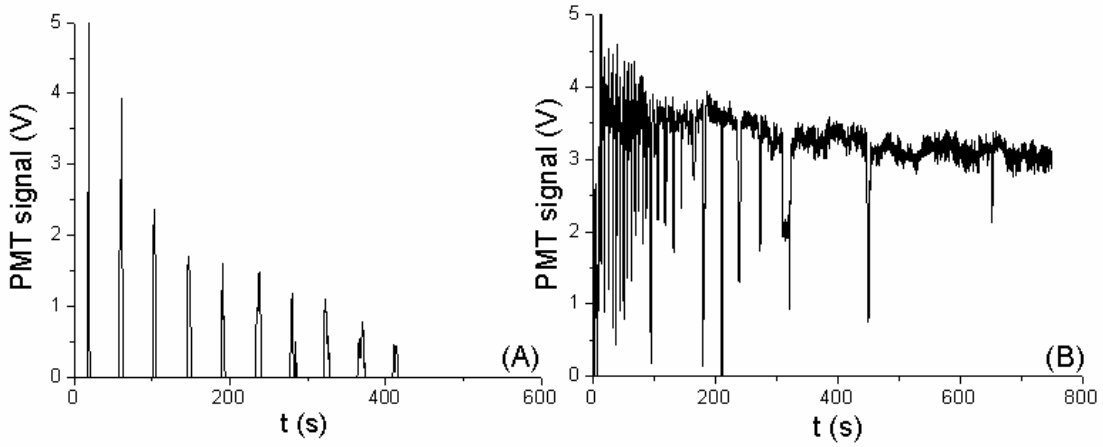

Figure 4.15: PMT signals of improper frequencies for rhodamine B and fluorescein mixtures in SDCC. (A) 0.045 Hz is too low as the signal disappears after 10 cycles and (B) 0.45 Hz is too high as the signal reaches a plateau after 400 s. In both cases, no chromatography separation can be detected.

The highest separation resolution was obtained with a rotation frequency f of 0.114 Hz. This frequency provided a moving wall velocity of 6.44 mm/s with r = 9 mm, and a mean mobile phase velocity of 3.22 mm/s.

Another crucial factor in SDCC is the sample concentration, which is determined by the amount of sample injected and the volume of mobile phase applied. Improper

concentrations illustrated in figure 4.16 lead to poor resolutions in chromatographic separations. With too low concentration shown in figure 4.16 (A), the S/N ratio of the PMT signal was low, which made the separation peaks hard to identify. Too high concentration in figure 4.16 (B) induces saturated intensity on PMT recorder from the first cycle and the plateau becomes broader after several cycles.

Based on experimental results, the concentration factor was quantified by applying 0.1 μL sample solutions with syringe and 6 drops of mobile phase solution with plastic pipette (2 mm in diameter). The reproducibility was improved with experience.

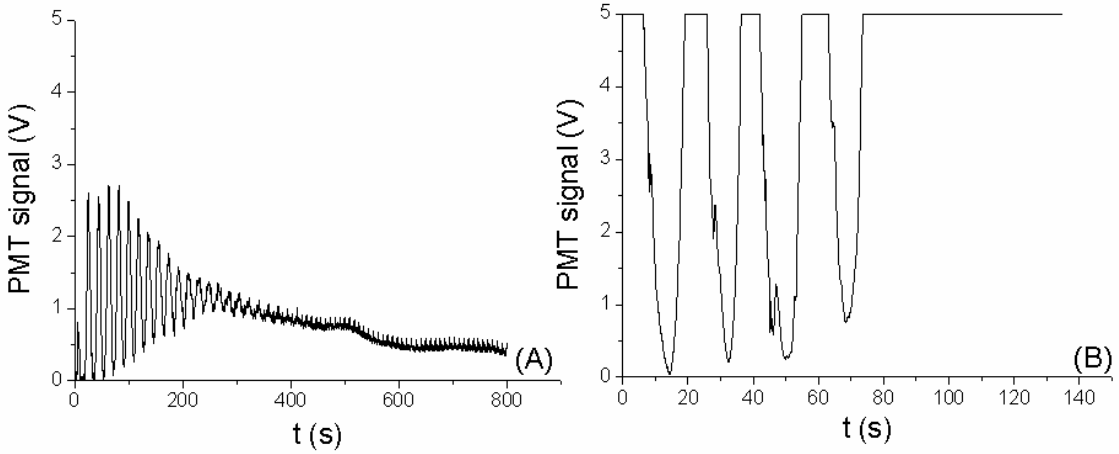

Figure 4.16: PMT signals of improper concentrations for rhodamine B and fluorescein mixtures in SDCC. (A) Too low concentration causes low S/N ratio and (B) too high concentration leads to overloaded detection. Both conditions have poor resolutions. The frequency is 0.114 Hz.

With optimized rotation frequency (f = 0.114 Hz) and sample concentration, rhodamine B and fluorescein mixture was successfully separated. The result is plotted as intensity versus time in figure 4.17 (A). The first peak is a single peak with no separation yet. From the second cycle the peak begins to split into two peaks and the overlap of these two peaks become smaller following the cycles. In these separated two peak groups, the faster peaks with higher intensity indicate rhodamine B and the fluorescein peaks have lower intensity. That is because rhodamine B has higher

polarity and less affinity to the stationary phase, so it has shorter retention time. The decreasing intensity of the signals is mainly attributed to dispersion into mobile phase and partly to photo-bleaching of the fluorescent dye molecules. Growth of the time interval between the two peaks following each rotation cycle represents the increasing separation efficiency. In order to distinguish rhodamine B and fluorescein peaks, Gaussian simulation is applied (figure 4.17 (B)) for further studies. Although the reproducibility needs to be enhanced, SDCC method has successfully separated the samples in this channel-free system.

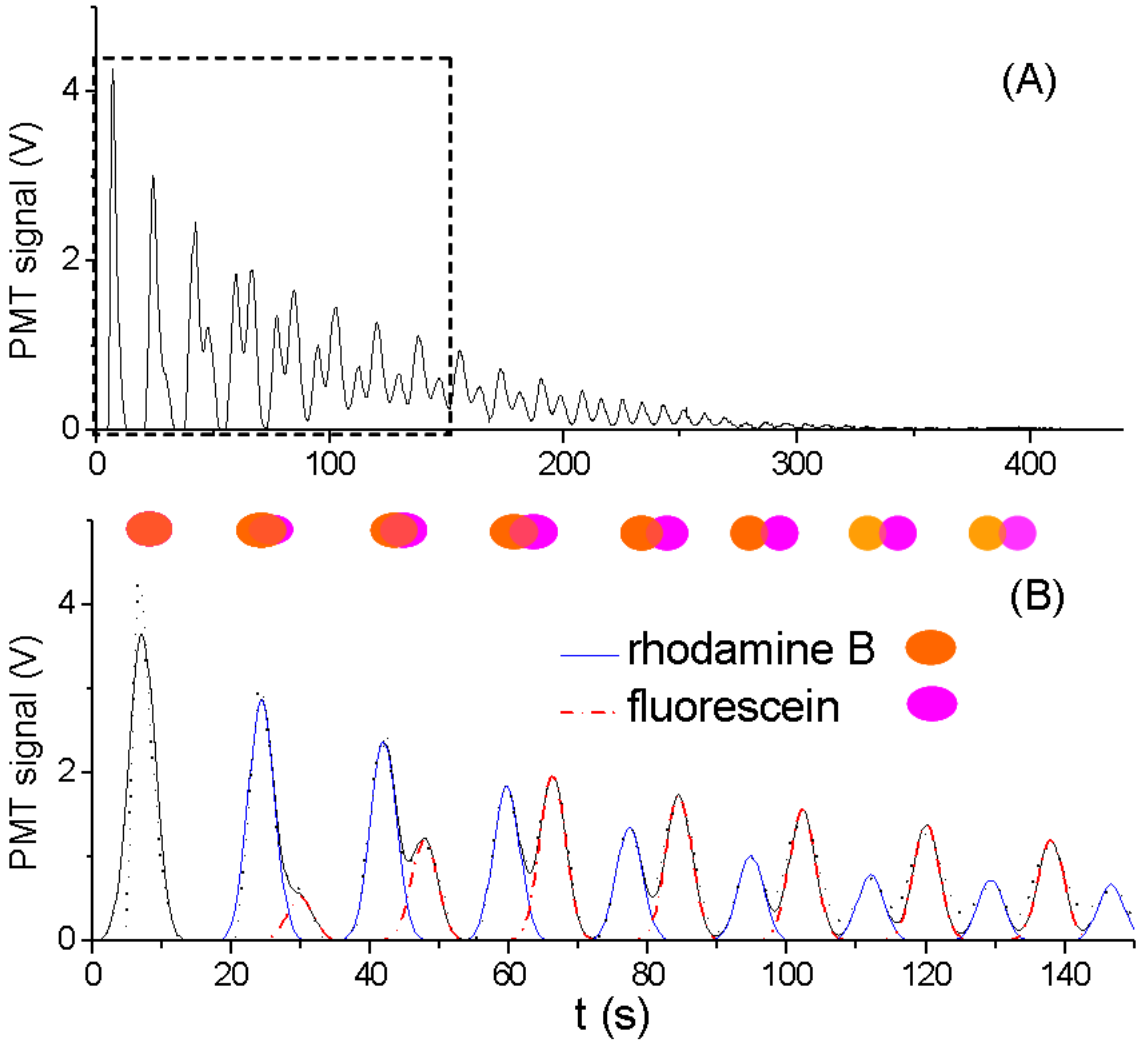

Figure 4.17: Fluorescence intensities of (A) experimental peaks by PMT, and (B) simulated peaks with Gaussian simulation by PeakFit v4. rhodamine B has shorter retention time because it has lower polarity and stronger affinity to the C18.

As shown in figure 4.17 (A), the height of rhodamine B peaks decrease with time due to dispersion, but the height of fluorescein peaks firstly increase and then decrease. The abnormal intensity change is due to the resonance energy transfer (RET)[83] effect, which is explained by figure 4.18.

4.2.2 Resonance Energy Transfer

RET is referred to fluorescence resonance energy transfer (FRET), which can happen when the emission wavelength of one fluorophore overlaps excitation wavelength of another fluorophore. The emission fluorophore is called donor and the other one is called acceptor, which work as a pair in RET process. RET extent depends on the concentration ratio of the acceptor and the donor, the overlap extent of the emission spectrum of donor with the absorption spectrum of acceptor, the orientation of donor and acceptor dipoles, and the distance between donor and acceptor molecules.

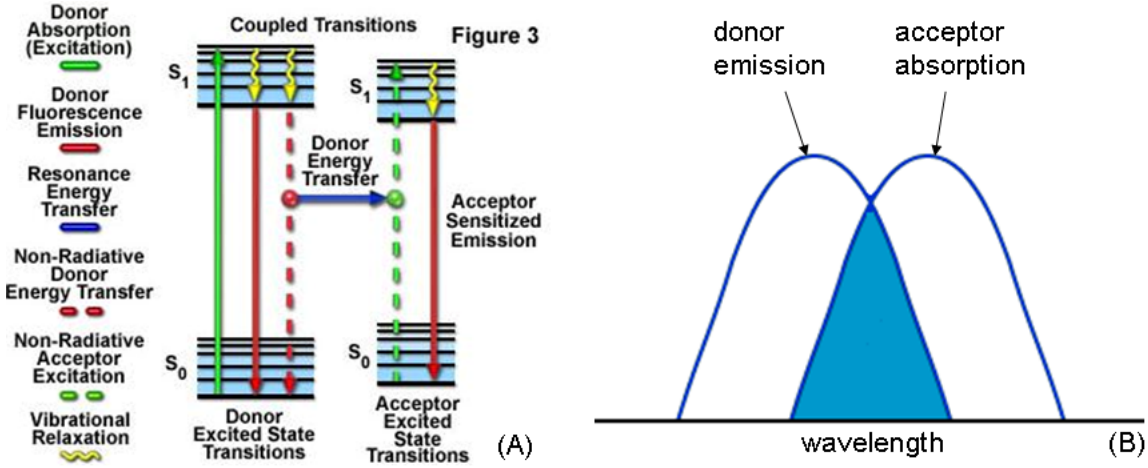

Figure 4.18: Theoretical explanation of RET. (A) the Jablonski diagram[1] and (B) schematic spectrum overlap[2] representation of the coupled transit between the donor emission and acceptor absorption.

[1] http://www.olympusconfocal.com/applications/fretintro.html
[2] http://www.bio.davidson.edu/courses/Molbio/MolStudents/spring2000/deeb/method.html

The RET effect decays with the increasing distance between donor and acceptor. From a certain critical distance, the RET decay rate is faster than the transfer rate and the RET is not efficient anymore. This critical distance is named as Förster distance[84]. So the most important use of RET is to determine the distance of two sites on a macromolecule like protein or DNA, which has pairs of function groups with energy transit. To be an acceptor, the component is not necessarily fluorescent. As the figure 4.18 (A) shows, there is even no photon transit process.

In our experiment, fluorescein was assumed to be quenched by rhodamine B in the first several cycles because of RET (figure 4.18 (B)). Further experiments were designed to prove the assumption.

Experiment:

In the first set of experiment, 0.5 mM rhodamine B and 0.5 mM fluorescein sodium salt in methanol solution were measured separately, and their mixture with the ratio of 1:1 was measured.

As the second set of experiment, 0.5 mM rhodamine B and 0.5 mM fluorescein sodium salt mixture solutions with different ratios of 1:2, 1:5, and 1:10 in methanol were measured.

Fluorescence spectroscopy was done by SPEX FluoroMax spectrometer. The xenon lamp has emission wavelength of 467 nm and excitation wavelength of 480 nm. The scanning range was from 400 nm to 800 nm, with increment wavelength of 0.5 nm and integration time of 0.2 s. The split of the monochromator was 1 nm.

The fluorescence spectra for the first group are shown in figure 4.19. 0.5 mM fluorescein in methanol has the emission wavelength at 516 nm (figure 4.19 (C)). The absorption wavelength of rhodamine B is at 530 nm, and the emission wavelength of fluorescein is in the range of rhodamine B absorption. Hence, the fluorescein works as a donor and the emission energy is absorbed by rhodamine B as an acceptor to excite its own emission. This proves the existence of RET and explains the

observation in figure 4.19 (D) that the mixture has only one emission fluorescence wavelength at about 580 nm, when compared with figure 4.19 (B), where 0.5 mM rhodamine B in methanol solution has the emission wavelength at 580 nm.

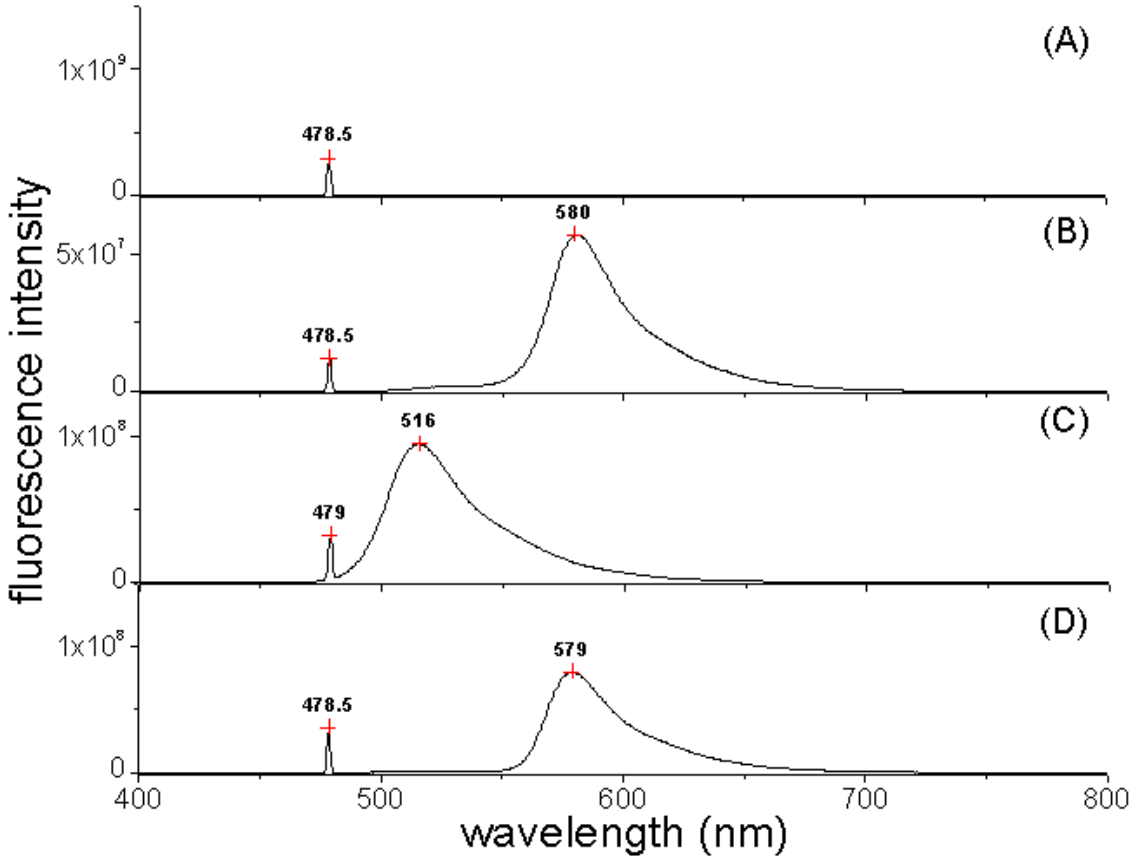

Figure 4.19: Fluorescence spectra of (A) pure methanol, (B) 0.5 mM rhodamine B in methanol, (C) 0.5 mM fluorescein in methanol, and (D) 0.5 mM rhodamine B and 0.5 mM fluorescein mixture in methanol. Peak at about 479 nm is from xenon lamp emission. In the mixture solution (D), fluorescein is quenched by rhodamine B.

In the second group, rhodamine B and fluorescein mixture solution with different concentration ratios are compared in figure 4.20. The concentration ratios of rhodamine B to fluorescein change from 1:2 to 1:10. When the ratio is 1:2, the fluorescence intensity of fluorescein is quenched by rhodamine B shown in figure 4.20 (A). When the ratio is 1:5, the fluorescein emission peak appears at 512 nm as a

convex shoulder shown in figure 4.20 (B). The small shoulder grows with the increasing concentration of fluorescein, because the emitting energy offered by fluorescein molecules fulfills the rhodamine B absorption demand and provides redundant energy for fluorescein emission. With the increasing amount of fluorescein molecules, more energy is provided by the donor fluorophore. Hence, when the concentration ratio is 1:10, the intensity of fluorescein emission peak at 512 nm and the one of rhodamine B at around 570 nm are comparable (figure 4.20 (C)).

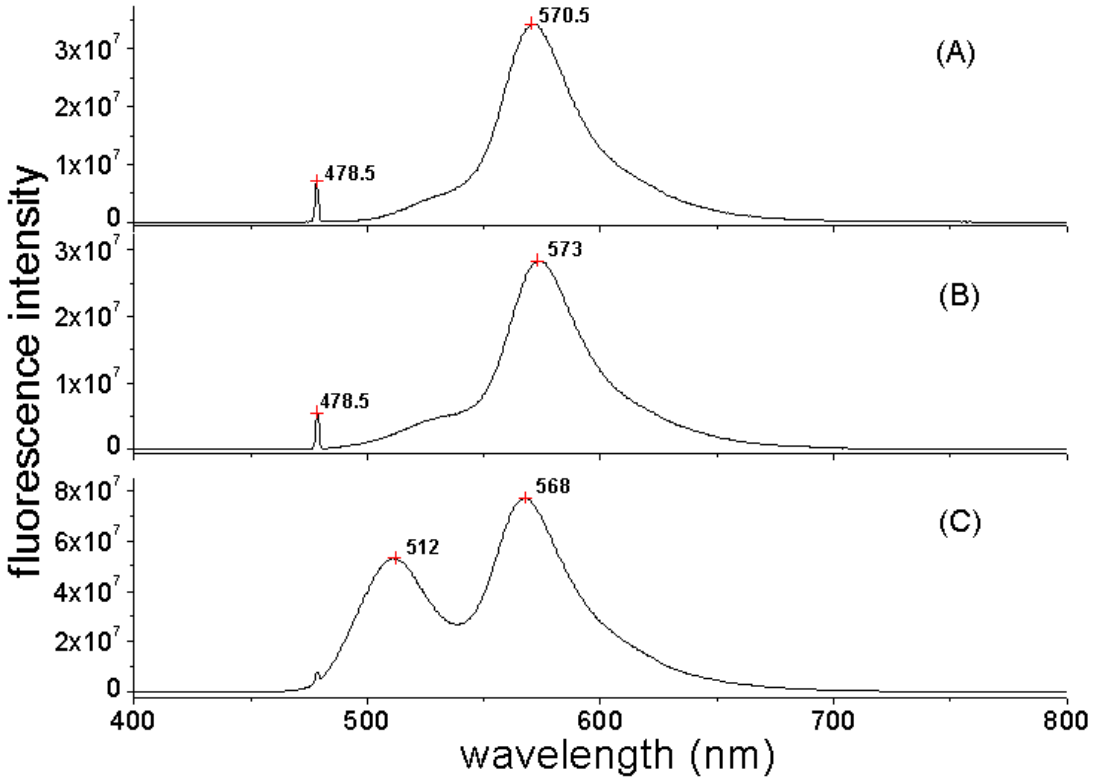

Figure 4.20: Fluorescence spectra of different concentration ratios of rhodamine B to fluorescein mixture in methanol with (A) 1:2, (B) 1:5, and (C) 1:10. Peak at about 479 nm is from xenon lamp emission. The fluorescence spectrum of fluorescein at first (A) is quenched by rhodamine B and ((B) and (C)) then grows with the increasing concentration of fluorescein.

With these investigations, the phenomena observed in figure 4.17 can be explained with RET effect. For the sample solution with 1:1 (c/c) rhodamine B and

fluorescein, the fluorescein signal was completely quenched by rhodamine B. The fluorescein signal could only be detected after being separated from rhodamine B. With more fluorescein separated from rhodamine B, the fluorescence intensity increased because of weaker RET effect.

However, the fluorescein molecules disperse into the mobile phase as well as rhodamine B molecules, therefore the intensity for both dyes decrease with time. With the separated peaks in the chromatogram, their chromatographic performance can be analyzed.

4.2.3 Chromatographic Analysis

Theoretical plate numbers *N* and height equivalent to a theoretical plate (HETP) *H* are the most important parameters to evaluate the chromatographic separation efficiency. In section 2.3.1, *N* was defined by equation 2.4 in general chromatographic method, which indicated the equilibrium steps derived from chemical engineering concept. Therefore *N* was calculated from the chromatogram. In our experiment, HETP is defined by equation 4.2, where *i* is the cycle number, *r* is 9 mm.

$$H_i = \frac{2 \cdot \pi \cdot r \cdot i}{N_i} \quad (4.2)$$

The rhodamine B and fluorescein peaks are simulated and sorted into two separate groups as shown in figure 4.21. Since the peaks are simulated with Gaussian function and normalized with the same peak width w_b *(s)*, *N* and *H* are calculated and listed in section B.3 for both fluorophores. The peaks after 15 cycles still contribute to *H* and *N* calculations, albeit the intensity is already too low to be seen in figure 4.21.

Increasing *N* and decreasing *H* both lead to increasing separation efficiency. The trends are plotted in figure 4.22 against cycles. The decreasing rate of *H* slows down after several cycles. *N* increases with number of cycles linearly. For fluorescein, theoretical plate numbers *N* increase with the rotation cycles from 102 to more than 1000 during the whole separation process. *N* increases to 295 in the fifth cycle, where

the two dyes have been partly separated according to the chromatogram. The maximum theoretical plate number is around 1000 after 20 cycles. At the same time, *H* decreases from 1700 μm to 1220 μm, which also indicates increasing separation efficiency.

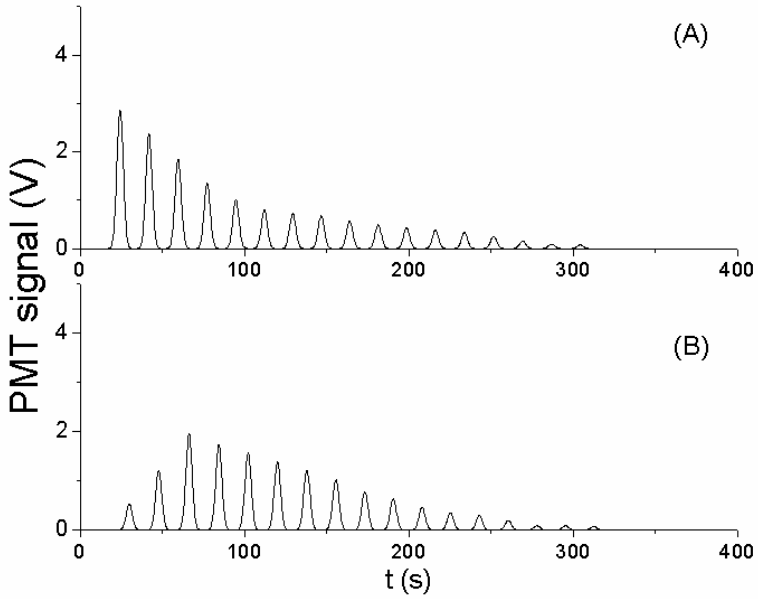

Figure 4.21: Simulated peaks of (A) rhodamine B and (B) fluorescein from experiment after normalized. These peaks are used to derive the parameters for separation efficiency of both fluorophores.

Rhodamine B shows the same good chromatographic performance. With improved setup and stationary phase coating, the *N* value can be increased and achieve extremely big values.

Besides theoretical plate numbers and HETP, the separation factor α mentioned in section 2.3.1 is another important parameter to describe the separation ability of the stationary phase. α should be greater than 1.0 when separation is efficient. The bigger the α is, the more capable is the stationary phase to selectively retain the components. The changes of α with cycles for both dyes are listed in section B.3. α is defined as $\alpha = t_{R2}/ t_{R1}$, where t_{R2} *(s)*, t_{R1} *(s)* are the retention time for rhodamine B and fluorescein respectively. Δt_R *(s)* is the time interval of two peaks in the same cycle. Δt_R can be used to represent the resolution when the dead time for each cycle is unknown in our experiment. The increasing time interval illustrates increasing separation efficiency. α

stays larger than 1.0, which represents that the stationary phase has good stability and strong separation capability and these abilities can last for at least 400 s during the whole separation process.

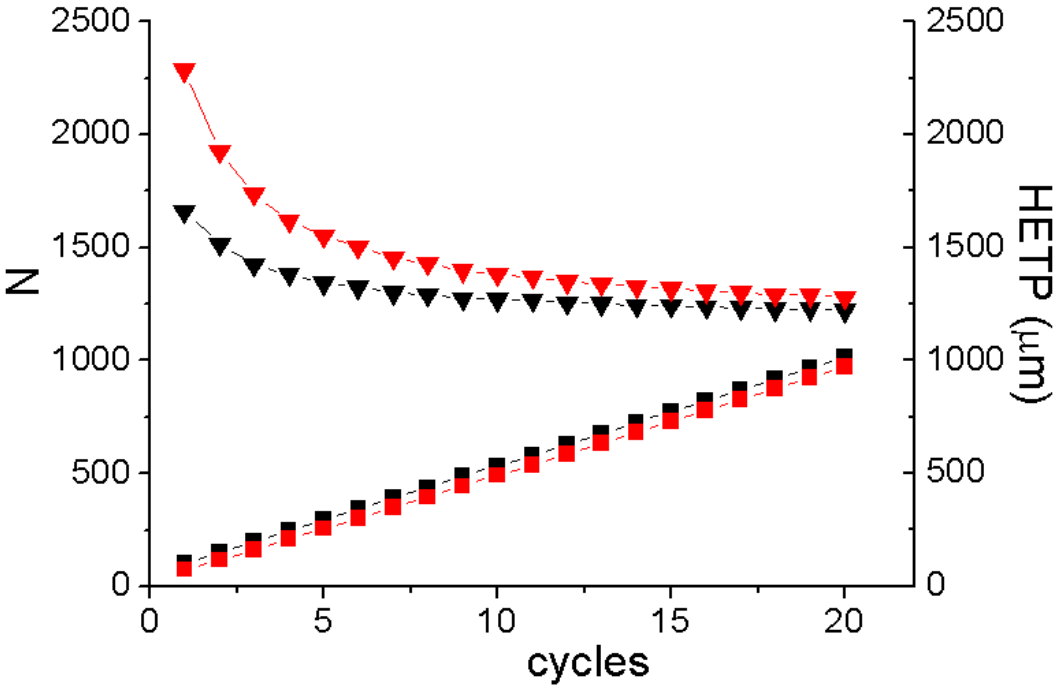

Figure 4.22: Plate numbers *N* and HETP changes with rotation cycles for both rhodamine B and fluorescein. Separation efficiencies for both rhodamine B (red color) and fluorescein (black color) increase, which is represented by increasing plate numbers (■) and decreasing HETP (▼).

The trends of α and Δt_R shown in figure 4.23 indicate that the stationary phase effectively maintains its separation ability for more than 20 rotation cycles, in terms of time duration longer than 350 s.

The increasing Δt_R in figure 4.23 is consistent with trends of *N* and *H* shown in figure 4.22. This proves again that the separation efficiency increases with rotation cycles. α is bigger than 1.0 throughout the whole separation process, which shows C18 coating is relative stable and has good separation performance.

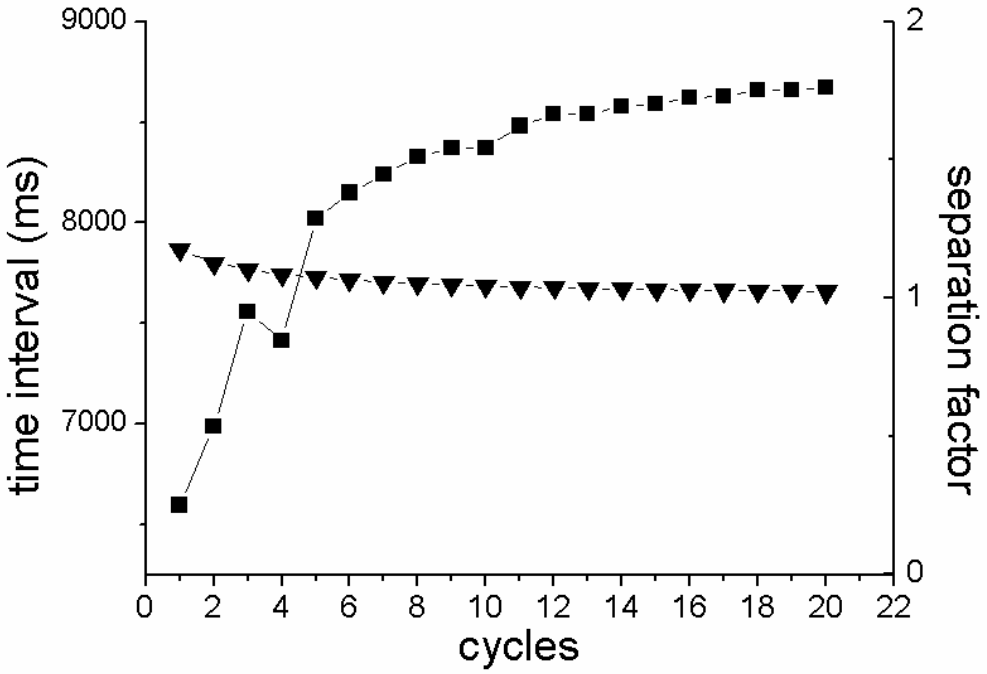

Figure 4.23: Time interval Δt_R (■) and separation factor α (▼) with rotation cycles for both rhodamine B and fluorescein. The separation efficiency increases with cycles with the increasing time interval. The separation factor stays more than 1 indicates that the stationary phase is capable through the whole experiment.

Besides the chromatographic performance, frequency information for rhodamine B and fluorescein in SDCC is also analyzed with FFT analysis. Their frequency information is supposed to explain the successful separation with solid frequency difference.

4.2.4 Frequency Analysis

Fast Fourier transform was used to transfer the time domain information into frequency domain for better S/N ratio especially for cyclic systems as discussed in section 3.2.2. In our experiment, FFT were carried out with the help of MATLAB or Origin 7.0 using the data acquired by digital-analogue converter (ADC, Pico Instruments). The program process is discussed in section B.4.

The small periodic peaks, which appear after 20 cycles give important frequency information in a long time period, although they are not taken into account in the chromatographic analysis. These peaks are amplified in figure 4.24.

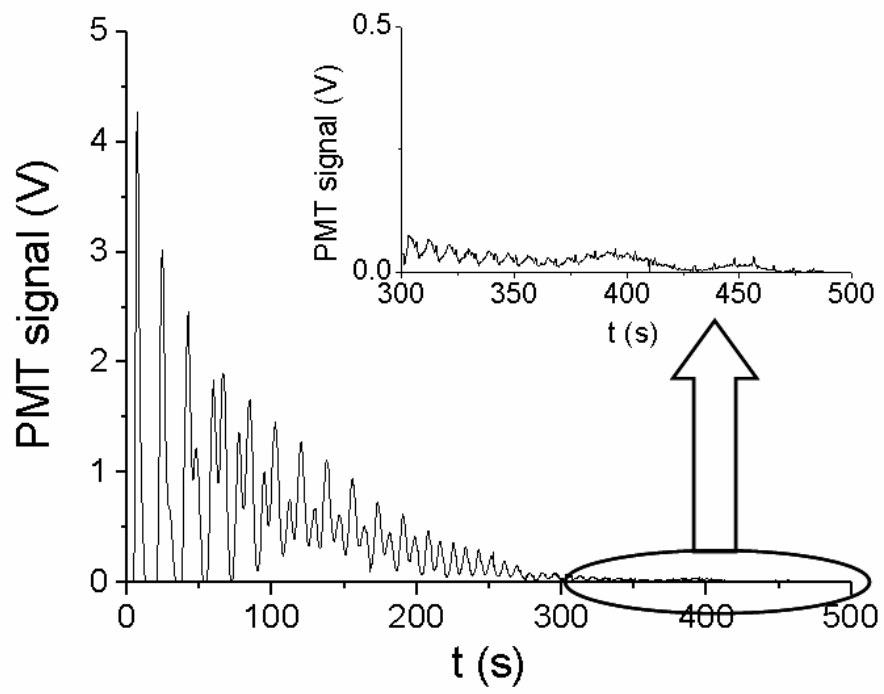

Figure 4.24: FFT analysis of signals collected for rhodamine B and fluorescein mixture solution in SDCC. The rotor has a frequency of 0.114 Hz. The periodic small peaks after 300 s contribute to the frequency analysis.

The frequency information is obtained in figure 4.25. In figure 4.25, the peak at the rotation frequency (0.114 Hz) attributes to the dirt attached on the rotating glass plate or the light diffraction and reflection. The band around 0 Hz represents irregular perturbation within the detection limit. The regularly paced frequency bigger than 0.114 Hz are due to the harmonic peaks companied when FFT is done for a long time period.

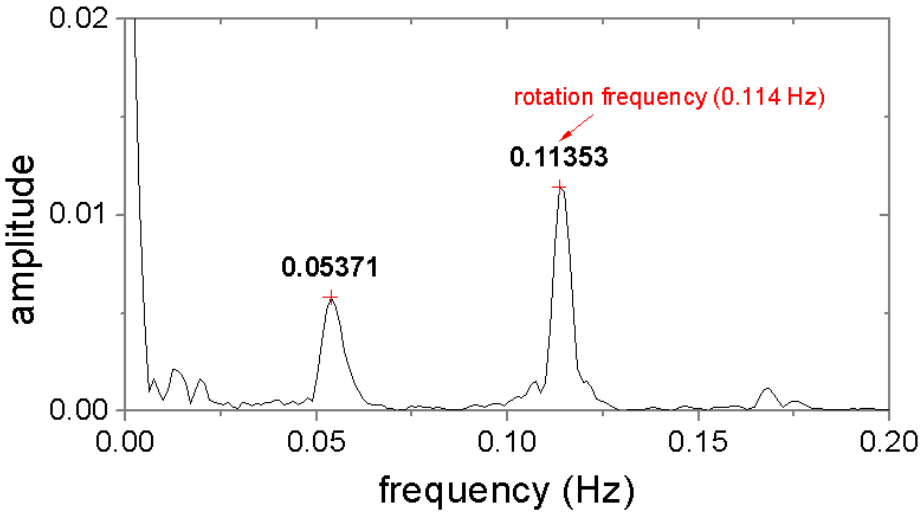

Figure 4.25: FFT analysis for SDCC experiment. The peak at about 0.054 Hz is assumed to be the frequency of analytes, which is near to the frequency of mobile phase.

Ideally the separated components should show two separate peaks in frequency domain graph, but in figure 4.25 only one broad peak is observed at about 0.054 Hz. This observation is explained in figure 4.26 where pure rhodamine B and fluorescein with multiple revolutions are compared with the same rotation frequency of 0.114 Hz. Rhodamine B has the frequency at 0.056 Hz in figure 4.26 (A), which is 0.002 Hz faster than fluorescein at 0.054 Hz (figure 4.26 (B)).

Therefore, the two frequency peaks are too close to give high resolution in FFT when their mixture solution is tested. They have 0.002 Hz difference in frequency, which means a time difference of about 1 s for each cycle. The flow of mobile phase predominates the movement of fluorophores, and the retention effect of stationary phase is rather weak, therefore the frequencies are close to half of the rotation frequency at about 0.054 Hz as shown in figure 4.26.

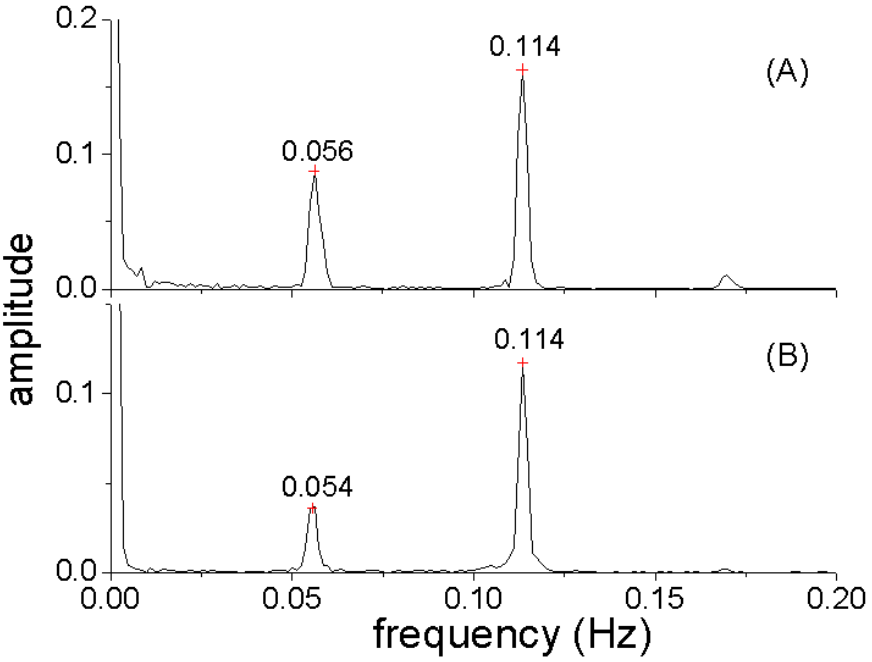

Figure 4.26: FFT analysis of signals collected with the rotor at a frequency of 0.114 Hz. (A) rhodamine B and (B) fluorescein. The frequency difference between the two fluorophores is only 0.002Hz, which is hard to distinguish in figure 4.25.

Theoretically the resolution of FFT peaks can be enhanced by collecting data for a longer period of time, as discussed in section 3.2.2. But in our experiment, a longer testing time doesn't provide a better resolution. Rhodamine B was taken as an example with the rotation frequency of 0.114 Hz. Figure 4.27 and figure 4.28 compare FFT analysis of rhodamine B with different time durations.

With longer time, signal at rotation frequency of 0.114 Hz has better resolution due to more data collected under this stable condition. But the S/N ratio for the mobile phase flow frequency is reduced with longer period of time, while the peak at the half of the rotation frequency decreases. The comparison is remarkable with obvious disturbance signal at rotation frequency as shown in figure 4.27. The mobile phase flow signal is weakened (figure 4.27 (B)) because more stationary phase particles disturb the fluid flow in a longer time period.

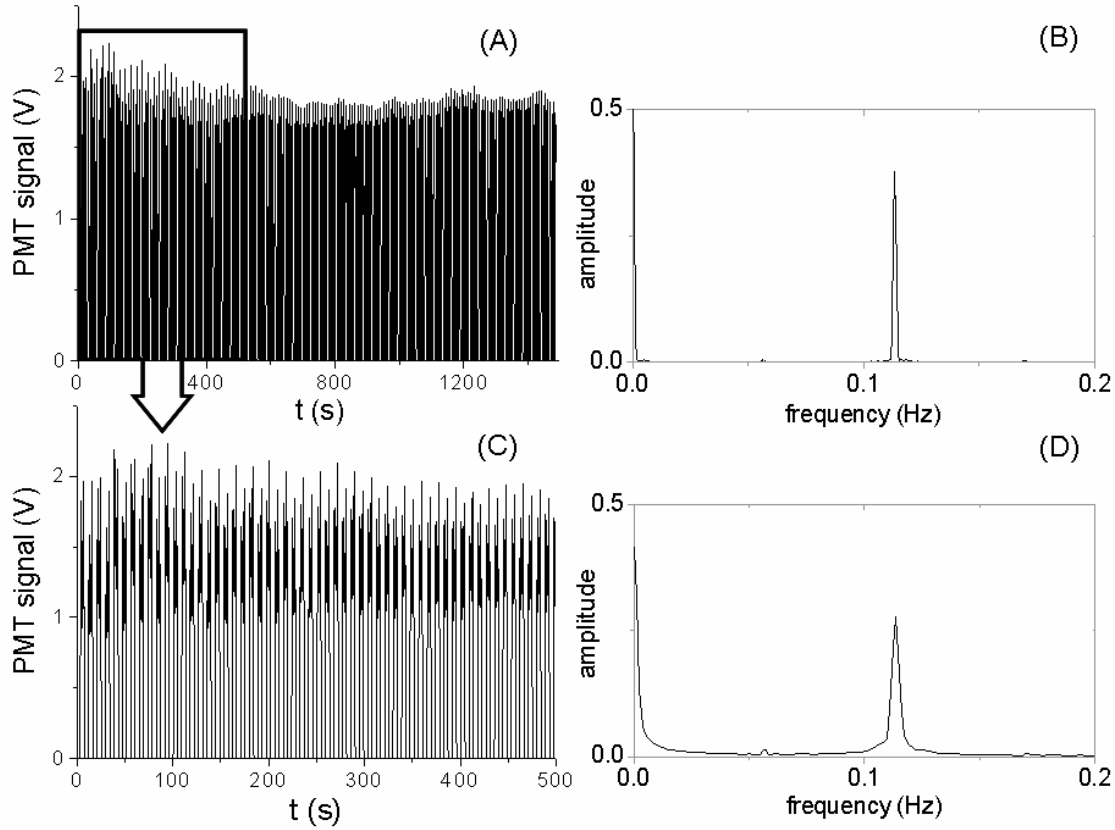

Figure 4.27: FFT analysis of fluorescein with rotation frequency at 0.114 Hz. (A) PMT signals for 1400 s and (B) corresponding FFT analysis are compared with time periods of 500 s ((C) and (D)). Longer time period shows better resolution in the frequency graph.

The disturbance at the frequency 0.114 Hz can be attributed to diffraction or reflection of the rotation plate, or exceeded dye residue on the plate. A black paper was attached at the back side of the rotation plate to minimize reflection and diffractions.

The periodic signals with the rotation frequency were reduced after the black paper was applied. The data collected in 2500 s in figure 4.28 (A) and (B) has worse peak resolution and less intensity at half the rotation frequency which concerns the sample flow frequency, when compared with shorter time period of 800 s (figure 4.26 (C) and (D)). More small peaks show up below 0.057 Hz in figure 4.28 (B) because

the stationary phase particles keep dropping off when flushed by mobile phase during rotation.

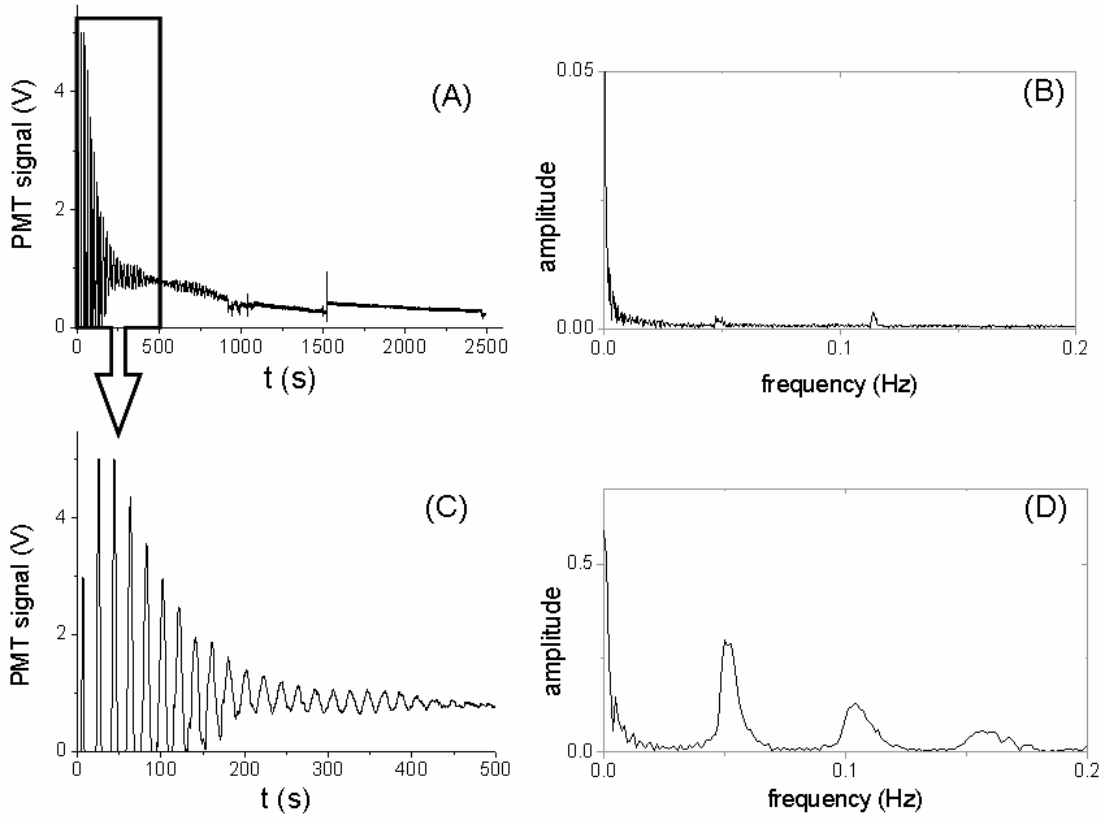

Figure 4.28: FFT analysis of rhodamine B with rotation frequency at 0.114 Hz. (A) PMT signals for 2500 s and (B) corresponding FFT analysis are compared with time periods of 800 s ((C) and (D)). Longer time period shows weaker amplitude peaks, which is opposite with the theoretical assumption in figure 4.27 because of the C18 particles peeling off and introduce more random frequency signals.

The particles flow in the mobile phase with various speeds and unstable flow conditions. These influences introduced perturbation to cause the small peaks or bands in the frequency information.

In every case, the fluorescent signals decrease and extinct after a certain time period. This phenomenon is attributed to the free diffusion and dispersion of fluorophore molecules.

4.2.5 Diffusion Coefficient

The existence of analyte concentration gradient forms a temporary boundary between analytes and mobile phase. Meanwhile, the concentration gradient enables the analyte molecules to pass the boundary and diffuse into the surrounding mobile phase. At last, the concentration of analytes will reach equilibrium. Our channel-free system makes use of the short time period to accomplish separation.

Sample molecules travel through the mobile phase or elute from the stationary phase during diffusion process. The diffusion effect in chromatographic columns leads to peak broadening and sample loss. The Van Deemter's equation[85] explains the diffusion components in packed column LC, which describes the relationship between HETP H and flow velocity u *(m/s)* of mobile phase.

In the Van Deemter's equation $H = A + B/u + Cu$, A is the diffusion of sample molecules into porous path in stationary phase which is called Eddy-diffusion. B/u is the longitudinal diffusion of sample molecules through the column. Cu represents the sample molecules diffusion between stationary phase and mobile phase, which is called mass transfer. With a certain flow velocity u, the H value will reach the minimum. This flow velocity u will give the packed column LC the highest separation efficiency.

The diffusion effect in the microfluidic chromatography system also leads to peak broadening; however the diffusion model is built up based on molecule traveling freely in the free paths. This model follows Einstein-Smoluchowski equation[86] (equation.4.3). The diffusion coefficient D *(cm²/s)* is defined by the mean free path λ *(cm)* and the average time between collisions τ *(s)*.

$$D = \frac{\lambda^2}{2\tau} \quad (4.3)$$

Flow injection analysis[87] and electric field[88] in microfluidic devices have been utilized to study the diffusion coefficient D. In the SDC channel, the diffusion coefficients for different dyes were measured with static method[89].

Experiment

In our experiment, the sample molecules were driven by shear force in a circular track. At the same time, diffusion of sample molecules in all directions was also taking place. This effect leaded to the expansion of the sample area and peak broadening. As illustrated in figure 4.29, the tangential velocity of sample depends on the radius value when the rotation frequency is fixed.

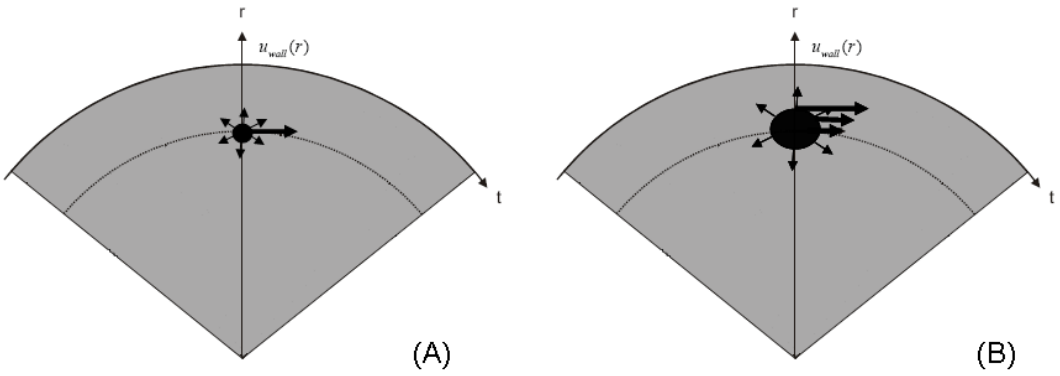

Figure 4.29: Samples flow profiles by the shear force and the molecules free diffusion paths. (A) The initial sample area and (B) the sample area after several rotations, the area increase is due to both shear force in the direction of circular track and diffusion effect in all directions.

Taking rhodamine B as an example, the peak broadening processes are recorded and the peaks are simulated into a serial of Gaussian curves with the same baseline. They are used to describe the cumulative spread of small variations during the diffusion. More details are discussed in section B.5. The peak information such as peak widths, peak heights and peak areas with cycles are listed with cycles in table B.5. The peak broadening and peak loss were demonstrated by increasing peak width and decreasing peak area. The trends of peak width and peak area with rotations are shown in figure 4.30.

The peak broadening reflects the diffusion in the circular track; however the loss of the peak area represents the dispersion of molecule out of the circular track. When

the flow velocity stays the same, the change of peak width can be used to calculate the diffusion path length. The diffusion time equals to the rotation time.

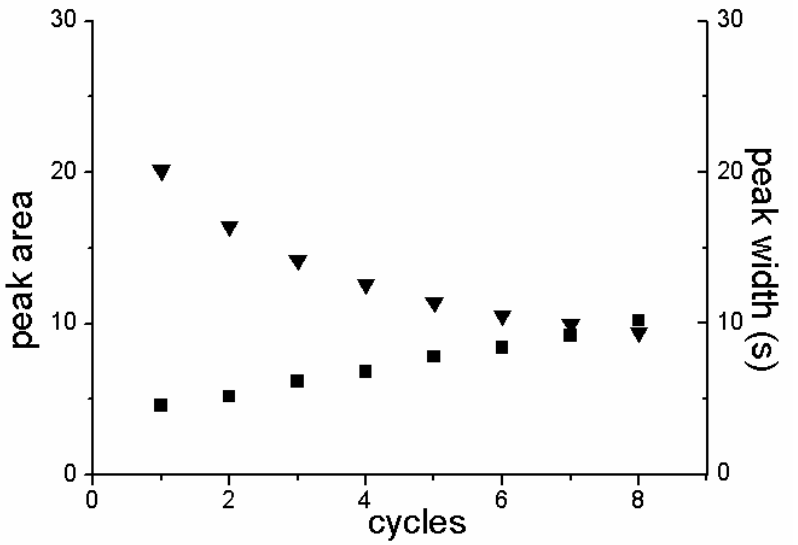

Figure 4.30: Peak width (■) and peak area (▼) trends of rhodamine B with rotation frequency of 0.114 Hz. Peak area decreases and peak width increases because of diffusion and dispersion.

The variance of peak width reveals the pure molecule diffusion with time. Equation 4.4 is derived from equation 4.3 to calculate the diffusion coefficient in our experiment. In equation 4.4, *u (cm/s)* stands for flow velocity; *σ (s)* is time variance which is peak width variance; and *t* represents the diffusion time, which is the time difference between the peak maximum positions for the corresponding peak variances.

$$D = \frac{(\sigma \cdot u)^2}{2t} \quad (4.4)$$

The time variance σ increases with the rotation cycles, which is shown in figure 4.31. In figure 4.31, the peak variance $(\sigma \cdot u)^2$ is plotted versus time and the slope is equals to two times of diffusion coefficient *D*. With the $r^2 = 0.938$, the mean flow rate *u* is 3.22 mm/s with rotation frequency at 0.114 Hz, the diffusion coefficient *D* is calculated to be 6.03×10^{-3} cm^2/s. Compared with the rhodamine B diffusion

coefficient measured with static method in aqueous solution[85] (4.27×10^{-6} cm^2/s), D in our experiment is much bigger. While the diffusion coefficient was measured in a kinetic system, which enhanced the sample molecules dispersion compared with in static method. The channel-free condition had less restriction for molecule dispersion than in micro-channels[87].

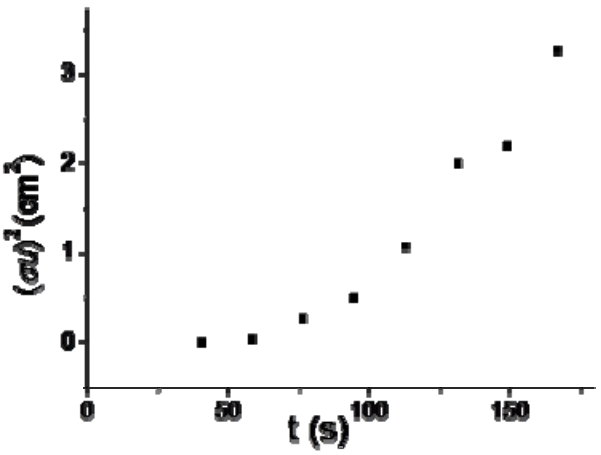

Figure 4.31: Peak variance $(\sigma \cdot u)^2$ with retention time t for rhodamine B when rotated with 0.114 Hz in SDCC. The diffusion coefficient of rhodamine B in the circular kinetic system is calculated to be about 6.03×10^{-3} cm^2/s according to this graph.

4.2.6 Other Applications

SDCC is successful in separating fluorescent dyes not only for rhodamine B and fluorescein, but also for fluorescein and coumarin 307. Solution of 5 mM coumarin 307 ($C_{13}H_{12}F_3NO_2$, Radiant Dyes Chemie, Wermelskirchen, Germany) and 5 mM fluorescein mixture in methanol was injected manually. With the mobile phase of 30% (v/v) water in methanol solution, the resolution of 1.02 is satisfying, as shown in figure 4.32 (A).

Because coumarin 307 has the excitation wavelength (Ex) at 480 nm and the emission wavelength (Em) at 530 nm and fluorescein has the Ex at 490 nm and Em at

520 nm, RET effect doesn't occur in the chromatogram in figure 4.32 (B). After the separation, the peak intensities of both fluorescein and coumarin 307 decrease with rotation cycles. Fluorescein has higher polarity, hence the fluorescein peaks show up earlier than the coumarin 307 peaks. After five cycles, the fluorescein peaks are already very weak due to dispersion. The theoretical plate numbers for both fluorophores are less than 1000.

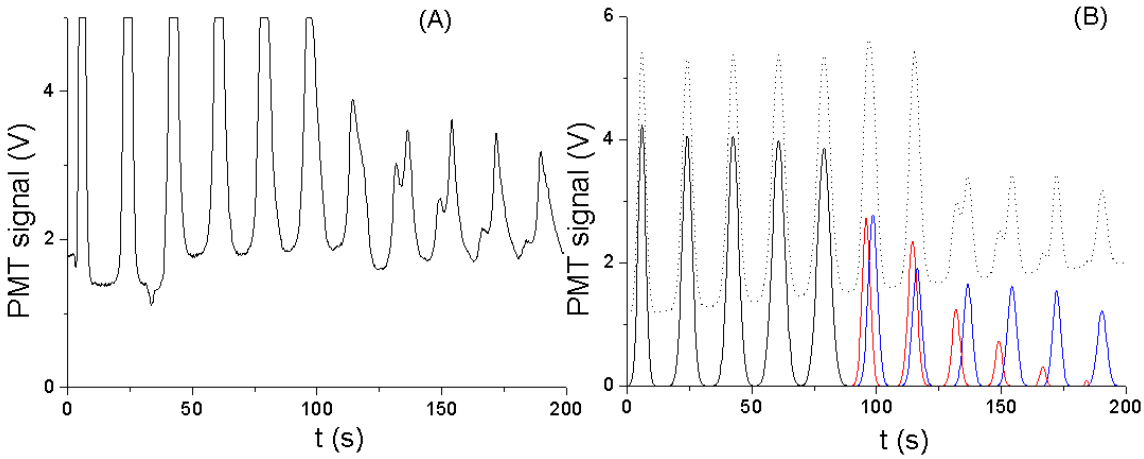

Figure 4.32: Chromatogram of fluorescein and coumarin 307 with SDCC. (A) Experimental peaks by PMT, and (B) simulated peaks by PeakFit v4, red peaks represent fluorescein and blue peaks for coumarin 307. The red peaks in (B) represent fluorescein and blue peaks are coumarin 307. The theoretical plate numbers for both fluorophores are less than 1000.

4.3 Summary

Since delicate mechanical design is critical to validate SDCC, the setup with better rotation stability was chosen to carry out the experiment. Then both theoretical model and experimental proofs are introduced in this chapter.

The roughness and thickness of the stationary phase are particularly important for high performance SDCC separations. The stationary phase coating procedure

consisted of pretreatment and silanization. Characterization was carried out by WLI and contact angle measurements. At last, the 2% HF solution pretreatment and immersion method were chosen to prepare all the C18 coated glass plates.

A novel channel-free microfluidic chromatography system with a rotating plate described in chapter three has been successfully used for the shear driven circulation and separation of fluorescent analytes described in this chapter. It is the first time to report the successful shear driven chromatographic separations within a circular system[90].

The chromatographic performance was characterized with theoretical plate number, HETP and separation factor. All of the parameters demonstrated increasing separation efficiency with rotation cycles, which is the original purpose of SDCC. A trial to utilizing magnetic particles has given a new idea for the stationary phase coating. Magnetic particle is a kind of media to help stabilize the siloxane linkage.

FFT was applied to analyze frequency information of analytes in the SDCC experiment. The assumption that linear shear driven velocity profile makes the mobile phase move with half of the rotor speed was proven by FFT. The analytes were retarded by the stationary phase with different extent because of their different polarities, and their rotation frequencies are therefore also different.

Although mathematical models have been built up for some specialized laminar flow diffusions in microfluidic system[91][92], the kinetic diffusion of microfluidic flow remains a big challenge because of the extremely small liquid volume and delicate micro-structures in the channels. Temperature and pressure are constant in microfluidic devices; therefore they have little influence on the free diffusion of sample molecules in our experiment. In the chromatogram, the peak area is proportional to the amount of sample stayed in the circular track whilst rotating. The sample loss causes decreasing sample concentration and reduces the peak area. The photo-bleaching of fluorescent molecules, which contributes to the decay of peak intensity, accelerates the decreasing of peak areas.

CHAPTER FIVE: INTEGRATION OF AN AUTOMATED INJECTION SYSTEM WITH SEPARATION PLATFORM

5.1 Introduction of Injection with Micro-channel

Injection system is an important component in the μ-TAS. Due to the small sample volume usually involved in the μ-TAS, injection system directly affects the detection sensitivity. Sample pretreatment such as preconcentration is sometimes applied before injection to enhance the detection limit. The injection methods can be generally divided into volume-based and time-based sample injections[93]. Time-based method is to control the time of the injection process rather than the volume of the sample. This method is always used to compare the different injection amount in a group of experiments. Volume-based injection method needs an injection channel for each different volume; however time-based injection method needs only one channel for series of volumes. Therefore, time-based method is more reliable with less system errors.

Meanwhile, time-based method has more flexibility in chip designs, when the injection is not defined strictly by the geometric design as in the volume-based method. For both methods, the hydrodynamic and electrokinetic injection models have been built up to accomplish different tasks.

More specific injection methods have been studied to optimize the injection

step in the μ-TAS. For example, in micro-channels, the pinched electrokinetic injection method can focus the microfluidic flow to reduce band broadening and decrease sample leakage[94]-[96]. Hydrodynamic pinched injection method has been developed recently[97]-[99] to overcome the side effects occurred when the electric field applied in the micro-channels made of polymer, because the polymer surface would carry electric charge in electric field and interfered the microfluidic flow profile. Other examples such as injection in parallel arrayed narrow channels[100], spontaneous spray injection for CE[101], optically gated sample injection in multi-channel system[102], and gravity driven flow injection[103] all belong to continuous injection, which is the dominant injection method for both time-based and volume-based injections. Recently, evaporation driven transportation of water to microfluidic networks based on mimicking the function of plant leaf was reported to have a potential application in a microfluidic system[104].

In shear driven linear chromatography, an automated hydrodynamic injection method with micro-channel was developed[105]. The sample plug was injected and transported by a movable wall to the separation channel. In this experiment, hydrodynamic injection method is tried in both models: with micro-channel and without micro-channel.

5.1.1 Fabrication of Micro-channel

The square soda lime glass plates (Nanofilm, Westlake Village, CA, USA) with the size of 76.2 mm × 76.2 mm used as the mask are pre-coated with 5300 Å positive photoresist (AZ 1518, baked at 103ºC for 0.5 h) layer, which is on top of a 100 nm chromium layer.

The fabrication of glass chip consists of photolithography and HF etching as shown in figure 5.1. In the photolithography step, the chip design was drawn with AutoCAD 2004 and printed out on a plastic film as a photo mask. The photo mask was placed on the coated glass plate and exposed under the MEGA UV Exposure

Unit LV 202E (RS, Corby, UK) for 5 s. After the exposure, photo mask was restored immediately in the protective holder to keep it away from being polluted by the solution. The exposed glass plate was developed for 60 s by a standard developer solution with 20% (v/v) Microposit 351 Developer (Shipley Europe Ltd., Coventry, UK) in ultra pure water (Merck, Germany) to remove the photoresist layer. Then the glass plate was rinsed with bidistilled water and dried with nitrogen, and immersed into chromium etching solution (Lodyne, Microchem Systems Ltd., Coventry, UK) to remove the chromium layer. After both the photoresist and chromium function layers were removed, the glass plate was rinsed with bidistilled water and dried with nitrogen gas again. This glass plate prototype can also be used as a photo mask to produce more glass plates.

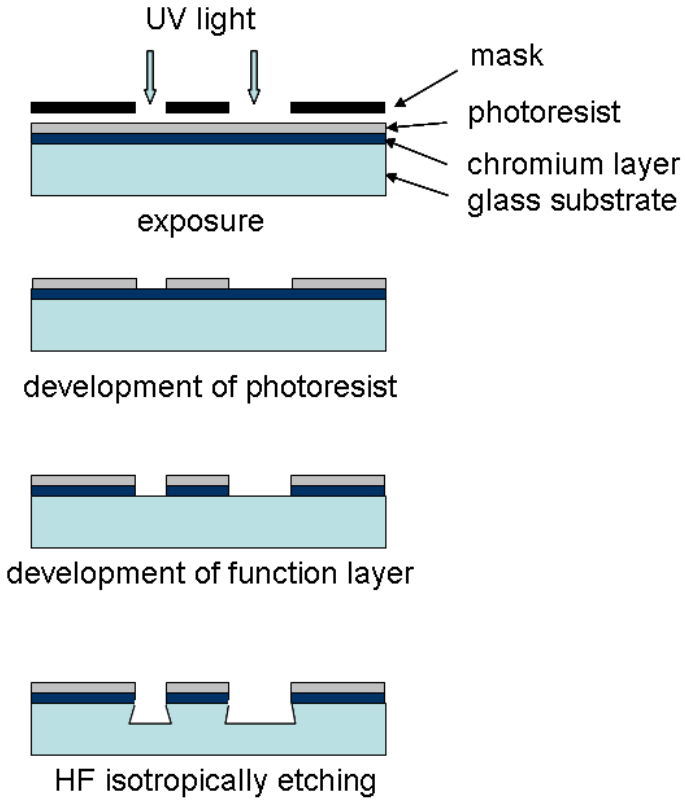

Figure 5.1: Photolithography and HF etching processes with soda lime glass. After exposed under UV light, the photoresist layer is removed firstly, and then the function layer with chromium is removed by etching solution. The glass chip is etched with 5% (v/v) HF in water solution at last.

After the photolithography step, the chip design was ready on the glass plate. In the next step, HF etching was carried out by immersing the prepared glass plate into a diluted HF solution with a concentration of 5% (v/v) in water solution. The substrate was isotropically etched with a certain rate depending on the HF concentration.

Theoretically, wet etching of glass is an isotropical etching process. This means that the process features the channel width wider than the mask width as shown in figure 5.2. The bottom of the channel stays smooth and optically transparent. The under-etching occurs under the chromium layer, which has the same etching rate with the in-depth etching. The width of the channel is more than twice the depth of it, and the corners are rounded. The degree of under-etching W (μm) is equal to the channel depth d (μm). And the channel width W_{chip} (μm) can be calculated by $W_{chip} = W_{mask} + 2d$.

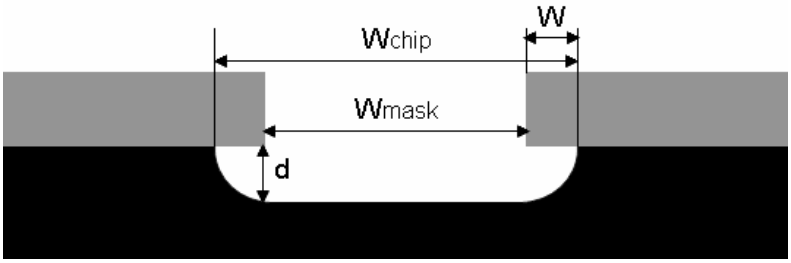

Figure 5.2: Illustration of etching effect under the mask. The width of the channel is more than twice the depth of it, and the corners are rounded. The degree of under-etching W (μm) is equal to the channel depth d (μm). And the channel width W_{chip} (μm) can be calculated by $W_{chip} = W_{mask} + 2d$.

The HF solution was recycled in the experiment; and the etching rate was recorded as a standard for the HF concentration. The etched channel was measured by microscope (Nikon, Japan) and the depth was equal to the under-etching width on both sides of the channel.

At last the rest part of the glass with photoresist and chromium layers was removed with Dimethylformamide (DMF) and chromium etching solution. All the development solutions were recycled and renewed once a week in our lab. After the glass plate with channel was fabricated, holes were drilled by the metallic drill (Proxxon Micromot System GmbH, Germany) with the head of 1 mm in diameter and drill press (Micro Miller MF 70, Proxxon, Germany) for tubing connection.

After the fabrication, glass plate with the injection channel was tested.

5.1.2 Injection Control

Rotation experimental arrangement A discussed in section 3.1.2 was used to integrate the injection system. The rotatory motor with vacuum pump was placed on top of the stationary stage. Restricted by the experimental arrangement, the injection tubing could not rotate with the rotor. Therefore, the injection channel was fixed with the stationary stage and the injection was introduced with the inlet and outlet reservoirs from the bottom (figure 5.3).

Experiment:

The injecting and withdrawing syringes were held by a mechanical pump (Technical & Scientific Equipment GmbH, Germany). Two different types of tubing were used: silicon tubing (Cole Parmer Instrument Company) and capillary PEEK tubing (Western Analytical Products, CA, USA). The syringes were connected to the glass plate with silicon tubing, which was glued to the syringe on one side and connected to the micro-channel by capillary tubing on the other side. The inner diameter of the capillary tubing is 50 μm and the outer diameter is 350 μm. The capillary was fixed by epoxy resin (Araldite, Germany). At last, the glass plate with silicon tubing was heated to 70ºC in the oven for at least 2 h to firm the resin.

Time-based injection method was utilized in the experiment. The volume of the sample injected was controlled by the injection rate and injection time. The injection process consisted of two steps: channel-filling and sample transportation. After the micro-channel was filled with sample solutions, the injected portion was transported by the cover glass plate to the separation track which was 14 mm away from the injection position. This movement was carried out by the rotation glass holder made by ISAS workshop. The rotation glass holder was designed to hold the round glass plate and move linearly towards the bottom glass plate.

The moving distance and velocity were controlled by tuning the screw manually. The whole hydrodynamic injection setup is illustrated in figure 5.3, with the magnified injection part with inlet and outlet tubing.

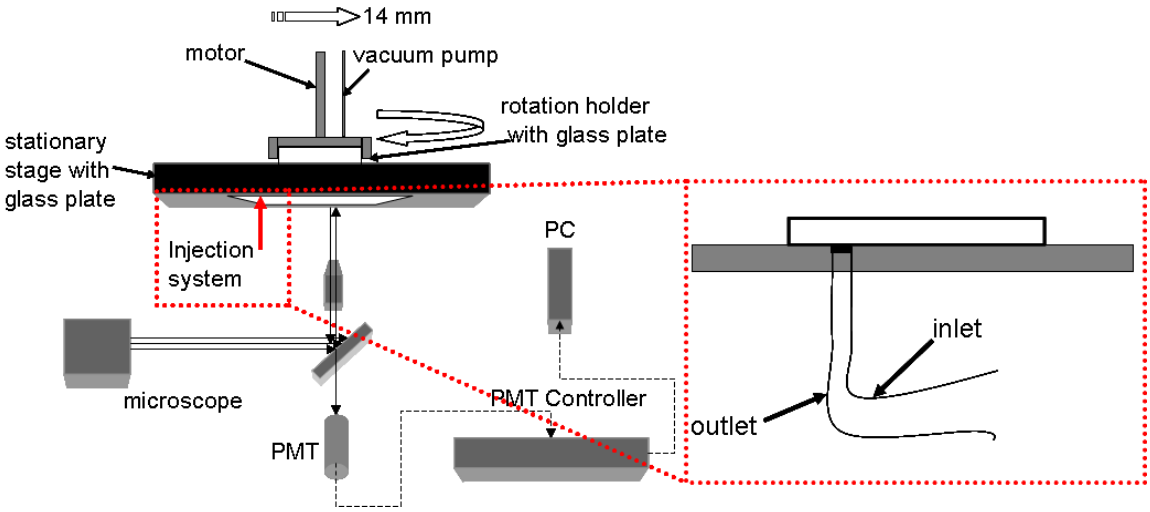

Figure 5.3: Schematic illustration of injection setup. The injection is carried out with inlet and outlet tubings.

Two chip designs with different channel lengths of 5 mm (figure 5.4 (A)) and 7 mm (figure 5.4 (B)) were drawn with AutoCAD 2004. The channel widths were both 0.5 mm. Channels were aligned 25 mm from one side of glass plate

according to the experimental arrangement.

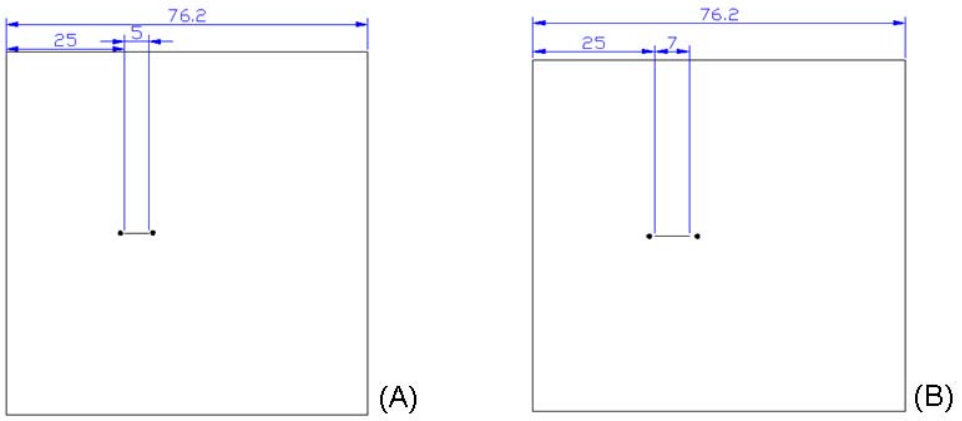

Figure 5.4: Chip design for injection channels with channel widths of 0.5 mm and different channel lengths of (A) 5 mm and (B) 7 mm. Unit: mm.

In order to acquire images with better contrast by the CCD camera, the photoresist and chromium layers on the rest parts of the glass plate were kept. Therefore only the fabricated channel was transparent. Using the standard wet etching method described in section 5.1.1, the injection channels in our experiment were fabricated to be about 20 μm deep. The width of the channel was 0.54 mm (0.5 mm + 40 μm) according to the description in section 5.1.1. The flow velocity was determined by the pushing and withdrawing pressures applied at both ends of the channel.

Results and Discussions:

Due to the limitation of microscope observation, only a small part of the whole channel with the length of 5 mm was able to be recorded, which was about 1.5 mm (figure 5.5). Considering capillary force effects between the two hydrophilic glass plates, the outlet rate (27 mL/h) was set to be three times as fast as the inlet rate (9 mL/h) to drive the injection stream to flow in the desired

direction. Although most of the injected sample flows in the channel, the leakage flow out of channel is unavoidable (figure 5.5). The stream flows with a parabolic head and broad shoulders. The flow profiles from 1s to 4s reveal that in the unsealed channel system, the capillary force is unavoidable due to the slit distance between the two glass plates. The injected sample liquid firstly disperses and fills the gap around the inlet reservoir, then flows towards the outlet reservoir driven by the pressure difference. The existence of 20 μm deep channel is not able to prevent the microfluidics from flowing outside. However, the main flow direction was well controlled in the experiment.

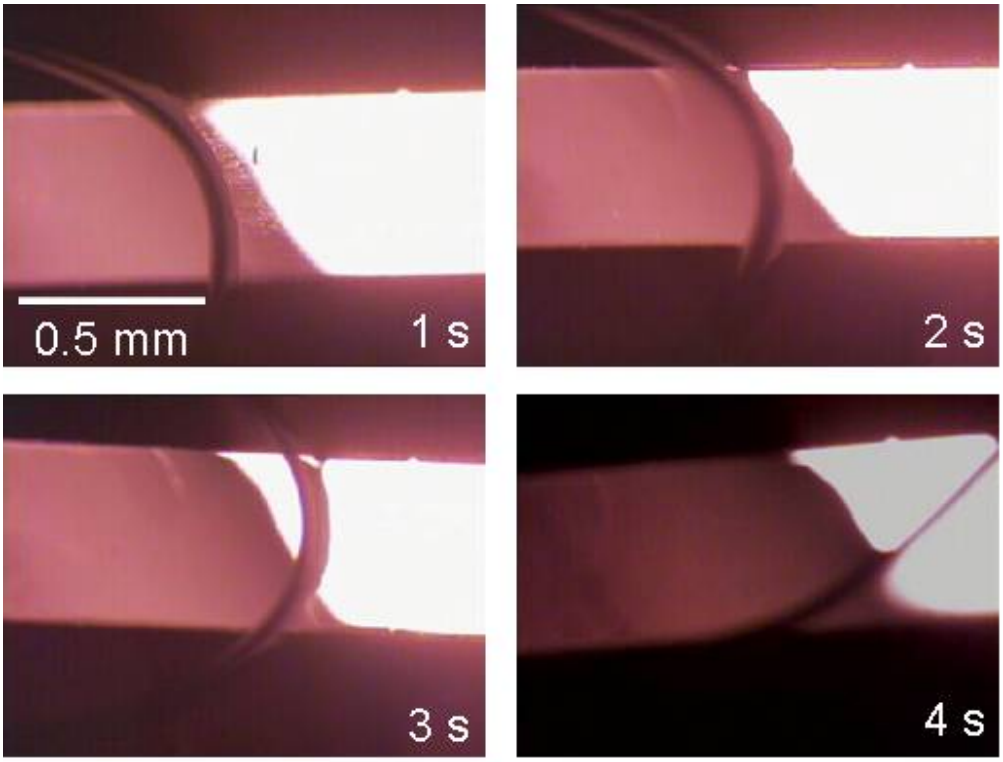

Figure 5.5: Chronological images of injection flow profiles in the 5 mm long channel, which is 20 μm in depth and 0.54 mm in width. From 1 s to 4 s, the microfluidic flows along the channel from inlet to the outlet reservoir. The leakage flow out of the channel is obvious even with higher outlet speed and lower inlet speed.

Injection flow behavior in the channel with a length of 7 mm was compared with the 5 mm channel. It is found that channel lengths made no obvious changes. The injected fluid rinsed the area around the channel inlet reservoir and then moved towards the outlet. With longer flow path, the flow profile had broader shoulders and the control of flow was poorer.

In order to decrease the dispersion area of sample flow at the inlet reservoir, the pressure difference applied was increased by increasing the withdraw speed to 45 mL/h. After the injection channel was filled, in some case the air around the channel was sucked into the fluid flow and bubbles were formed.

Taking 7 mm long channel as an example, the air bubble flow profiles in the injection channel are shown by time in figure 5.6. The existence of bubble weakens the quantification function of injection process. The air bubble grows with time (figure 5.6) because of the lasting unequal inlet and outlet volume, and no enough liquid is injected to compensate the volume loss.

Another potential problem raised with increased pressure difference was the thickness change of the space between two plates. The system was not isolated from the environment. Therefore, when the air between the two glass plates was sucked to the outlet reservoir, the air outside the system intruded to fill the space. This unstable condition induced turbulence between the two glass plates.

In order to avoid producing air bubbles, the two-plate system should be surrounded with the same liquids. However if the injection part is to be integrated with separation system, the injection part should be immersed in mobile phase solution, and this will lead to unknown mixing between sample and mobile phase. Therefore the concentration of sample is unable to qualified and standardized. The injection system loses its reproducibility and precision.

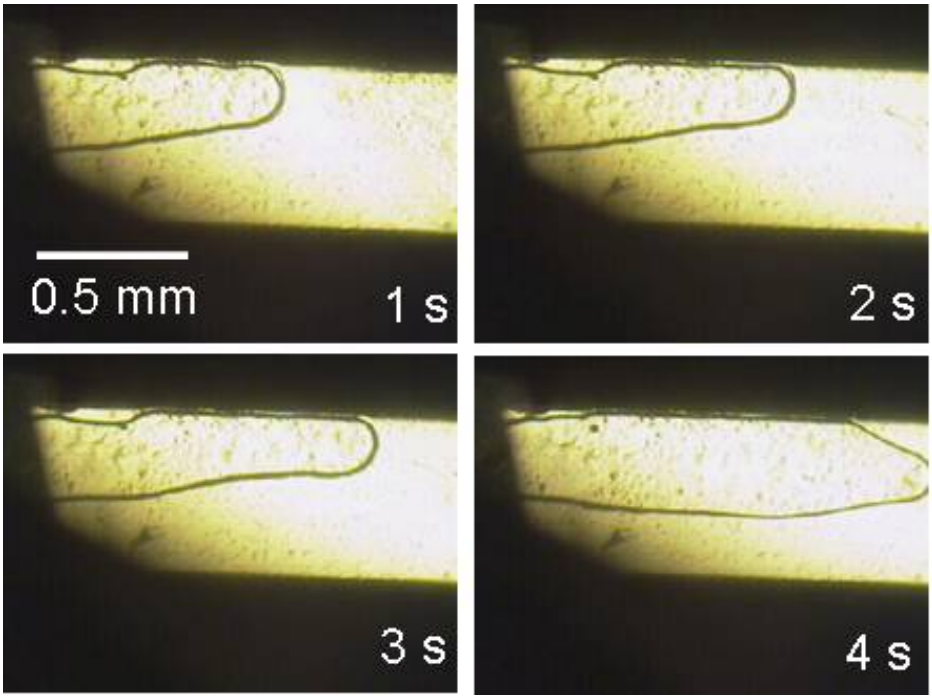

Figure 5.6: Bubble flows in the 7 mm long injection channel with injected microfluid. From 1 s to 4 s, the bubble appears and grows with time through the channel. The channel is 20 μm in depth and 0.54 mm in width.

.

Since the injection with channels showed many disadvantages, the injection was simplified into channel-free method, which was consistent with channel-free separation method discussed in section 4.2.

5.2 Channel-free Injection

The experimental arrangement was similar to injection-with-channel method as shown in figure 5.3, but only one inlet hole was drilled instead of channel with both inlet and outlet. The sample was injected hydrodynamically through the hole onto the glass plate. The connection method was the same as described in section 5.1.2.

Experiment:

In order to minimize the influence of evaporation during the process, water was used as the mobile phase and all the samples were dissolved in water.

Before the injection, air bubbles in the tubing were driven out until a small amount of sample came out of injection tubing. After water was perfused on the bottom plate, the other glass plate was laid on top carefully to extrude the air pockets.

The sample was injected by syringe with a proper injection velocity, and the injection volume was controlled by the injection time. The injection velocity is to be optimized with experience. Because the sample solution in the tubing would mix with water and diffused to the water film when injection was too slow. On the other hand, too fast injection led to sample springing out suddenly when the cover glass plate moved at the beginning of the transportation step, while the back pressure was too high when the volume changed within such a short time in the silicone tube.

After injected, the sample was transported into the separation track by the cover glass plate, with a proper moving speed. The speed was also to be optimized with experience. If the cover glass was moved too fast, some samples had no time to travel along and stuck to the bottom plate to leave a "sample trail". This led to the sample loss. If the sample was transported with too low speed, the dispersion of sample molecules induced that the area of sample solution expanded enormously when it arrived at the separation track. Therefore the peak width was wide and peak shape was poor from the beginning of the rotation process. During the transportation, the cover glass plate should be kept strictly parallel to the bottom one to ensure that the cover glass moved smoothly. Otherwise the sample flowed away out of the detection window because of the perturbance. At last, the injection quality was checked when the motor started to rotate.

Results and Discussions:

2 µL of 5 mM amino black 10 B ($C_{22}H_{14}N_6Na_2O_9S_2$, Merck, Germany) solution in water was injected and the transportation process was recorded by the CCD camera as shown in figure 5.7.

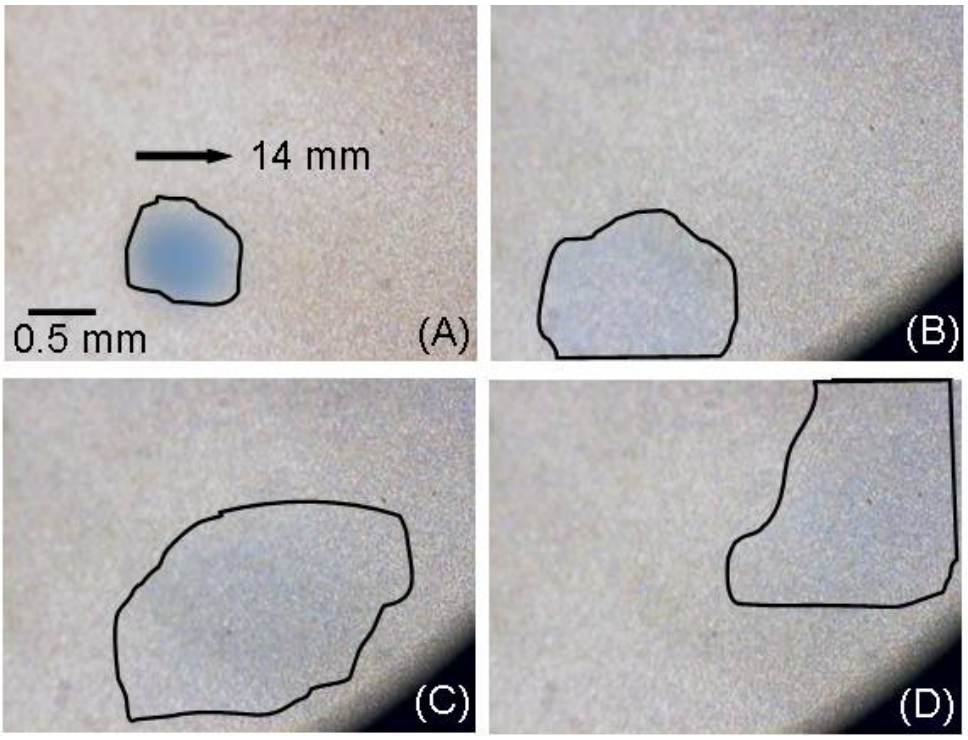

Figure 5.7: Transportation and rotation process of amino black 10 B dye solution after the channel-free injection in a chronological order from (A) to (D). Mobile phase is water and the rotation is anticlockwise. Before the rotation starts, the diffusion is not fierce and the boundary between dyes and mobile phase is still clear. That means the transportation step is effective.

Without an outlet, the injected sample only diffused statically before the transportation process began. After the dye was injected (figure 5.7 (A)), this portion was transported to the separation track in figure 5.7 (B), and the area expanded during transportation because of dispersion. When the rotation started,

the boundary became unclear and the sample started to merge into the mobile phase in figure 5.7 (C) and (D). These pictures indicated that the transportation was effective and the dispersion of sample molecules was not prominent compared with the dispersion occurred in the following rotation process.

Furthermore, the injection was integrated with rotation process. 2 μL of 5 mM fluorescein sodium salt in water solution was injected and the fluorescence was recorded when rotation step began. The frequency of rotatory motor was 1.41 Hz. The CCD images of the whole injection and rotation processes are discussed in section C.1, and the PMT signals are shown in figure 5.8.

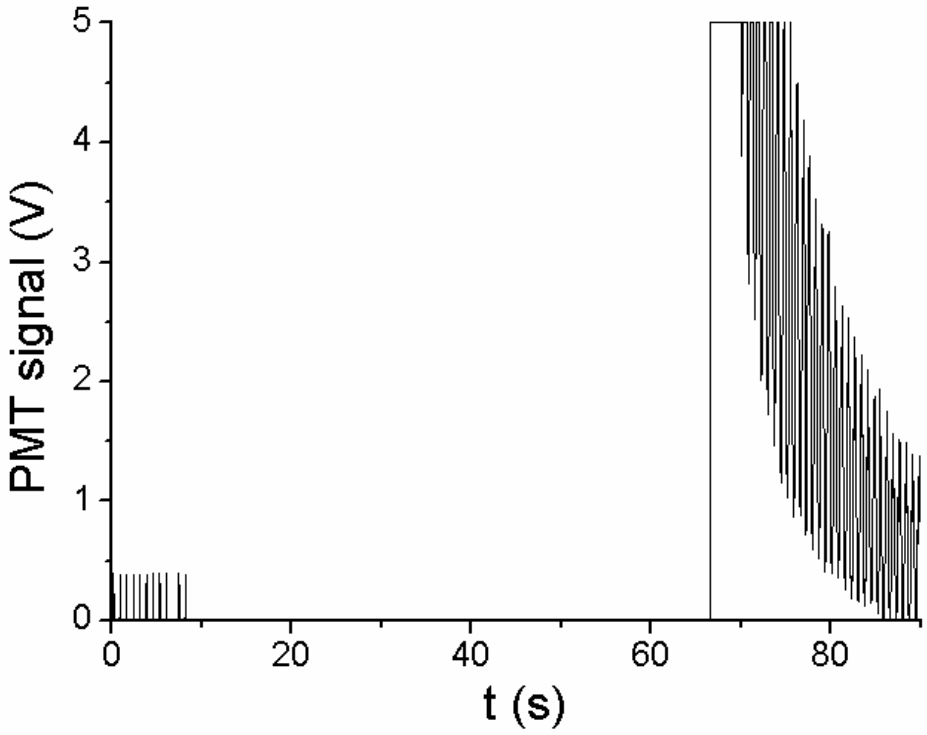

Figure 5.8: PMT signal for fluorescein injection and rotation. From 0 s to 65 s, the samples are transported from the injection track to the separation track. From 65 s on, the samples are rotated in the separation track. The fluorescence intensity increases suddenly to maximum indicates that the transportation step is effective.

As shown in figure 5.8, the whole process including injection and rotation lasted for longer than 90 s. At 0 s, 2 μL fluorescein samples were injected between two glass plates hydrodynamically through silicone tube. From 0 s to about 65 s was the transportation step before the injected sample reached the observation region. Some small peaks on the PMT diagram from 0 s to 10 s were due to the perturbation occurred when the cover glass plate moved with the rotatory motor. At about 65 s, the sample was transported to the destination successfully and the fluorescent intensity increased quickly to maximum. The sharp increase indicated that only limited amount of sample dispersed in to the mobile phase and the concentration stayed in high level. The boundary between the two different liquids was still clear after transportation step. When the rotation started, the peaks intensity decreased with time because of sample dispersion.

5.3 Summary

A semi-automated hydrodynamic injection system was built up in order to quantify the sample injection and enhance experiment reproducibility. In previous SDCC work[50], the injection channel was designed across the annular separation channel in microfluidic system, which led the sample to remix with the residue in the injection channel with each cycle and produced artifact peaks. In order to eliminate the artifacts, sample transportation distance of 14 mm was introduced to keep injection and separation tracks apart.

Microfluidic channels fabricated in glass substrate were tried firstly and the channels were not capable of preventing the flow leakage. Hence, channel-free injection method was chosen due to its better performance and geometric fitting to the following channel-free separation step. With the channel-free injection, the free interfacial diffusion of molecules maintained the concentration of the injection sample during transportation in only a short time period before rotation. Fluorescein was successfully injected and transported to the separation track with

considerable reproducibility.

The channel-free injection system demonstrates its potential to approach closer to automation.

CHAPTER SIX: SUMMARY AND OUTLOOK

6.1 Summary

The miniaturized separation techniques are blooming in analytical sciences for chemical, biological, and pharmaceutical applications. Their advantages in cutting down the consumption of analytes, simplifying operation processes, and their flexibility for integration are well recognized. The achievements of this research project exposed an application possibility of a novel microfluidic separation method in μ-TAS separation platform. This microfluidic separation method "channel-free shear driven circular liquid chromatography" is introduced as a cyclic liquid chromatography technique into μ-TAS.

In order to validate the channel-free shear driven circular liquid chromatography, a rotating microfluidic system was established with two different designs. Soda lime glass is chosen to provide the microfluidic environment for its optical transparency and adequate mechanical hardness. One round glass wafer laid on the top of another square glass plate forms a channel-free microfluidic system. The rotation movement is accomplished by a rotatory motor which holds the upper glass plate. The stable rotation condition including constant rotation frequency and constant thickness of liquid film is critical in carrying out successful separations. Meanwhile, the centrifugal force has to be eliminated with low rotation frequency to keep the sample in the separation track, when no micro-channel exists.

Firstly, the two setups were tested to investigate their stabilities and potential application abilities. The property of the bottom glass surface was measured and compared after rotation. With one setup, many scratches showed up and indicated the

changing thickness of liquid film; and the upper glass plate has motion freedom in x-axis. Therefore this setup is not suitable to realize shear driven circular liquid chromatography, however it can be used to integrate the channel-free injection part with the separation system. Because this setup can provide higher rotation frequency, the fluorescent particles were studied to verify the influence of centrifugal force was insignificant. Furthermore, FFT was used to extract frequency information from periodic signals in our rotating microfluidic system. The other setup has superior rotation stability in keeping the glass surface smooth and keeping the rotation frequency constant. Therefore it was chosen to carry out chromatography experiment. The thickness of the liquid film was measured to ensure that the scale was in the μm range and the microfluidic properties were applicable. After the preliminary experiment with fluorophore solutions to check the feasibility of chromatography application, channel-free shear driven circular liquid chromatography was validated. The C18 stationary phase coating was optimized with adequate stability and superior roughness and thickness. Magnetic powders were also utilized for C18 coating. With the optimized rotation frequency and sample concentrations, two model fluorophores rhodamine B and fluorescein were successfully separated. The separation efficiency was proved to increase with cycles, with the increasing theoretical plate numbers, decreasing HETP, and increasing separation factors. The resonance energy transfer effect accompanied with the separation of rhodamine B and fluorescein was studied and the FFT analysis was investigated in details as well. Fluorescein and coumarin 307 were separated as another example to validate SDCC.

After validation of SDCC, the diffusion coefficient of rhodamine B was measured as an example to explain the fast extinction of fluorescent signals after a certain time period. The fast dispersion of sample molecules restricted the application of channel-free system.

At last, an automated channel-free injection system was integrated to the separation system. In order to eliminate the remixing of samples during rotation, the injection reservoir was designed to be 14 mm away from the separation track. Fluorescein solution was successfully transported to the separation track. Although

the reproducibility needs to be improved, the injection system demonstrates a promising prospect in integrating automated injection and detection units with the SDCC system.

6.2 Outlook

Since SDCC is used as a separation platform in μ-TAS, the future SDCC device should be fabricated with smaller size and be able to accomplish analytical tasks with reliable precision.

Firstly a more stable rotating microfluidic system is considered to improve the reproducibility. The magnetic levitation principle can help to build a new rotating system, which provides circular shear force between two magnets by rotating the floating magnet. A number of commercial products have been manufactured with magnetic levitation system, such as the floating train and floating bed. This kind of system is assumed to have more flexibility with reliable stability.

As shown in figure 6.1, the rotation glass plate can be fixed with the floating ring magnet and the stationary glass plate is laid underneath. The repulsing force produced by the ring magnetic dipoles and the weight of the rotatory system will reach balance. This balance holds the upper part floating above the stationary stage, and keeps the distance of the space a constant. The distance can be tuned by changing the strength of magnetic field or the weight of the rotatory part. The magnets always tend to align their axes to be parallel with the magnetic field.

This setup gives more flexibility for the liquid thickness between two glass plates. Meanwhile, the floating system will not damage the glass surface even if the glass plates are not strictly parallel. But in the X- and Y- axes, once the position is fixed according to the layout of the magnetic dipoles, it is hard to move. This stability relies on the nature of magnets.

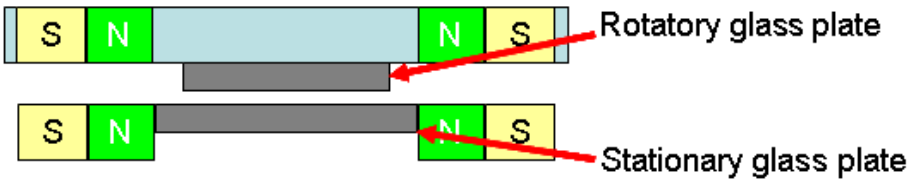

Figure 6.1: Illustration of magnetic levitation setup for shear driven circular rotating functions, two ring magnets are aligned to provide the rotating space. The rotation frequency can reach extremely high and the thickness of the mobile phase film can be decided by the strength of the magnetic field.

There are many possibilities to introduce rotation motion. With the setup shown in figure 6.1, a mechanical rotatory motor can be attached with the floating glass plate. Applying a two-phase or three-phase rotating magnetic field like in magnetic motors[1] can also provide rotation with high frequencies. Because the friction is small in magnetic levitation system, the rotation motion will be smooth and stable.

As for SDCC performance, some promising improvements are supposed to enhance the separation efficiency, such as reducing the thickness of both mobile phase and stationary phase, operating in a particle-free environment, and introducing transverse optics which can provide a long detection path across the miniature liquid film.

When the stationary phase coating is improved with reliable reproducibility, the isotherm which is the adsorption equilibrium of the stationary phase under certain temperature can be investigated. Isotherm represents the correlation of the absorption conditions of the stationary phase with different mobile phase concentrations[106]. As a standard to characterize the thermodynamics in stationary phase, isotherm reflects the effective internal surface areas of the stationary phase, which is normally expressed by the total adsorbent load volume.

[1] http://www.tpub.com/neets/book5/18a.htm

In the future work, the separated analytes is considered to be led to flow out of the SDCC separation platform and collected for further detection and usage. A collection system is placed with a certain distance away from the separation track. The separated analytes are transported to the collection position by the cover glass plate. Then the mobile phase is injected to flush the analytes out, as illustrated in figure 6.2.

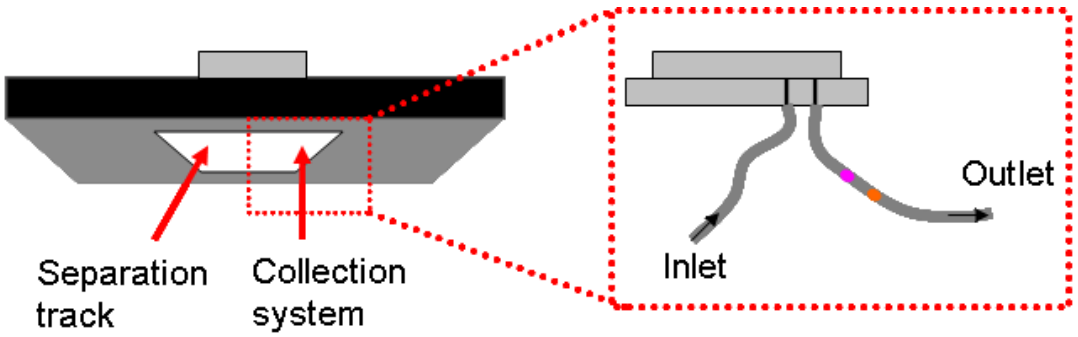

Figure 6.2: Illustration of collection system integrated with separation system for future SDCC applications. After the analytes are separated, they can be transported to the collection track and led out by pressure.

With the collection system integrated, SDCC method could broaden its applications.

Lastly, for the channel-free injection, the technique of "micro-plasma writing" can be used to define the flow track and direct the microfluidic flow. This technique changes demanded parts of hydrophobic surface into hydrophilic with a dielectric barrier discharge microplasma jet. The silanized glass surface is activated by the microplasma jet like "writing on a paper" to form hydrophilic microchannels. Here, hydrophobic boundaries provide so called "virtual walls" for surface-directed capillary flow. The results are shown in figure 6.3 (A)[107]. Another kind of surface directed flow method firstly reported in gas-liquid system[108] (figure 6.3 (B)) can be applied in liquid-liquid system, because the aqueous flow can be confined to the hydrophilic pathways and other organic sheath flows can be directed in the

hydrophobic pathway. The channel wall is established between hydrophilic surface and hydrophobic surface. The channel-free method can be simplified by means of surface fabrication.

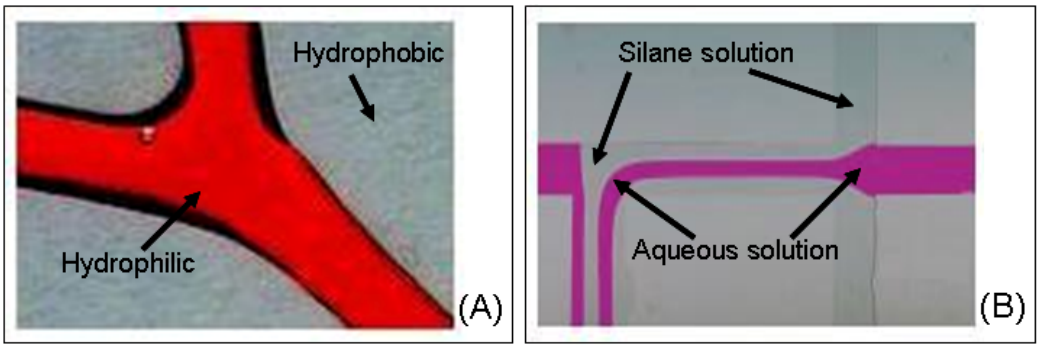

Figure 6.3: Ways to define microfluidic flow for potential channel-free injection method by utilizing the (A) surface modification[107] and (B) immiscible properties[108] of the flows.

By successfully integrating channel-free injection and automated analytes collection steps, the application of SDCC in chemical industries, clinical diagnosis, pharmaceutical separations, and other high efficiency separations in life sciences can be appreciated.

APPENDIX A: ADDITIONAL INFORMATION ON MICRO-FLUIDIC ROTATING SYSTEM

A.1 WLI Measurement

Two setups have been designed and built for micro-fluidic rotating purpose. Since the upper glass plate was fixed by vacuum with rotatory motor in design A, the upper glass plate was not strictly parallel to the bottom stationary glass plate. After rotating for 5 minutes, the depth of scratch was measured by WLI and shown in figure A.1. Scratch edge with a depth of more than 1 μm demonstrates the fierce friction. This observation helps to choose design B for the SDCC experiment.

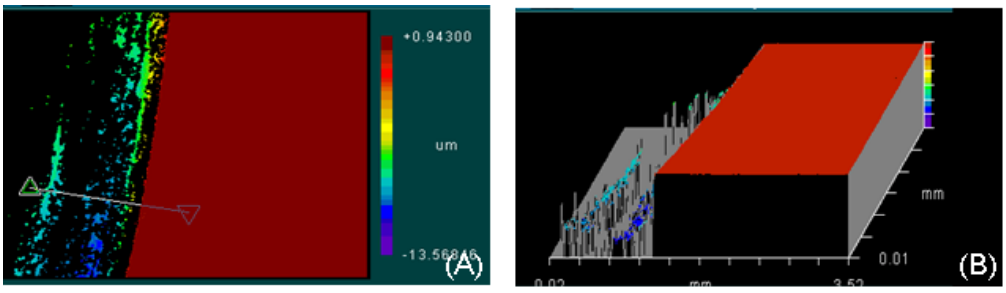

Figure A.1: WLI pictures of uncoated glass surface after rotating for 5 minutes with design A. The scratch is deeper than 20 μm.

A.2 Structure Drawings of Two Designs

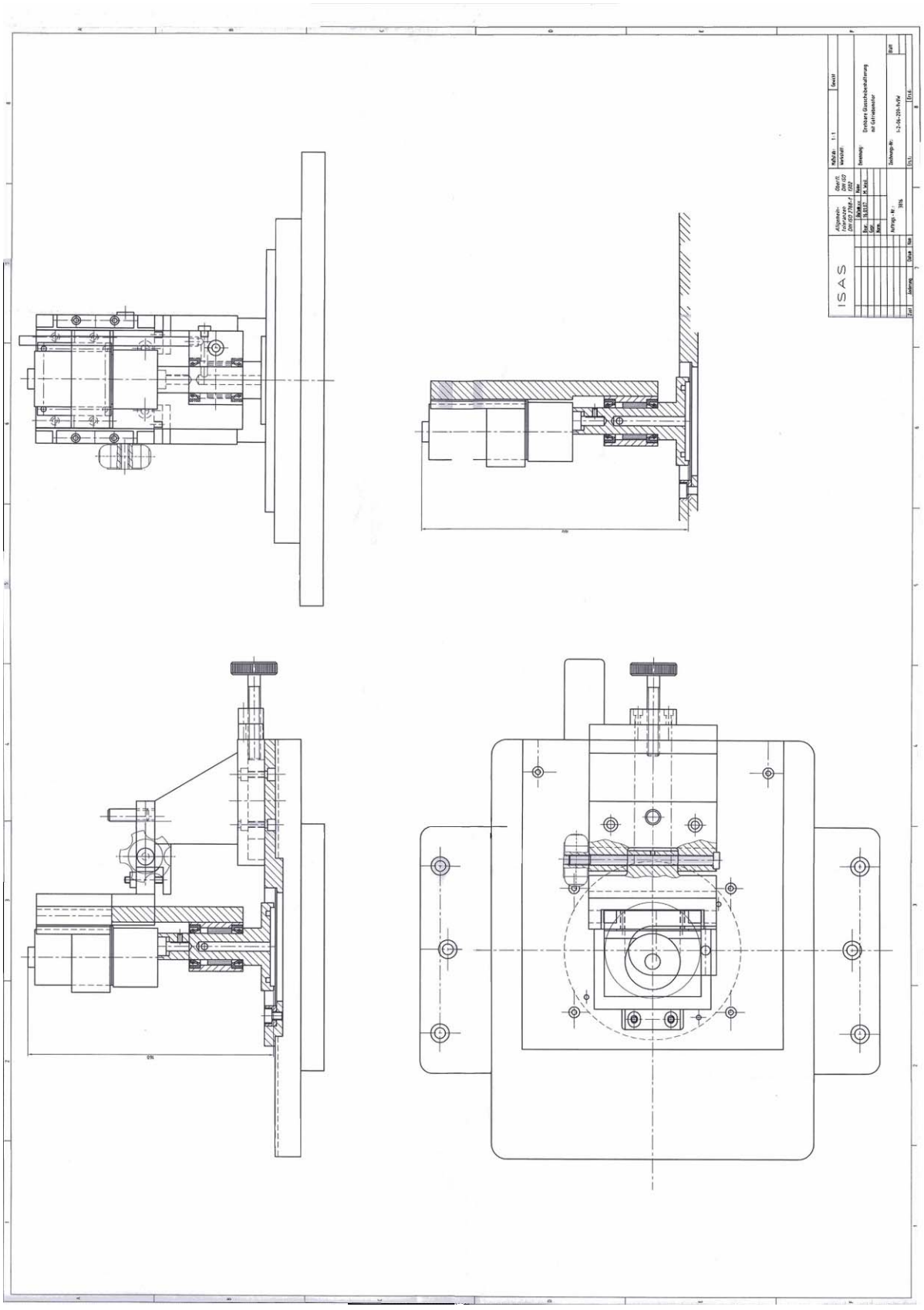

Figure A.2: Drawing of design A with a homemade rotor.

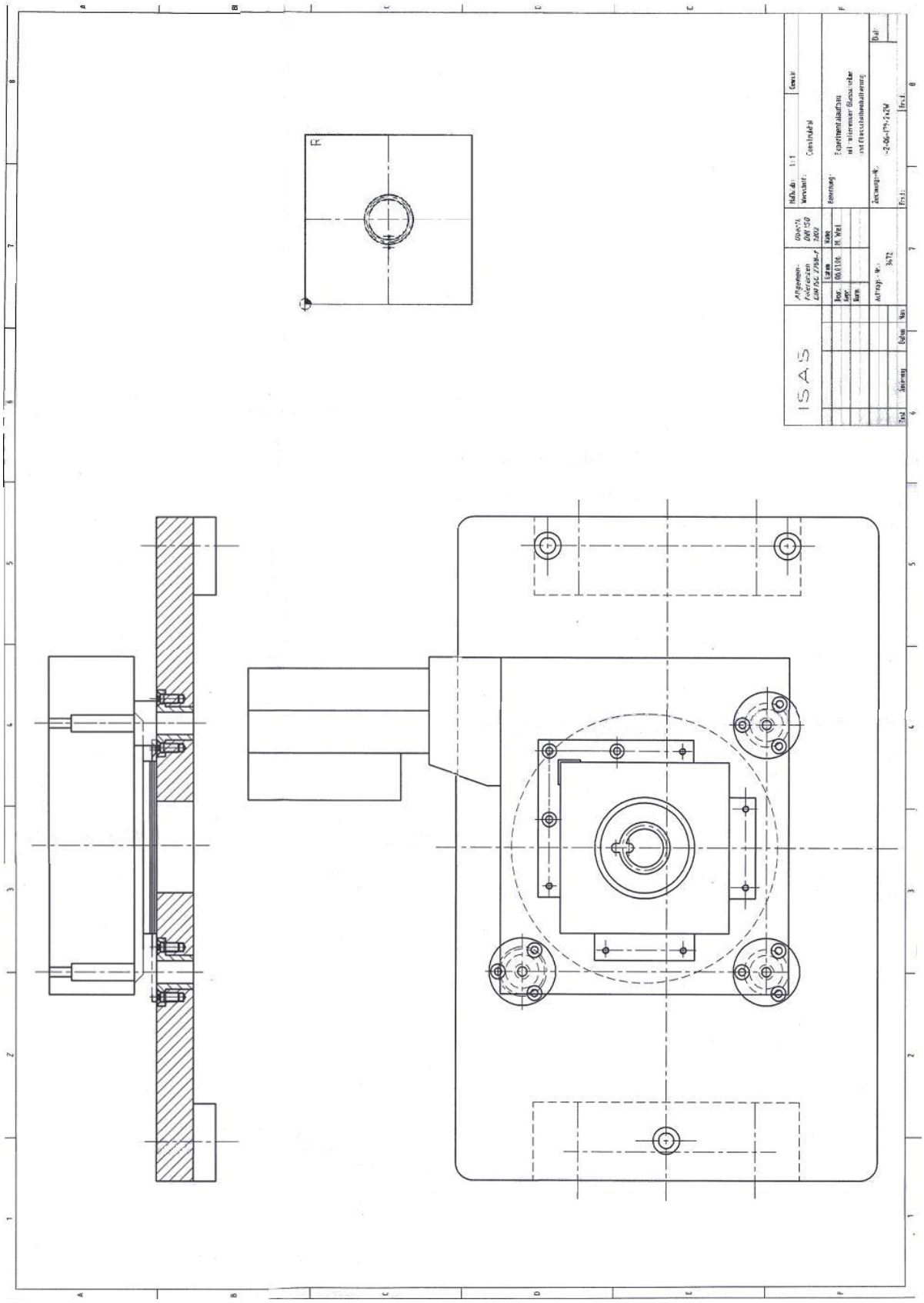

Figure A.3: Drawing of design B with a PI stepping motor.

A.3 Oil-water System

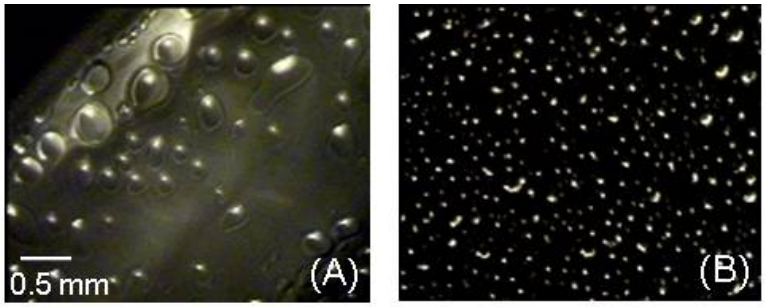

Figure A.4: Oil-water phases after rotation, (A) glass surface without coating and (B) glass surface modified with dimethyl-dichlorsilane ($(CH_3)_2SiCl_2$, Merck, Germany). The oil droplets distribute in the water phase evenly.

Immiscible phases such as oil and water were examined under rotating shear force in our system. Rotating shear force drove the droplet to disperse. The droplet shape and size on different surfaces were compared in figure A.4. Uncoated glass surface had low surface tension, and the size of oil droplets in water was big. The oil droplets were much smaller with surface coated with dimethyl-dichlorsilane due to high surface tension.

APPENDIX B: ADDITIONAL INFORMATION ON SHEAR DRIVEN CIRCULAR LIQUID CHROMATOGRAPHY

B.1 Contact Angle Measurements

Table B.1 compares the contact angles by treating with different immersion methods for different durations of time. Table B.2 shows the contact angle changes when the glass surface was treated with vapor deposition method. From table B.1, we can see the time of immersion does not largely affect the surface properties, which indicates that the siloxane linkage takes place immediately with fresh prepared soda lime glass and the standard deviation (SD) are acceptable ($\leqslant$ 2%).

Table B.1: Contact angles of glass plates treated with different immersion methods for different time durations, three places are randomly chosen and each glass plate sample is measured twice.

			Contact angles (º)						Average (º)	SD
Fresh made	a[1]	Left	113.03	115.45	115.57	117.62	117.52	115.46	113.59	0.94%
		Right	112.28	111.26	113.24	109.75	112.24	109.60		
		Average	112.66	113.36	114.41	113.69	114.88	112.53		
	b	Left	108.84	110.70	111.32	113.22	113.15	114.43	110.72	1.17%
		Right	108.86	110.52	110.30	107.80	108.82	110.62		
		Average	108.85	110.61	110.81	110.51	110.99	112.53		
	c	Left	111.75	115.81	116.34	116.30	114.54	114.89	113.20	1.23%
		Right	112.49	113.45	110.55	112.97	110.26	108.99		
		Average	112.12	114.63	113.45	114.64	112.40	111.94		
	d	Left	106.93	104.81	106.71	108.92	106.36	103.79	107.53	1.35%
		Right	108.45	110.79	106.88	110.80	108.11	107.86		
		Average	107.69	107.8	106.80	109.86	107.24	105.83		
After 24 h	a	Left	109.92	109.78	109.15	108.85	112.76	110.80	109.32	1.60%
		Right	111.31	112.23	107.47	105.47	108.35	105.70		
		Average	110.62	111.01	108.31	107.16	110.56	108.25		
	b	Left	105.74	108.73	107.64	112.42	115.49	111.34	107.92	2.30%
		Right	104.83	105.57	105.74	103.93	108.66	104.93		
		Average	105.29	107.15	106.69	108.18	112.08	108.14		
	c	Left	116.71	118.96	115.64	116.77	118.60	116.22	114.46	0.99%
		Right	111.08	111.93	111.48	111.84	113.23	111.02		
		Average	113.90	115.45	113.56	114.31	115.92	113.62		
	d	Left	105.91	104.30	104.87	105.52	105.93	106.25	105.91	3.25%
		Right	103.24	103.36	101.69	102.04	116.09	111.68		
		Average	104.58	103.83	103.28	103.78	111.01	108.97		

[1]**a**. 1 s in C18 solution and 10 s in pure toluene.

b. 10 s in C18 solution and 10 s in pure toluene.

c. 1 h in C18 solution and 10 s in pure toluene.

d. 1 h in C18 solution and dilute with pure toluene, avoid contact of air.

Table B.2: Contact angles of vapor deposition methods. The contact angles decrease from 100° to 60°, which means the coating is unstable.

		Contact angles (°)						Average (°)	SD
Fresh made	Left	119.40	100.58	89.93	120.87	115.62	120.43	108.32	11.85%
	Right	113.86	98.86	86.56	111.50	107.96	114.32		
	Average	116.63	99.72	88.25	116.19	111.79	117.38		
	Left	104.23	101.32	96.52	103.98	100.89	87.45	97.79	5.92%
	Right	100.45	98.78	90.13	104.86	95.22	89.67		
	Average	102.34	100.05	93.33	104.42	98.06	88.56		
After 24 h	Left	58.49	61.11	62.09	48.93	48.21	47.25	52.78	2.48%
	Right	46.98	50.41	49.67	54.68	52.53	53.27		
	Average	52.74	55.61	55.88	51.81	50.37	50.26		
	Left	63.49	62.58	64.68	58.79	61.04	60.62	60.49	0.51%
	Right	56.93	59.77	56.66	60.64	60.61	60.02		
	Average	60.21	61.18	60.67	59.72	60.83	60.32		

B.2 Program in PICO

Here only those commands used in experiment are chronologically listed below.

When the stepping motor fits precisely with the bottom glass plate in special position, **DH** was used at first to define the current motor position as the zero position (home position). This is very important because the position of motor should be precisely defined to meet the construction of the setup. Then the following rotation step started. **SV n** ($0 < n < 65{,}535$) was used to set velocity to n counts per second. **MR n** ($-1{,}073{,}741{,}823 < n < 1{,}073{,}741{,}823$) meant to move (rotate) the stepping motor to a certain position. At last, **GH** was to move the motor back to the defined home position for the next experiment.

The command SV 50000 was measured to be 0.114 Hz and the value of SV was proportional to frequency.

B.3 Chromatographic Performance

Table B.3: Theoretical plate numbers *N* and HETP *H* values of rhodamine B and fluorescein. The base width of the peaks is 10163 ms for both rhodamine B and fluorescein after normalization.

rhodamine B	i	**1**	**2**	**3**	**4**	**5**	**6**	**7**
	t_R (ms)	37896.96	55099.97	72479.59	90110.76	107410	124670	142540
	H_i(μm)	2286.56	1922.94	1736.43	1617.70	1549.73	1502.47	1454.66
	N_i	74	118	163	210	255	301	350
	i	**8**	**9**	**10**	**11**	**12**	**13**	**14**
	t_R (s)	159840	177770	195070	212290	230220	247580	265520
	H_i(μm)	1428.17	1397.07	1380.8	1368.29	1349.33	1339.37	1324.97
	N_i	396	445	491	537	586	633	683
	i	**15**	**16**	**17**	**18**	**19**	**20**	
	t_R (ms)	282880	300820	318190	336140	353510	371470	
	H_i(μm)	1317.78	1306.41	1301.02	1291.72	1287.61	1279.82	
	N_i	729	779	825	875	922	972	
fluorescein	i	**1**	**2**	**3**	**4**	**5**	**6**	**7**
	t_R (ms)	44491.55	62088.41	80037.94	97522.14	115430	132820	150780
	H_i(μm)	1658.96	1514.43	1423.96	1381.16	1341.86	1323.74	1300.01
	N_i	102	149	198	246	295	342	391
	i	**8**	**9**	**10**	**11**	**12**	**13**	**14**
	t_R (ms)	168170	186140	203440	220770	238760	256120	274100
	H_i(μm)	1290.19	1274.25	1269.52	1265.19	1254.53	1251.54	1243.29
	N_i	438	488	534	581	63	677	727
	i	**15**	**16**	**17**	**18**	**19**	**20**	
	t_R (ms)	291470	309440	326820	344800	362170	380140	
	H_i(μm)	1241.25	1234.64	1233.22	1227.65	1226.77	1222.10	
	N_i	774	824	871	921	968	1017	

The changes of Δt_R and α are plotted in table B.4. In 20 cycles, the Δt_R increases from 6600 ms to 8670 ms. But the α value decreases from 1.17 to 1.03 because the stationary phase is dropping off when the mobile phase flows and flushes.

Table B.4: Separation factor α and time interval Δt_R with rotation cycles for both rhodamine B and fluorescein, which are calculated from the peaks silmulated in figure 4.19.

i	**1**	**2**	**3**	**4**	**5**	**6**	**7**
t_{R1} (ms)	37896.96	55099.97	72479.59	90110.76	107410	124670	142540
t_{R2} (ms)	44491.55	62088.41	80037.94	97522.14	115430	132820	150780
Δt_R(ms)	6595	6988	7558	7411	8020	8150	8240
α	1.174	1.127	1.104	1.082	1.075	1.065	1.058
i	**8**	**9**	**10**	**11**	**12**	**13**	**14**
t_{R1} (ms)	159840	177770	195070	212290	230220	247580	265520
t_{R2} (ms)	168170	186140	203440	220770	238760	256120	274100
Δt_R(ms)	8330	8370	8370	8480	8540	8540	8580
α	1.052	1.047	1.043	1.040	1.037	1.034	1.032
i	**15**	**16**	**17**	**18**	**19**	**20**	
t_{R1} (ms)	282880	300820	318190	336140	353510	371470	
t_{R2} (ms)	291470	309440	326820	344800	362170	380140	
Δt_R(ms)	8590	8620	8630	8660	8660	8670	
α	1.030	1.029	1.027	1.026	1.024	1.023	

B.4 Program in MATLAB

```
x = data(:,1);        [import x axis]

y = data (;,2);       [import y axis]

plot (y);        [draw intensity graph against time]

Y = fft(y);        [fast Fourier transform]

n = length(Y);        [calculate data points]

power = abs(Y(1:n/2)).^2;        [take the real part of fast Fourier transform]

nyquist = 5;        [Nyquist is half of the sampling frequency, so if your sampling
 frequency is 10 (10 samples per second), the Nyquist should equal to 5.]

freq = (1:n/2)/(n/2)*nyquist;        [define the frequency scale]
```

plot (freq,power); *[draw FFT graph]*

end;

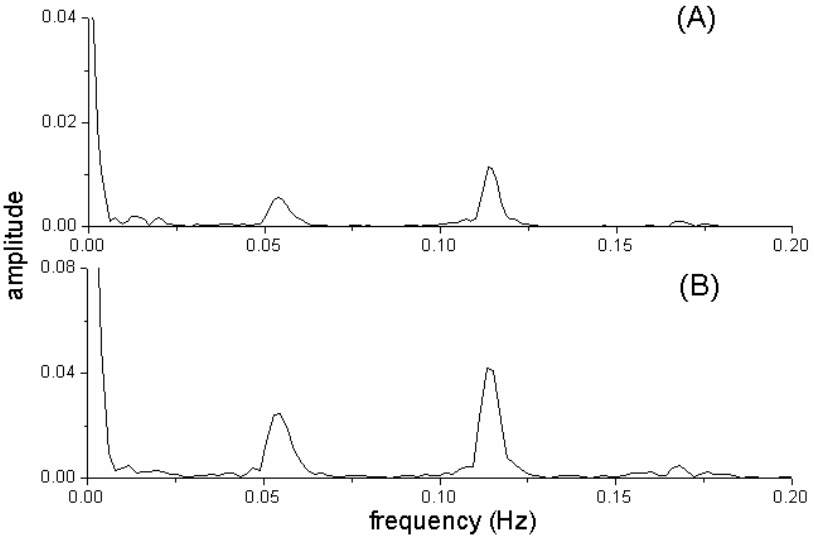

Figure B.1: FFT comparison for different time intervals, (A) every 0.2 s and (B) every 2 s. the resolution is better with shorter time period.

According to the discrete wavelet function used in Fourier transform, H (=$\{h_k\}$) and G (=$\{g_k\}$) are low-pass filter and high-pass filter, which are called wavelet filter coefficients. The relationship between h_k and g_k is shown in equation B.1. They helped to define the smoothed coefficients $C^{(j)}$ and the differential coefficients $D^{(j)}$ as shown in equation B.2 and equation B.3[1].

$$g_k = (-1)^k h_{1-k}; \sum_k h_k = 1; \sum_k g_k = 0 \qquad \text{(B.1)}$$

$$C^{(j)} = \sqrt{2} \cdot \sum_n (C_n^{j-1} h_{n-2k}) \qquad \text{(B.2)}$$

$$D^{(j)} = \sqrt{2} \cdot \sum_n (C_n^{j-1} g_{n-2k}) \qquad \text{(B.3)}$$

When H and G are applied to *C(0)* of finite length N, *C(1)* and *D(1)* at level 1

[1] http://www.eso.org/sci/data-processing/software/esomidas//doc/user/98NOV/volb/node322.html

can be generated and the vector *C(1)* is generated with length of *N*/2. This process can be applied repeatedly until the request resolution is obtained. This implies an interesting phenomenon that the longer collecting time interval between two points will give better resolution for FFT analysis using wavelet function, which is shown in figure B.1. The intensity of both mobile phase frequency and rotation frequency were increased with longer time interval for data collection. And the S/N ratio increased since the small peaks between 0 Hz and 0.05 Hz were reduced as shown in figure B.1 (B). But according to the FFT basic rule, the sample collection frequency should be at least twice the maximum frequency in the continuous signal[2]. The sampling frequency limit is called Nyquist frequency.

B.5 Diffusion Coefficient

The peak information was studied for rhodamine B dye when rotated at 0.114 Hz with our channel-free SDCC system.

The peaks intensity is plotted versus time in figure B.2 (A) with the rotation frequency at 0.114 Hz. Due to the dispersion of sample molecules out of the track, the sample concentration decreases to lower than the detection limit of PMT. The peaks height decrease and at last disappear. The peaks are centered on the temporal position of the peak maximum in figure B.2 (B). In general, the peaks represent the fluorescent band which flows over the microscope objective. The distribution of sample molecules defines the band width and shape.

[2] http://en.wikipedia.org/wiki/Nyquist_frequency

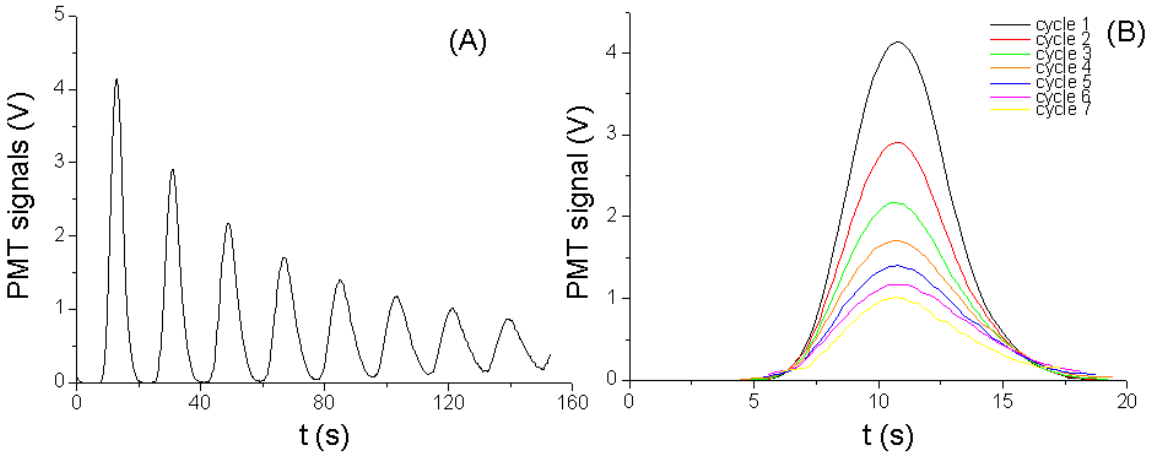

Figure B.2: Peak shapes for rhodamine B when rotated with 0.114 Hz. (A) peaks broadening with time and (B) centered with maximum peak intensity.

Peak area and intensity decrease rapidly with time in figure B.2 (A). The first seven cycles are chosen to be centralized in figure B.2 (B). After the 7th cycle, the shape of the peak is too poor to be analyzed. The details are listed in table B.5.

Table B.5: Peak information from figure B.2 (acquired by Origin 7.0).

cycles / characters	1	2	3	4	5	6	7	8
Peak maximum at (s)	10.8	28.8	46.8	64.8	83	101.4	119.2	137.2
Peak width (s)	4.6	5.2	6.2	6.8	7.8	8.4	9.2	10.2
Peak height (V)	4.138	2.913	2.169	1.71	1.401	1.175	1.016	0.876
Peak area	20.14	16.41	14.22	12.61	11.43	10.52	9.96	9.39

APPENDIX C: ADDITIONAL INFORMATION ON INJECTION DEVICE

C.1 CCD Images of Injection and Rotation Process

2 μL of 5 mM fluorescein sodium salt in water solution was injected and the fluorescence information was recorded by CCD camera when rotation step began. The frequency of rotatory motor was 1.41 Hz. The images are shown in figure C.1. When the fluorescein was injected and moved to the objective (figure C.1 (A)), it took about 0.45 s before the fluorescence disappeared. Starting from the second cycle (figure C.1 (B)), the fluorescent intensity decreased (at 0.47 s, 1.14 s, 1.46 s, 1.76 s, and 2.03 s), and the duration of fluorescence that can be observed in each cycle also decreased with time, from 0.21 s (figure C.1 (B)) to 0.12 s in the fifth cycle (figure C.1 (E)). This indicates the dispersion of sample molecules with rotations.

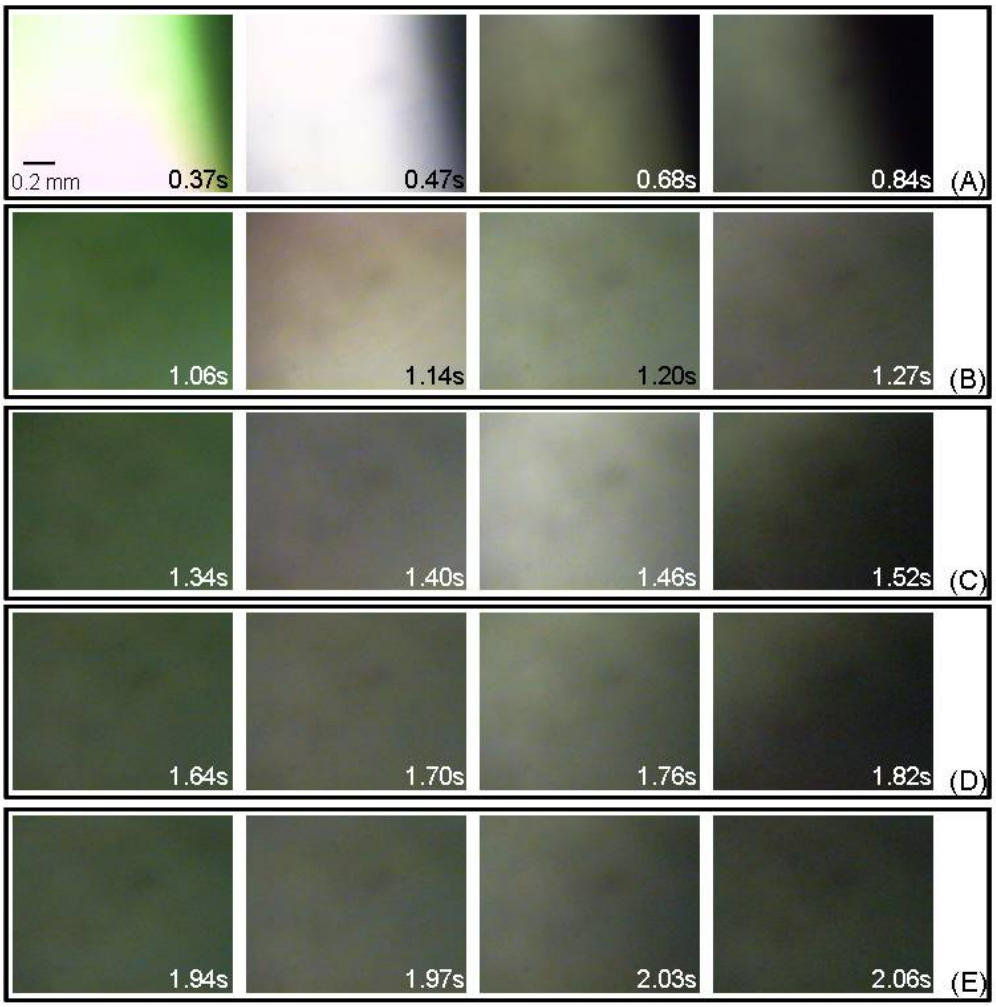

Figure C.1: Images of fluorescein rotating at 1.41 Hz after injected with channel-free method. The rotatory motor rotates clockwise. Images are sorted chronologically from (A) the first cycle to (E) the fifth cycle. The sample molecules disperse with cycles.

TABLE OF ABBREVIATIONS

CE	Capillary Electrophoresis
DFT	Discrete Fourier Transform
FFT	Fast Fourier Transform
FRET	Fluorescence Resonance Energy Transfer
GC	Gas Chromatography
HETP	Height Equivalent to a Theoretical Plate
HPLC	High Performance Liquid Chromatography
ISAS	Institute for Analytical Sciences
LC	Liquid Chromatography
LIGA	Lithographie Galvanoformung Abformung
MEMS	Micro-Electro-Mechanical System
μ-TAS	Miniaturized Total Analysis Systems
ODS	Octadecylsilane
PCR	Polymerase Chain Reaction
PDMS	Polydimethylsiloxane
PMMA	Polymethylmethacrylate
PMT	Photomultiplier Tube
RET	Resonance Energy Transfer
RPLC	Reversed Phase Liquid Chromatography
SCCE	Synchronized Cyclic Capillary Electrophoresis
SCOFT	Shah Convolution Fourier Transform
SD	Standard Deviation
SDC	Shear Driven Chromatography
SDCC	Shear Driven Circular Chromatography
TLC	Thin Layer Chromatography
UTLC	Ultrathin Layer Chromatography
WLI	White Light Interferometry

BIBLIOGRAPHY

[1] A. Manz, N. Graber, H. M. Widmer, (**1990)**. Miniaturized Total Chemicalanalysis Systems – a novel concept for chemical sensing. *Sens Actuators B,* **B1:** 244.

[2] H. Poppe, **(1997)**. Some Reflections on Speed and Efficiency of Modern Chromatographic Methods, *J. Chromatogr. A.,* **778:** 3.

[3] G. Desmet, G. V. Baron, **(1999)**. On the Possibility of Shear-driven Chromatography: a Theoretical Performance Analysis, *J. Chromatogr. A.,* **855:** 57.

[4] V. J. Coates, H. J. Noebels, I. S. Fagerson, (**1958).** Gas Chromatography, pp. 237-247. Academic Press Inc., New York.

[5] J. C. T. Eijkel, A. van den Berg, A. Manz, **(2004)**. Cyclic Electrophoretic and Chromatographic Separation Methods, *Electrophoresis,* **25:** 243.

[6] P. S. Dittrich, A. Manz, **(2006)**. Lab-on-a-chip: microfluidics in drug discovery, *Nature,* **5:** 210.

[7] T. Vilkner, D. Janasek, A. Manz, (**2004).** Micro Total Analysis Systems. Recent Developments, *Anal. Chem.,* **76:** 3373.

[8] H. Yin, K. Killeen, **(2007)**. The Fundamental Aspects and Applications of Agilent HPLC-Chip, *J. Sep. Sci.,* **30:** 1427.

[9] G. S. Zhuang, J. Liu, C. P. Jia, Q. H. Jin, J. L. Zhao, H. M. Wang, **(2007)**. Microchip-based capillary electrophoresis for determination of lactate dehydrogenase isoenzymes. *J. Sep. Sci.,* **30:** 1350.

[10] M. S. Munson, G. Danger, J. G. Shackman, D. Ross, **(2007)**. Temperature Gradient Focusing with Field-Amplified Continuous Sample Injection for Dual-Stage Analyte Enrichment and Saperation, *Anal. Chem.,* **79:** 6201.

[11] D. Kohlheyer, J. C. T. Eljkel, S. Schlautmann, A. van den Berg, R. B. M. Schasfoort, **(2007)**. Microfluidic High-Resolution Free-Flow Isoelectric Focusing, *Anal. Chem.,* **79:** 8190.

[12] J. G. Shackman, M. S. Munson, D. Ross, **(2007)**. Gradient Elution Moving Boundary Electrophoresis for High-Throughput Multiplexed Microfluidic Devices, *Anal. Chem.,* **79:** 565.

[13] H. Yin, K. Killeen, R. Brennen, D. Sobek, **(2005)**. Microfluidic Chip for Peptide Analysis with an Integrated HPLC Column, Sample Enrichment Column, and Nanoelectrospray Tip, *Anal. Chem,.* **77:** 527.

[14] D. Janasek, J. Franzke, A. Manz, (**2006)**. Scaling and the design of miniaturized chemical-analysis systems, *Nature,* **42:** 374.

[15] S. C. Terry, G. H. Jerman, J. B. Angell, **(1979)**. A gas chromatographic air analyzer fabricated on silicon wafer using integrated circuit technology. *IEEE Trans. Electron Devices*, **12 (ED-26):** 1880.

[16] A. de Mello, **(2002)**. Plastic fantastic? *Lab Chip.*, **2:** 31N

[17] J. N. Lee, C. Park, G. M. Whitesides, **(2003)**. Compatibility of Poly(dimethylsiloxane)-Based Microfluidic Devices, *Anal Chem.,* **75:** 6544.

[18] N. Xia, G. M. Whitesides, **(1998)**. Soft lithography, *Ann. Rev. Mater. Sci.,* **28:** 153.

[19] Y G. M. Whitesides, B. Grzybowski, **(2002)**. Self-Assembly at All Scales, *Science,* **295(5524):** 2418.

[20] K. S. V. Mohan, M. Abhijit, G. Animangsu, **(2006)**. Embedded Template-Assisted Fabrication of Complex Microchannels in PDMS and Design of a Microfluidic Adhesive, *Langmuir*, **22:** 10291.

[21] A. W. Martinez, S. T. Phillips, B. J. Wiley, M. Gupta, G. M. Whitesides, **(2008)**. FLASH: A rapid method for prototyping paper-based microfluidic devices, *Lab Chip.,* **8:** 2146.

[22] G. Karniadakis, A. Beskok, N. Aluru, **(2005)**. Shear-Driven Flows. In: Microflows and Nanoflows, pp. 79-112. Springer Science+Business Media, Inc.

[23] Steffen Hardt, Friedhelm Schoenfeld, **(2007)**. Microfluidics: Fundamentals and Engineering Concepts. In: Microfluidic Technologies for Miniaturized

Analysis Systems, pp. 2-49. Springer Science+Business Media, Inc.

[24] G. T. A. Kovacs, **(1998)**. Micromachined Transducers Sourcebook. WCB/McGraw-Hill, Boston.

[25] A. Fick, **(1855)**. On Liquid Diffusion, *Phil. Mag.,* **10:** 30.

[26] M. Madou, J. Zoval, G. Jia, H. Kido, J. Kim, N. Kim, **(2006)**. Lab on a CD, *Annu. Rev. Biomed. Eng.,* **8:** 601.

[27] G. T. Kovacs, **(1998)**. Microfluidic devices. In: Micromachined Transducers Sourcebook, pp.781-193. WCB/McGraw-Hill, Boston.

[28] G. Ekstrand, C. Holmquist, A. E. Oerlefors, B. Hellman, A. Larsson, P. Anderson, **(2000)**. Microfluidics in a rotating CD. In: Micro Total Analysis Systems 2000, pp. 311-314. Kluwer Acad. Dordrecht.

[29] J. Ducrée, S. Haeberle, S. Lutz, S. Pausch, F. von Stetten, R. Zengerle, **(2007)**. The centrifugal microfluidic Bio-Disk platform, *J. Micromech. Microeng.,* **17:** S103.

[30] I. H. A. Badr, R. D. Johnson, M. J. Madou, L. G. Bachas, **(2002)**. Fluorescent Ion-Selective Optode Membranes Incorporated onto a Centrifugal Microfluidics Platform, *Anal. Chem.,* **74:** 5569.

[31] H. Wu, T. W. Odom, D. T. Chiu, G. M. Whitesides, **(2003)**. Fabrication of Complex Three-dimensional Microchannel Systems in PDMS, *J. Am. Chem. Soc.,* **125:** 554.

[32] J. H**.** Lee, J. B. Ha, Y. K. Bahk, S. H. Yoon, T. Arakawa, J. S. Ko, B. S. Shin, S. Shoji, J. S. Go, **(2008)**. Microfluidic centrifuge of nano-particles using rotating flow in a microchamber, *Sensors and Actuators B,* **132:** 525.

[33] G. Karniadakis, A. Beskok, N. Aluru, **(2005)**. Governing Equations and Slip Models. In: Microflows and Nanoflows, pp. 51-74. Springer Science+Business Media, Inc.

[34] J. H. Xu, G. S. Luo, S. W. Li, G. G. Chen, **(2006)**. Shear force induced monodisperse droplet formation in a microfluidic device by controlling wetting properties, *Lab Chip.,* **6 (1):** 131.

[35] J. Tan, J. H. Xu, S. W. Li, G. S. Luo, **(2008)**. Drop dispenser in a cross-junction microfluidic device: Scaling and mechanism of break-up, *Chem.*

Eng. J., **136 (2-3):** 306.

[36] M. Rauscher, S. Dietrich, J. Koplik, **(2007)**. Shear Flow Pumping in Open Micro- and Nanofluidic Systems, *Phys. Rev. Lett.,* **98:** 224504-1.

[37] H. Lu, L. Y. Koo, W. M. Wang, D. A. Lauffenburger, L. G. Griffith, K. F. Jensen, **(2004)**. Microfluidic shear devices for quantitative analysis of cell adhesion. *Anal. Chem.,* **76 (18):** 5257.

[38] D. M. Hallow, R. A. Seeger, P. P. Kamaev, G. R. Prado, M. C Laplaca, M. R. Prausnitz, **(2008)**. Shear-Induced Intracellular Loading of Cells With Molecules by Controlled Microfluidics. *Biotechnol. Bioeng.,* **99 (4):** 846.

[39] L. S. Ettre, **(1993)**. Nomenclature for Chromatography, *Pure and Appl, Chem.,* **65(4):** 819.

[40] J. C. Kraak, **(1997)**. Prospects of Miniaturized Separation Systems, *Pure and Applied Chemistry,* **69:** 157.

[41] R. Swart, J. C. Kraak, H. Poppe, **(1995)**. Performance of an ethoxyethylacrylate stationary phase for open-tubular liquid chromatography, *J. Chromatogr. A,* **689:** 177.

[42] G. L. Gauthier, R. Grimm, **(2006)**. Miniaturization**:** Chip-based Liquid Chromatography and Proteomics, *Drug Discovery Today: Technologies,* **2(1):** 59.

[43] M. H. Fortier, E. Bonneil, P. Goodley, P. Thibault. **(2005)**. Integrated Microfluidic device for Mass Spectrometry-based Proteomics and its Application to biomarker Discovery Programs, *Anal. Chem.,* **77:** 1631.

[44] M. Niñonuevo, H. An, H. Yin, K. Killeen, R. Grimm, R. Ward, B. German, C. Lebrilla, **(2005)**. Nanoliquid Chromatography-Mass Spectrometry of Oligosaccharides Employing Graphitized Carbon Chromatography on Microchip with a High-Accuracy Mass Analyzer, *Electrophoresis,* **26:** 3641.

[45] M. Vollmer, P. Hörth, G. Rozing, Y. Couté, R. Grimm, D. Hochstrasser, J. C. Sanchez, **(2006)**. Multi-dimensional HPLC/MS of the Nucleolar Proteome using HPLC-chip/MS. *J. Sep. Sci.,* **29:** 499.

[46] N. Burggraf, A. Manz, E. Verpoorte, C. S. Effenhauser, H. M. Widmer, N. F. de Rooij, **(1994)**. A novel approach to ion separations in solution: synchronized cyclic capillary electrophoresis (SCCE), *Sensors and Actuators B,* **20:** 103.

[47] F. von Heeren, E. Verpoorte, A. Manz, W. Thormann, **(1996)**. Micellar Electrokinetic Chromatography Separations and Analyses of Biological Samples on a Cyclic Planar Microstructure, *Anal. Chem.,* **68:** 2044.

[48] J. G. Choi, M. Kim, R. Dadoo, R. N. Zare, **(2001)**. Electrophoretron: a new method for enhancing resolution in electrokinetic separations, *J. Chromatogr. A.,* **924:** 53.

[49] A. Manz, L. Bousse, A. Chow, **(2001)**. Synchronized Cyclic Capillary Electrophoresis using Channels Arranged in a Triangle and Low Voltages, *Fresenius J. Anal. Chem.,* **371:** 195.

[50] J. Zhao, J. Jorgenson, **(1999)**. Application of synchronous cyclic capillary electrophoresis: Isotopic and chiral separations, *J. Microcolumn Sep.,* **11:** 439.

[51] D. Clicq, K. Pappaert, S. Vankrunkelsven, N. Vervoort, G. V. Baron, G. Desmet **(1999)**. Shear-Driven Flow Approaches to LC and Macromolecular Separations, *Anal. Chem.,* **76(23):** 430 A.

[52] S. Vankrunkelsven, D. Clicq, D. Cabooter, W. D. Malsche, J.G.E. Gardeniers, G. Desmet, **(2006)**. Ultra-rapid separation of an angiotensin mixture in nanochannels using shear-driven chromatography, *J. Chromatogr. A,* **1102:** 96.

[53] V. Fekete, D. Clicq, W. D. Malsche, H. Gardeniers, G. Desmet, **(2007)**. State of the Art of Shear Driven Chromatography Advantages and Limitations, *J. Chromatogr. A,* **1149:** 2.

[54] X. Yang, G. Jenkins, J. Franzke, A. Manz, **(2005)**. Shear-driven pumping and Fourier transform detection for on chip circular chromatography applications, *Lab Chip*, **5(7):** 764.

[55] C. D. Chin, V. Linder, S. K. Sia, **(2007)**. Lab-on-a-chip devices for global health: past studies and future opportunities, *Lab Chip,* **7(9):** 1094.

[56] B. Huang, H. K. Wu, D. Bhaya, A. Grossman, S. Granier, B. K. Kobilka, R. N. Zareal, **(2007)**. Counting Low-copy number Proteins in a Single Cell, *Science,* **315(5808):** 81.

[57] Z. F. Chen, Y. H. Gao, R. G. Su, **(2003)**. Fabrication and characterization of poly(methyl methacrylate) microchannels by *in situ* polymerization with a novel metal template, *Elctrophoresis*, **24(18):** 3246.

[58] F. Xu, M. Jabasini, Y. Baba, **(2002)**. DNA separation by microchip electrophoresis using low-viscosity hydroxypropylmethylcellulose-50 solutions enhanced by polyhydroxy compounds, *Electrophoresis*, **23(20):** 3608.

[59] A. Röseler, E. H. Korte, **(1998).** Infrared ellipsometric analysis of organic film-on-substrate samples, *Thin Solid Films,* **313-314:** 708.

[60] K. Roodenko, M. Gensch, H. M. Heise, U. Schade, N. Esser, K. Hinrichs, **(2006)**. Influences of thick film inhomogeneities on the ellipsometric parameters, *Infrared Physics and Technology*, **49 (1-2):** 74.

[61] L. G. Puckett, E. Dikici, S. Lai, M. Madou, L. G. Bachas, S. Daunert, **(2004)**. Investigation into the applicability of the centrifugal microfluidics platform for the development of protein-ligand binding assays incorporating enhanced green fluorescent protein as a fluorescent reporter. *Anal. Chem.,* **76 (24):** 7263.

[62] X. Meng, R. Tao, Y. Wang, **(2008)**. Fractional Fourier domain analysis of cyclic multirate signal processing, *Science in China Series E: Technological Sciences,* **51(6):** 803.

[63] H. J. Crabtree, M. U. Kopp, A. Manz, **(1999)**. Shah convolution Fourier Transform Detection, *Anal. Chem.,* **71 (11):** 2130.

[64] Y. C. Kwok, A. Manz, **(2001)**. Shah Convolution Differentiation Fourier Transform for Rear Analysis in Microchip Capillary Electrophoresis, *J. Chromatogr. A.,***924(1-2):** 177.

[65] Y. C. Kwok, A. Manz, **(2001)**. Shah Convolution Fourier Transform Detection : Multiple-sample injection technique, *Electrophoresis*, **22(2):** 222.

[66] Y. C. Kwok, N. T. Jeffery, A. Manz, **(2001)**. Velocity Measurement of Particles Flowing in a Microfluidic Chip Using Shah Convolution Fourier Transform Detection. *Anal. Chem.,* **73(8):** 1748.

[67] F. R. Verdun, C. Giancaspro, A. G. Marshall, **(1988)**. Effects of Noise, Time-Domain Damping, Zero-Filling and the FFT Algorithm on the "Exact" Interpolation of Fast Fourier Transform Spectra, *Appl. Spectrosc.,* **42:** 715.

[68] S. Pennathur, D. K. Fygenson, **(2008)**. Improving Fluorescence Detection in Lab on Chip Devices, *Lab Chip,* **8(5):** 649.

[69] A. J. Berglund, K. Mchale, H. Mabuchi, **(2007)**. Feedback localization of freely diffusing fluorescent particles near the optical shot-noise limit, *Optics Letters,* **32(2):** 145.

[70] L. Shui, S. Pennathur, J. C. T. Eijkel, A. van den Berg, **(2008)**. Multiphase flow in lab on chip devices: A real tool for the future, *Lab Chip,* **8(7):** 1010.

[71] T. Kang, J. Han, K. S. Lee, **(2008)**. Concentration gradient generator using a convective–diffusive balance, *Lab Chip,* **8(7):** 1220.

[72] T. T. Huang, D. G. Taylor, S. L. Kwan, M.Sedlak, R. Bashir, N. S. Mosier, M. R. Ladisch, **(2006)**. Surface-directed boundary flow in microfluidic channels, *Langmuir,* **22(14):** 6429.

[73] X. Cao, G. Hu, L. Huo, X. Zhu, T. Li, J. Powell, Y. Ito, **(2008)**. Stationary Phase Retention and Preliminary Application of a Spiral Disk Assembly Designed for High-speed Counter-current Chromatography, *J. Chromatogr. A.,* **1188:** 164.

[74] V. Berejnov, N. Djilali, D. Sinton, **(2008)**. Lab-on-chip methodologies for the study of transport in porous media: energy applications, *Lab Chip,* **8(5):** 689.

[75] J. Ducrée, S. Haeberle, T. Brenner, T. Glatzel, R. Zengerle, **(2006)**. Patterning of flow and mixing in rotating radial microchannels, *Microfluid Nanofluid,* **2(2):** 97.

[76] A. Braithwaite, F. J. Smith, **(1996)**. High Performance Liquid Chromatography. In: Chromatographic Methods, fifth edition, pp: 263-290. Chapman & Hall, London, UK.

[77] T. Taniguchi, S. Ito, **(2003)**. Molecular Dynamics Simulation of the Structure of Soda-lime-silica Glass. *Reports Res. Lab. Asahi Glass Co., Ltd.,* **53:**1.

[78] D. Clicq, R. W. Tjerkstra, J. G. E. Gardeniers, A. Van den Berg, G. V. Baron, G. Desmet, **(2004)**. Porous Silicon as a Stationary Phase for Shear-driven Chromatography. *J. Chromatogr. A.,* **1032:** 185.

[79] D. Cabooter, J. Billen, H. Terryn, F. Lynen, P. Sandra, G. Desmet, **(2008)**. Detailed Characterisation of the Flow Resistance of Commercial sub-2 μm Reversed-phase Columns, *J. Chromatogr. A.,* **1178:** 108.

[80] P. Enzel, N. Adelman, K. J. Beckman, D. J. Campbell, A. B. Ellis, G. C. Lisensky, (1999). Preparation of an Aqueous-Based Ferrofluid, J. Chem. Educ., **76:** 943.

[81] F. Gritti, G. Guiochon, **(2008)**. Complete Temperature Profiles in Ultra-High-Pressure Liquid Chromatography Columns. *Anal. Chem.,* **80(13):** 5009.

[82] L. W. Bezuidenhout, M. J. Brett, **(2008)**. Ultrathin Layer Chromatography on Nanostructured Thin Films. *J. Chromatogr. A.,* **1183:** 179.

[83] J. R. Lakowicz, **(2006)**. Energy Transfer. In: Principles of Fluorescence Spectroscopy third edition, pp. 443-475. Springer Science+Business Media, LLC.

[84] T. Förster , **(1948)**. Intermolecular energy migration and fluorescence (Transl RS Knox). *Ann. Phys. (Leipzig),* **2:**55.

[85] JJ.Van Deemter, FJ. Zuiderweg, A. Klinkenberg, **(1956)**. Longitudinal diffusion and resistance to mass transfer as causes of non ideality in chromatography. *Chem. Eng. Sc.* **5:** 271.

[86] J. Standard, **(2006)**. Diffusion. In: Applications of Programming in Chemistry Lecture Notes, pp. 84-90. Department of Chemistry, Illinois State University.

[87] G. Gerhardt, R. N. Adams, **(1982)**. Determination of Diffusion Coefficients by Flow Injection Analysis. *Anal. Chem.*, **54(16):** 2618.

[88] C. T. Culbertson, S. C. Jacobson, J. M. Ramsey, **(2002)**. Diffusion Coefficient Measurements in Microfluidic Device. *Talanta,* **56:** 365.

[89] K. Pappaert, J. Biesemans, D. Clicq, S. Vankrunkelsven, G. Desmet, **(2005)**. Measurements of Diffusion Coefficients in 1-D Micro- and Nanochannels using Shear-driven Flows. *Lab Chip.,* **5 (10):** 1104.

[90] Y. Cai, D. Janasek, J. West, J. Franzke, and A. Manz, **(2008)**. Channel-free Shear Driven Circular Liquid Chromatography. *Lab Chip*., **8 (11):** 1784.

[91] B**.** H. Weigl**,** P. Yager, **(1999)**. MICROFLUIDICS: Microfluidic Diffusion-Based Separation and Detection. *Science,* **283 (5400):** 346.

[92] V. Okhonin, E. Wong, S. N. Krylov, **(2008)**. Mathematical Model for Mixing Reactants in a Capillary Microreactor by Transverse Diffusion of Laminar Flow Profiles. *Anal. Chem.,* **80 (19):** 7482.

[93] N. A. Polson, M. A. Hayes, **(2001)**. Microfluidics: controlling fluids in small places. *Anal.Chem.,* **73(11):** 312 A.

[94] C. T. Culbertson, S. C. Jacobson, J. M. Ramsey, **(1998)**. Dispersion Sources for Compact Geometries on Microchips, *Anal. Chem.,* **70 (18):** 3781.

[95] L. M. Fu, R. J. Yang, G. B. Lee, Y. J. Pan, **(2003)**. Multiple injection techniques for microfluidic sample handling, *Electrophoresis,* **24 (17):** 3026.

[96] C. D. Thomas, S. C. Jacobson, J. M. Ramsey, **(2004)**. Strategy for Repetitive Pinched Injections on a Microfluidic Device, *Anal. Chem.,* **76 (20):** 6053.

[97] A. M. Leach, A. R. Wheeler, R. N. Zare, **(2003)**. Flow Injection Analysis in a Microfluidic Format, *Anal. Chem.,* **75 (4):** 967.

[98] X. Bai, H. J. Lee, J. S. Rossier, F. Reymond, H. Schafer, M. Wossner, H. H. Girault, **(2002)**. Pressure pinched injection of nanolitre volumes in planar micro-analytical devices, *Lab Chip,* **2 (1):** 45.

[99] L. Zhang, X. F. Yin, Z. L.Fang, **(2006)**. Negative pressure pinched sample injection for microchip-based electrophoresis, *Lab Chip,* **6 (2):** 258.

[100] C. X Zhang, A. Manz, **(2001).** Narrow Sample Channel Injectors for Capillary Electrophoresis on Microchips, *Anal. Chem.,* **73 (11):** 2656.

[101] Q. Fang, T. Zhang, J. Fu, **(2008)**. Microfluidic Spontaneous Sample Injection in the Picoliter Range for High-Speed Capillary Electrophoresis, Oral presentation in MicroScale Bioseparations and Methods for System Biology Conference (MSB) 2008, Berlin, Germany.

[102] H. Xu, T. P. Roddy, J. A. Lapos, A. G. Ewing, **(2002)**. Parallel Analysis with Optically Gated Sample Introduction on a Multichannel Microchip, *Anal. Chem.,* **74 (21):** 5517.

[103] Y. Z. Huang, W. B. Du, J. Z. Pan, Q. Fang, **(2008).** Microfluidic chip-based valveless flow injection analysis system with gravity-driven flows, *Analyst*, **133:** 1237.

[104] X. Noblin, L. Mahadevan, I. A. Coomaraswamy, D. A. Weitz, N. M. Holbrook, M. A. Zwieniecki, **(2008)**. Optimal vein density in artificial and real leaves, *Proc. Natl. Acad. Sci. U. S. A.*, **105 (27):** 9140.

[105] W. D. Malsche, D. Clicq, H. Eghbali, V. Fekete, H. Gardeniers, G. Desmet, **(2006)**. An automated injection system for sub-micron sized channels used in shear-driven-chromatography, *Lab Chip,* **6 (10):** 1322.

[106] H. Schmidt-Traub, **(2005)**. Fundamentals and General Terminology. In: Preparative Chromatography, pp. 32-36. WILEY-VCH Verlag GmbH&Co.

[107] J. West, A. Michels, S. Kittel, P. Jacob, J. Franzke, **(2007)**. Microplasma writing for surface-directed millifluidics, *Lab Chip,* **7 (8):** 981.

[108] B. Zhao, J. S. Moore, D. J. Beebe, **(2001)**. Surface-Directed Liquid Flow Inside Microchannels, *Science,* **291 (5506):** 1023.

YING CAI

Dessauerstrasse 28 Zi.10, 44263, Dortmund
Mobil: +49 (0)176 236 465 16
E-mail: yingcai@gmx.de
Nationalität: chinesisch
Geburtstag: 16.05.1982

◆ Ausbildung

- ✦ Seit 11.2005 **ISAS — Institute for Analytical Sciences (Technische Universität Dortmund),** Dortmund, Deutschland

  Doktorarbeit an der Fakultät Bio- und Chemieingenieurwesen "Microfluidic Separation: Validation of Shear Driven Circular Liquid Chromatography"
- ✦ 09.2003 — 10.2005 **Universität Siegen,** Siegen, Deutschland

  Master of Science in analytischer Chemie. "Characterization of Self-assembled Monolayers (SAMs) of Alkanethiols on Au (111) for Lab on Chip Capillary Coating"
- ✦ 09.1999 — 07.2003 **Shanghai Jiao Tong University,** Shanghai, China

  Bachelor of Engineering in Polymerchemie. "Polymerization and Characterization of Polymers based on Dibenzothiophene Dioxide"

◆ Auszeichnungen

- ✦ Seit 06.2008 Associate Member of the Royal Society of Chemistry (AMRSC), UK
- ✦ 2003-2005 Dekan Stipendium der Siegen Universität (2 Stipendiaten der Fakultät Chemie)
- ✦ 2001-2002 Klasse B- Stipendium der Shanghai Jiao Tong University (top 5%)
- ✦ 2000-2001 Klasse B- Stipendium der Shanghai Jiao Tong University (top 5%)
  Kwang-Hua Stipendium der Kwang-Hua Education Foundation, China
- ✦ 1999-2000 Klasse B- Stipendium der Shanghai Jiao Tong University (top 5%)
  Stipendium der Datang Telecom Technology & Industry Group, China
  Ausgezeichnete Studentin der Shanghai Jiao Tong University (3 aus 160)

◆ Publikationen

Papers

- ✦ **Y. Cai**, D. Janasek, J. West, J. Franzke, and A. Manz. Channel-free Shear Driven Circular Liquid Chromatography. *Lab on a Chip*, (2008), **8**: 1784-1786.
- ✦ **Y. Cai**, D. Janasek, J. Franzke, and A. Manz. A Channel-free Separation System Based on Circular Shear Driven Flow. *Proceedings of MicroTAS 2008, 12th International Conference on Miniaturized Systems for Chemistry and Life Sciences*, (2008), 1444-1446.

Konferenz

- ✦ 7.GDCh — Gesellschaft Deutscher Chemiker e.V, Berlin, Germany, 2005. " Characterization of Self-assembled Monolayers for Lab-on-Chip capillary coating".
- ✦ 12th International Conference on Miniaturized Systems for Chemistry and Life Sciences, San Diego, USA, 2008. "A Channel-free Separation System based on Circular Shear Driven Flow".

◆ Sprachkenntnisse

- ✦ Chinesisch: Muttersprache
- ✦ Englisch: fließend
- ✦ Deutsch: sehr gute Kenntnisse

◆ EDV-Kenntnisse

Microsoft office, Origin, Adobe Illustrator, MATLAB, AutoCAD, ChemOffice

◆ Fachliche Tätigkeiten

HPLC, CE, IR-Spektrometrie, UV-vis Spektrometrie, AFM und andere analytische Instrumente

◆ Referenzen

- ✦ Prof. Dr. Andreas Manz, ehemalige Institutsleitung des ISAS — Institute for Analytical Sciences, *Email*: a.manz@isas.de
- ✦ Prof. Dr. Andreas Schmid, TU Dortmund, Fakultät Bio- und Chemieingenieurwesen, *E-mail:* andreas.schmid@bci.uni-dortmund.de
- ✦ Prof. Dr. Bernd Wenclawiak, Siegen Universität, *Email*: wenclawiak@chemie.uni-siegen.de
- ✦ Prof. Jie Yin, vice president, Shanghai Jiao Tong University, *Email*: jyin@sjtu.edu.cn